MINISTERE DE L'ENSEIGNEMENT SUPERIEUR ET DE LA RECHERCHE
SCIENTIFIQUE

UNIVERSITE MOHAMED KHIDER BISKRA

FACULTE DES SCIENCES EXACTES
ET
DES SCIENCES DE LA NATURE ET DE LA VIE

Département des Sciences de la matière

THESE
Présentée par

Djani Faiçal

En vue de l'obtention du diplôme de :
DOCTORAT EN SCIENCES

Option :
Chimie des matériaux

Intitulée :

Etude physicochimique du système LaMM'O$_3$ à base de métaux divalents et trivalents.

Soutenue le : 30/10/2016

Devant la commission d'Examen

Barkat	Djamel	Prof.	Univ. Biskra	Président
Omari	Mahmoud	Prof.	Univ. Biskra	Directeur de thèse
Martinez-Arias	Arturo	Prof.	Univ. Madrid	Co-directeur de thèse
Lanez	Touhami	Prof.	Univ. El-Oued	Examinateur
Ouahrani	Mohamed Rida	Prof.	Univ. El-Oued	Examinateur
Meghezzi	Ahmed	Prof.	Univ. Biskra	Examinateur

Acknowledgment

Dedication

To my Parents

To my Brothers and Sisters

To my Wife and Daughters

To all my Friends anywhere

Faiçal

Contents

Chapter II

Chapter III

Chapter IV

Abstract

Abbreviations

VOCs	Volatile Organic Compounds
XRD	X-Ray Diffraction
XPS	X-Ray Photoelectron Spectroscopy
BET	Brunnauer-Emmett-Teller
PSD	Particle Size Distribusion
TGA	Thermogravimetric Analysis
DTA	Differential Thermal Analysis
FTIR	Fourier Transform Infra-Red
SEM	Scanning Electronic Microscopy
MO	Methyl Orange
DSSC	Dye-Sensitized Solar Cell
ITO	Indium Tin Oxide
PEDOT	Poly(3,4-EthyleneDioxyThiophene)
PSS	Poly (Styrène sulfonate) de Sodium
PTAA	Poly(triaryl amine), Poly[bis(4-phenyl)(2,4,6-trimethylphenyl)amine]
PCBM	Phenyl-C_{61}-Butyric acid Methyl ester
EDTA	EthylenDiamineTetraacetic Acid
DSC	Differential Scanning Calorimetry
TEM	Transmission Electron Microscopy
ESCA	Electron Spectroscopy for Chemical Analysis
JCPDS	Joint Committee on Powder Diffraction Standards

List of Tables

Chapter I

Chapter III

Chapter IV

Figures List

Chapter I

Chapter II

Chapter III

Chapter IV

General introduction

General introduction

Perovskite mixed oxides with the general formula ABO_3 containing rare earth elements (in A position) and 3d transition metals (in B position) are considered as strategic materials due to their interesting electrical, magnetic, optical and catalytic properties [1,2,3,4]. Among them, lanthanum nickel oxide $LaNiO_3$ with perovskite structure is considered of great interest because of its electronic and catalytic properties which make it a promising base material for its use as electrode material for storage and conversion of energy [5, 6], as well as a catalyst for the methane reforming reaction [7, 8, 9, 10, 11], for redox reactions involving NO, CO or soot [12, 13, 14] or for VOC's combustion reactions [15, 16].

Furthermore, VOC's combustion activity has been shown to be enhanced upon partial nickel substitution by iron in the perovskite structure as well as by the presence of nickel oxide as in the form of nanocomposites with a segregate phase interacting with the partially substituted perovskite [15]. Within this context, a sol-gel method (Pechini approach) , sol gel combustion using citric acid, ascorbic acid, sucrose, as chelating agents and methanol, ethanol, water as solvents, has been used to prepare different $La(Ni,Fe)O_x$ catalysts. In addition to the $LaNiO_3$ perovskite prepared by the same method and used as a reference sample, different formulations in which nominal amounts of Ni + Fe employed are in excess with respect to that of La have been prepared with the aim of achieving nickel substitution in the perovskite simultaneous to segregated NiO. The latter hypothesis is based on the fact that the thermodynamic stability $LaFeO_3$ is higher than that of $LaNiO_3$ [17].

Therefore, it could be expected that the substitution of Ni by Fe in the perovskite can be favoured and could induce the segregation of excess Ni in the form of NiO. The samples have been characterized by X-ray diffraction (XRD), X-ray photoelectron spectroscopy (XPS), Brunauer-Emmett-Teller specific surface area (S_{BET}) analysis, infrared spectroscopy (IR), thermal analysis (TGA-DTA) and powder size distribution (PSD) as a basis to explain their catalytic behavior for CO oxidation.

Our work is divided into four chapters:

 ➢ The first chapter is devoted to a literature review covering the one hand knowledge on mixed oxides of perovskites, and also their applications catalytic properties

 ➢ The second chapter is the subject of experimental techniques: preparation methods, physicochemical characterization techniques and the description of the catalytic tests installation.

 ➢ The third chapter is devoted to the effect of the synthesis method, the complexing agent, the solvent on the physicochemical properties of perovskite $LaNiO_3$.

 ➢ The fourth chapter presents the Synthesis, characterization and catalytic properties of La $(Ni.Fe)O_3$-NiO nanocomposites.

This work ends with general conclusion.

References

[1] Lacorre P, Torrance JB, Pannetier J, Nazzal AI, Wang PW, Huang TC (1991) Synthesis, crystal structure, and properties of metallic $PrNiO_3$: Comparison with metallic $NdNiO_3$ and semiconducting $SmNiO_3$. Solid State Chem 91(2):225-237.

[2] Chen MS, Wu TB, Wu JM (1996) Effect of textured $LaNiO_3$ electrode on the fatigue improvement of $Pb(Zr_{0.53}Ti_{0.47})O_3$ thin films. Appl Phys Lett 68(10):1430-1432.

[3] Singh RN, Tiwari SK, Singh SP, Jain AN, Singh NK (1997) Electrocatalytic activity of high specific surface area perovskite-type $LaNiO_3$ via sol-gel route for electrolytic oxygen evolution in alkaline solution. Int J of Hydr Ener
22(6):557-562.

[4] Peña MA, Fierro JLG (2001) Chemical Structures and Performance of Perovskite Oxides. Chem Rev 101(7):1981-2018.

[5] Ling TR, Chen ZB, Lee MD (1996) Catalytic behavior and electrical conductivity of LaNiO3 in ethanol oxidation. Appl Catal A 136(2):191-203.

[6] Burselle M, Pirjamali M, Kiros Y (2002) $La_{0.6}Ca_{0.4}CoO_3$, $La_{0.1}Ca_{0.9}MnO_3$ and LaNiO3 as bifunctional oxygen electrodes. Electr Acta 47(10):1651-1660.

[7] Lima SM, Assaf JM, Peña MA, Fierro JLG (2006) Structural features of $La_{1−x}Ce_xNiO_3$ mixed oxides and performance for the dry reforming of methane. Appl Catal A 311:94-104.

[8] Valderrama G, Kiennemann A, Goldwasser MR (2008) Dry reforming of CH_4 over solid solutions of $LaNi_{1−x}Co_xO_3$. Catal Today 133:142-148.

[9] Valderrama G, Goldwasser MR, De Navarro CU, Tatibouët JM, Barrault J, BatiotDupeyrat C, Martínez F (2005) Dry reforming of methane over Ni perovskite type oxides. Catal Today107:785-791.

[10] De Lima SM, Da Silva AM, Da Costa LOO, Assaf JM, Jacobs G, Davis BH, Mattos LV, Noronha FB (2010) Evaluation of the performance of Ni/La_2O_3 catalyst prepared from $LaNiO_3$ perovskite-type oxides for the production of hydrogen through steam reforming and oxidative steam reforming of ethanol. Appl Catal A 377(1-2):181-190.

[11] Pereñiguez R, Gonzalez-delaCruz VM, Caballero A, Holgado JP (2012) $LaNiO_3$ as a precursor of Ni/La_2O_3 for CO_2 reforming of CH_4: Effect of the presence of an amorphous NiO phase . Appl Catal B 123:324-332.

[12] Norman AK, Morris MA (1999) The preparation of the single-phase perovskite $LaNiO_3$. Mater Proc Technol 92:91-96.

[13] Russo N, Fino D, Saracco G, Specchia V (2008) Promotion effect of Au on perovskite catalysts for the regeneration of diesel particulate filters. Catal Today 137(2):306-311.

[14] Rida K, Pena MA, Sastre E, and Martinez-Arias A (2012) Effect of calcination temperature on structural properties and catalytic activity in oxidation reactions of $LaNiO_3$ perovskite prepared by Pechini method. J of Rare Earths 30(3):210-216.

[15] Pecchi G, Reyes P, Zamora R, Cadús LE, Fierro JLG (2008) Surface properties and performance for VOCs combustion of $LaFe_{1-y}Ni_yO_3$ perovskite oxides. Solid State Chem 181(4):905-912.

[16] De la Cruz RG, Falcón H, Peña MA, Fierro JLG (2001) Role of bulk and surface structures of $La_{1-x}Sr_xNiO_3$ perovskite-type oxides in methane combustion. Appl Catal B 33(1):45-55.

[17] Cheng J, Navrotsky A, Zhou XD, Anderson HU (2005) Enthalpies of formation of $LaMO_3$ perovskites (M = Cr, Fe, Co, and Ni). Mater Res 20(1):191–200.

First Chapter

Bibliographical study

A- Chemistry and Crystallography of Perovskites.

I.1 Introduction

The structural family of perovskites is a large family of compounds having crystal structures related to the mineral perovskite $CaTiO_3$. In the ideal form the crystal structure of cubic ABX_3 perovskite can be described as consisting of corner sharing $[BX_6]$ octahedra with the A cation occupying the 12-fold coordination site formed in the middle of the cube of eight such octahedra. The ideal cubic perovskite structure is not very common and also the mineral perovskite itself is slightly distorted. The perovskite family of oxides is probably the best studied family of oxides. The interest in compounds belonging to this family of crystal structures arise in the large and ever surprising variety of properties exhibited and the flexibility to accommodate almost all of the elements in the periodic system. Pioneering structural work on perovskites was conducted by Goldschmidt et al in the 1920: s that formed the basis for further exploration of the perovskite family of compounds. Distorted perovskites have reduced symmetry, which is important for their magnetic and electric properties. Due to these properties, perovskites have great industrial importance, especially the ferroelectric tetragonal form of $BaTiO_3$ [1].

I.2 The crystal structure of perovskite

Perovskite titanate is natural calcium $BaTiO_3$, and a very large number of compounds of formula ABO_3 present this structure (not to be confused with $MM'O_3$ type structures or cations M and M' have similar ionic radii). The perovskite structure is characterized by the association of large cations A, of radius r_A (alkali, alkaline earth or rare earths) and smaller radii r_B transition metal cations. B cations occupy the corners of a cube, while the A cations occupy the center of the cube. The atony of oxygen is placed in the middle of the edges of the cube. This structure, characterized by $Z = 1$. The ABO_3 unit cell is shown in Figure I.1 [2].
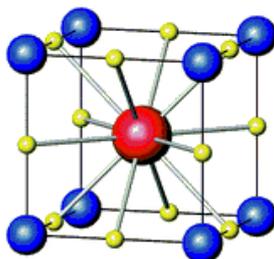
Figure I.1 *Arrangement of atoms in perovskite structure* ABO_3

The coordination numbers for each of the cations compared by oxygen are:

- Cation A, situated in the center of the unit cell, that are equidistant from the edges environments A/O = 12.
- For cations B, located at the corners of the unit cell, occupying octahedral sites: B/O = 6.

The following table shows the Typical perovskite compounds:

Table I.1 *Typical perovskite compounds* [3].

Compound	Lattice parameter/x 10 nm		
	a	b	c
Cubic structure			
$KTaO_3$	3.989		
$NaTaO_3$	3.929		
$NaNbO_3$	3.949		
$BaMnO_3$	4.040		
$BaZrO_3$	4.193		
$SrTiO_3$	3.904		
$KMnF_3$	4.189		
$KFeF_3$	4.121		
Tetragonal structure			
$BiAlO_3$	7.61		7.94
$PbSnO_3$	7.86		8.13
$BaTiO_3$	3.994		4.038
$PdTiO_3$	3.899		4.153
$TlMnCl_3$	5.02		5.04
LaAlO3 type			
$LaAlO_3$	5.357	$\alpha = 60° 06'$	
$LaNiO_3$	5.461	$\alpha = 60° 05'$	
$BiFeO_3$	5.632	$\alpha = 60° 06'$	
$KNbO_3$	4.016	$\alpha = 60° 06'$	
$GdFeO_3$ type			
$GdFeO_3$	5.346	5.616	7.668
$YFeO_3$	5.283	5.592	7.603
$NdGaO_3$	5.426	5.502	7.706
$CaTiO_3$	5.381	5.443	7.645
$NaMgF_3$	5.363	5.503	7.676

The simple examination of the elementary cell, which has only motive, allows to define the geometric conditions for this structure is observed:

$$(r_A + r_O) = \sqrt{2} \, (r_B + r_O)$$

It's actually a very strict condition and Goldschmidt introduced a tolerance factor t to explain the existence of such a structure for a wide range of ionic radii:

$$(r_A + r_O) = t\sqrt{2} \, (r_B + r_O)$$

According to the values of t, it is observed, cubic structures more or less distorted:

$t > 1$: hexagonal distortion (ex: $BaTiO_3$, $NaNbO_3$).

$1 < t < 0.95$: cubic structure (ex: $BaZrO_3$, $LaMnO_3$).

$0.95 < t < 0.9$: quadratic distortion (ex: $RbTaO_3$, $KNbO_3$).

$0.9 < t < 0.8$: orthorhombic distortion (ex: $PbTiO_3$, $GdFeO_3$).

The limits of the tolerance factor will vary with the charge of the cations A and B.
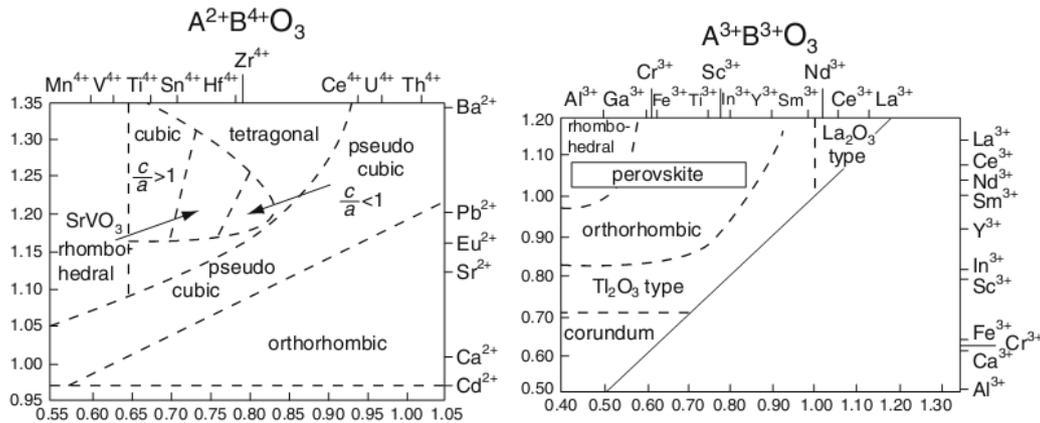
Figure I.2 *The effect of ionic size of A- and B-site cations on the observe distortions of the perovskite structure* [3].

It is evident that almost all elements except for noble gases can occupy either A or B lattice positions in the perovskite lattice, including dopants. The stability and the crystal group are mainly determined by the ratio of the ionic radii of the A and B cations. Indeed, the structure is dependent not only on the size but also on the nature of the A and B atoms. For example, $AMnO_3$ compounds crystallize in the perovskite structure when the A cation is La or Ce-Dy, whereas a new

hexagonal structure with 5- and 7-coordination of Mn and A, respectively, is formed when A = Ho-Lu or Y if A = La or Ce-Dy [3, 4].

Figure I.3 Chemical elements that can occupy sites in the perovskite structure.

I.3 Types of crystal perovskites ABO₃ structure

I.3.1 Orthorhombic perovskite

The $GdFeO_3$ structure is probably the most illustrative of all the orthorhombic perovskites distorted. Its space group is Pnma and lattice parameters are: $a = 5.346$, $b = 5.616$, $c = 7.668$, all ±0.004 Å. The $GdFeO_3$ structure is a distorted form of perovskite. The distortion mechanism is a tilting of essentially rigid MX_6 octahedra. It occurs when the A-site cation is too small for its 12 coordinate cavity in the cubic perovskite structure. This distortion of the perovskite structure is the predominant for perovskites with tolerance factors smaller than ~0.98. The distortion has several consequences [5]. Other materials adopting this orthorhombic-structure distorted are: $NaUO_3$, $LaYbO_3$ [6].

I.3.2 Rhombohedral perovskite

In several materials, the cubic cell may have a small deformation in the rhombohedral symmetry. If the distortion is not expand the unit cell, it is possible to index the unit cell containing one or two formulas respectively unitary with the

rhombohedral angles α ~ 90° or α ~ 60°. However, anions are generally placed as required larger cell unit with α ~ 60 °. As examples of rhombohedral perovskites: $LaNiO_3$ and $LaCoO_3$.
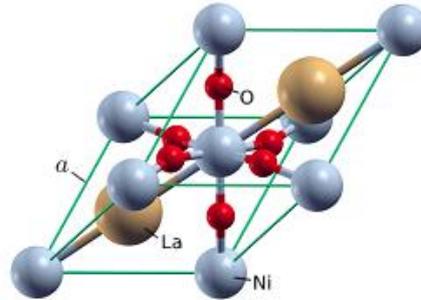
Figure I.4 *Primitive cell of LaNiO₃* [7].

I.3.3 Tetragonal perovskite

The crystal structure of $PbTiO_3$ is another derivative of the perovskite structure: It has space group P4mm, with a=3.902˚A, c=4.156˚A, Z=1. Compared with cubic $SrTiO_3$, $PbTiO_3$ is characterized by an elongation of the unit cell. The TiO_6 octahedron in the unit cell is more or less undeformed (strictly speaking it is the combination of two tetragonal pyramids of slightly different heights) but shifted along the c-axis. However, the displacement of the O^{2-} ions is bigger than the displacement of the Ti^{4+} ion, leading alltogether to a separation of the two centers of the positive and negative charges within the unit cell. This results in a permanent dipole of each unit cell. Figure I.5 (a) shows a single unit cell and the O^{2-} ion of the next cell above it, in order to depict a complete TiO_6 octahedron. Figure I.5 (b) shows the same arrangement as Figure I.5 (a), but more from the front so that the different displacements of the ions along the c-axis become better visible [8, 9].
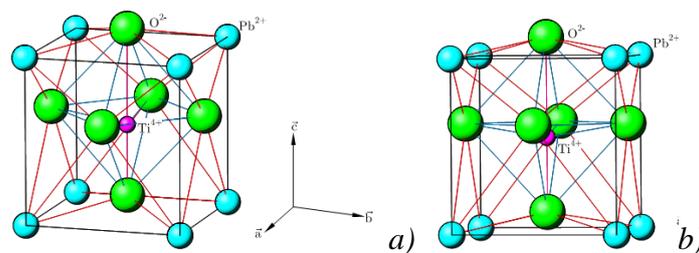
Figure I.5 *two views of the unit cell of PbTiO₃.*

I.3.4 Monoclinic and triclinic Perovskite

The structure of $CaRhO_3$, is monoclinic with lattice parameters of a = 12.5114 Å, 3.1241 Å, c = 8.8579(1) Å, β = 103.951(1), V = 336.01(1) $Å^3$ with space group $P2_1/m$. The structure contains edge-sharing RhO_6 octahedral chains along the b-axis. The six RhO_6 octahedral chains make a unit, which stacks up alternatively with the CaO_8 polyhedral layer along the [101] direction to form the structure of $CaRhO_3$ intermediate phase [10]. Also $BiMnO_3$ and $BiScO_3$ have a monoclinic perovskite crystal structure. $AgCuF_3$, $CsPbI_3$, $PbSnO_3$ have a triclinic perovskite structure.
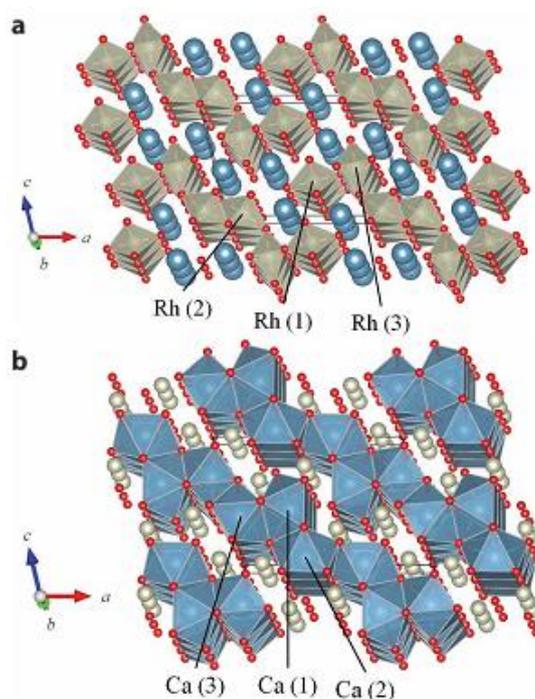
Figure I.6 *Crystal structure of CaRhO₃ intermediate phase with (a) RhO₆ octahedra, and with (b) CaO₈ polyhedra* [10].

$SrLaCuNbO_6$ and $SrLaCuTaO_6$ are Jahn–Teller distorted double perovskites with complete B –site ordering. The crystal structure of $SrLaCuTaO_6$ has been solved by refinement of neutron powder diffraction data at 323 (triclinic), 573(monoclinic) and 923 K (body-centered monoclinic) [11, 12].
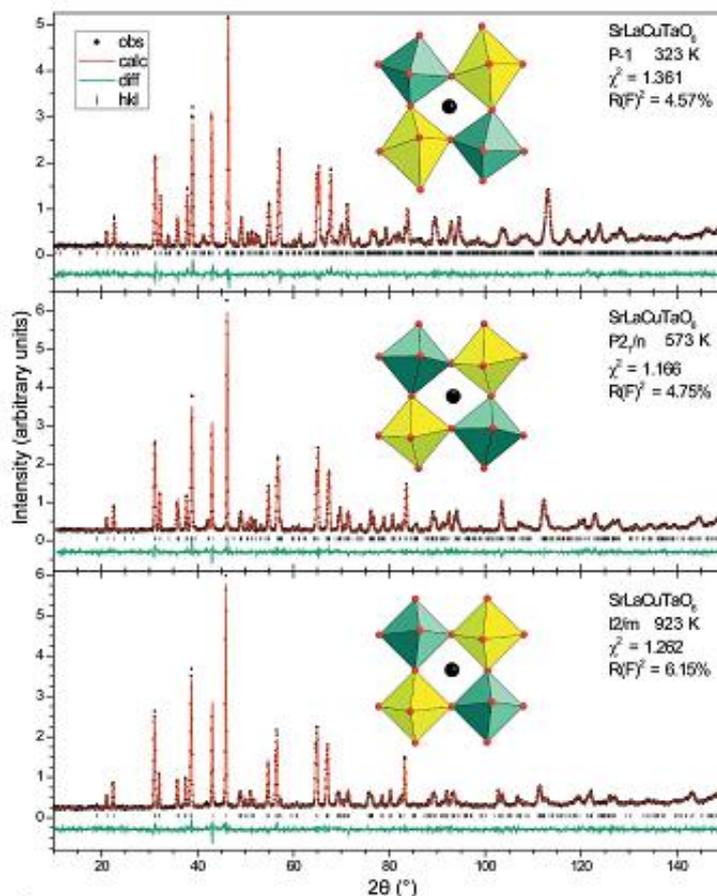
Figure I.7 *Refinements for SrLaCuTaO₆ at 323 (top), 573 (middle)*

and 923 K (bottom). [11]

I.3.5 Polymorphism

The distortion of the [BO₆] octahedra due to temperature changes or stress effects may cause the transition from cubic structure to tetragonal, rhombohedral or orthorhombic structures. Distorted perovskites have reduced symmetry, which is important for their magnetic and electric properties. Due to these properties, perovskites have great industrial importance and huge potential for cutting edge technology, especially the ferroelectric pseudo-cubic barium titanate, $BaTiO_3$. In most cases several factors act on the structure. As an example of the complexity $BaTiO_3$ has four phase transitions on heating: rhombohedral (R3m) — – 90 °C → orthorhombic (Amm2) — 5 °C → tetragonal (P4mm) — 120 °C → cubic (Pm $\bar{3}$m) [13].
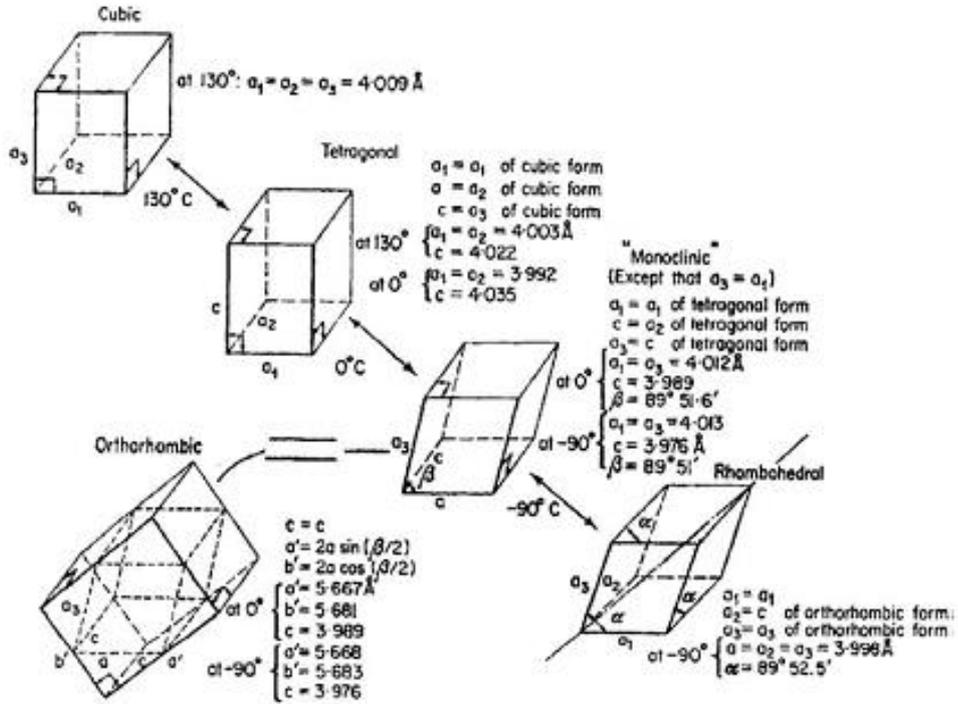
Figure I.8 Distortion of BaTiO₃ unit cell showing temperature dependence. [13]
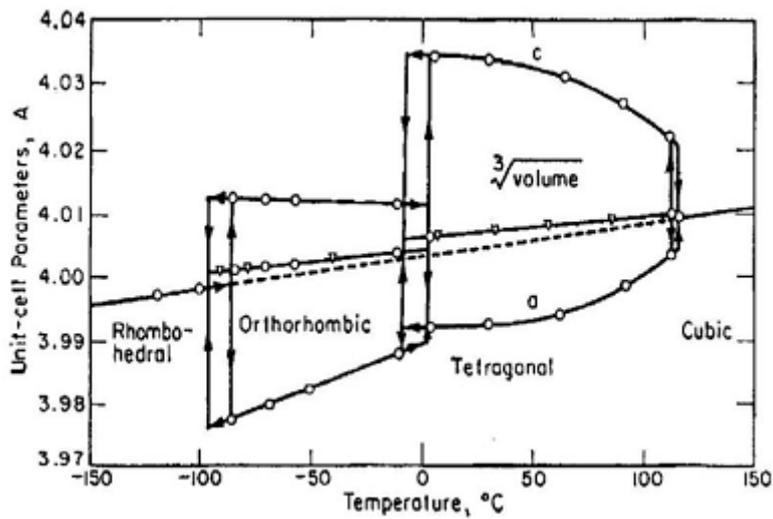
Figure I.9 Lattice constants of BaTiO3 as a function of temperature. [13]

I.4 Defects in the Crystalline Structure

Real crystals having different types of defects that represent an internal surplus energy of the crystal relative to a perfect crystal, and therefore a deviation from the maximum stability.

I.4.1 point defects: Vacancies, Interstitial, and Substitutional

I.4.1.1 Vacancies defects

A vacancy defect is formed when an atom is missing from a normal atomic site in a crystalline structure.
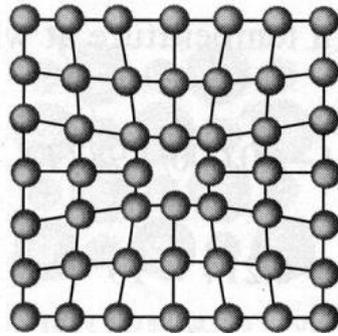
Figure I.10 vacancy defect in a crystalline structure.

The number of vacancies present in a material increases exponentially as the temperature increases. If n is the number of defects and N the total number of crystal sites: $n / N = A \exp (-Q / RT)$

With A dimensionless constant, Q energy of formation of point defect (J / mol), R ideal gas constant = 8.32 J / K, T the absolute temperature of the crystal (K).

The following figure shows the vacancy defect in the crystal structure of $LaNiO_3$
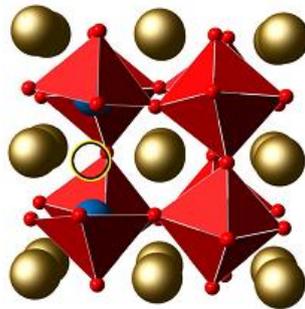
Figure I.11 Cell of $LaNiO_3$ with a single oxygen vacancy showing NiO_6 octahedra. The position of the vacancy is indicated by the open black circle. [7]

I.4.1.2 Interstitial Defects

An Interstitial defect is formed when an extra atom occupies a normally unoccupied site (interstitial site), since the interstitial atoms are larger than the interstitial sites the surrounding lattice is in compression.
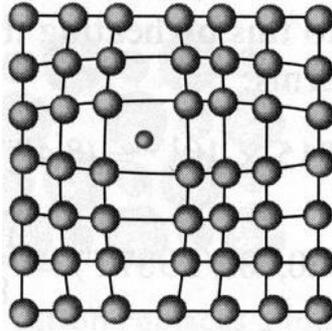
Figure I.12 Interstitial defect in a crystalline structure.

I.4.1.3 Substitutional Defects

Substitutional defects are produced when one atom is replaced by a different type of atom, if the substitutional atom is smaller than the original atom then the lattice is in tension. If the substitutional atom is larger than the original atom then the lattice is in compression.

a)   b)
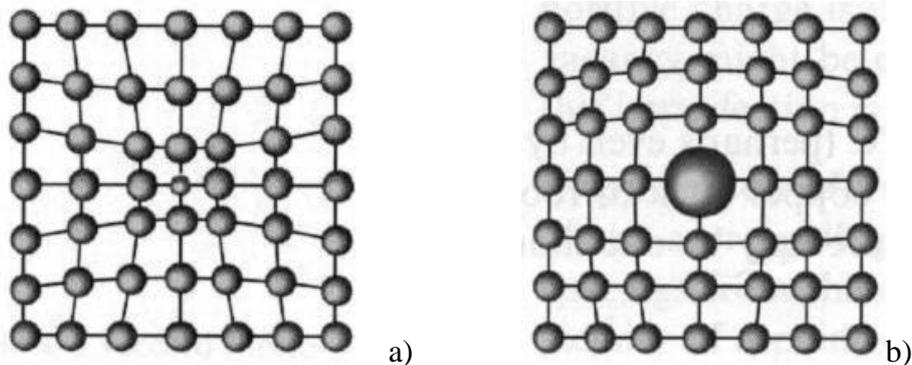
Figure I.13 Substitutional defect in a crystalline structure. (a) the substitutional atom is smaller then the original atom,(b) the substitutional atom is larger then the original atom.

I.4.2 linear defects

In linear defects groups of atoms are in irregular positions. Linear defects are commonly called dislocations. Any deviation from perfectly periodic arrangement of atoms along a line is called the line imperfection. In this case, the distortion is centered only along a line and therefore the imperfection can be considered as the boundary between two regions of a surface which are perfect themselves but are out of register with each other. The line imperfection acting as boundary between the slipped and un-slipped region, lies in the slip plane and is called a dislocation. Dislocations are generated and move when a stress is applied. The strength and ductility of metals are controlled by dislocations [14].

I.4.2.1 Edge Dislocations

The inter-atomic bonds are significantly distorted only in the immediate vicinity of the dislocation line. As shown in the set of images above, the dislocation moves similarly moves a small amount at a time. The dislocation in the top half of the crystal is slipping one plane at a time as it moves to the right from its position in image (a) to its position in image (b) and finally image (c). In the process of slipping one plane at a time the dislocation propagates across the crystal. The movement of the dislocation across the plane eventually causes the top half of the crystal to move with respect to the bottom half. However, only a small fraction of the bonds are broken at any given time. Movement in this manner requires a much smaller force than breaking all the bonds across the middle plane simultaneously [15].
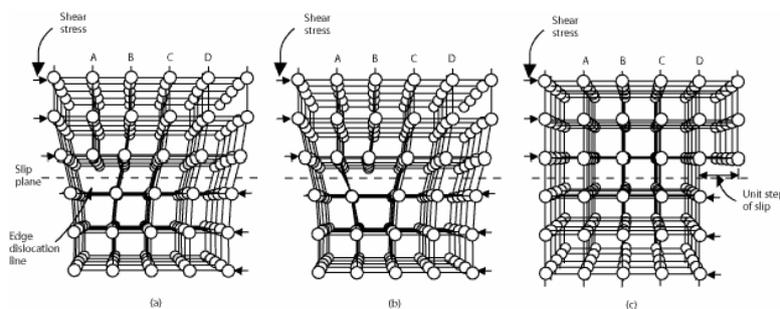
Figure I.14 *Edge Dislocations (linear defect)*

I.4.2.2 Screw Dislocations

The screw dislocation is slightly more difficult to visualize. The motion of a screw dislocation is also a result of shear stress, but the defect line movement is perpendicular to direction of the stress and the atom displacement, rather than parallel. To visualize a screw dislocation, imagine a block of metal with a shear stress applied across one end so that the metal begins to rip. This is shown in the upper right image. The lower right image shows the plane of atoms just above the rip. The atoms represented by the blue circles have not yet moved from their original position. The atoms represented by the red circles have moved to their new position in the lattice and have reestablished metallic bonds. The atoms represented by the green circles are in the process of moving. It can be seen that only a portion of the bonds are broke at any given time. As was the case with the edge dislocation, movement in this manner requires a much smaller force than breaking all the bonds across the middle plane simultaneously[16].
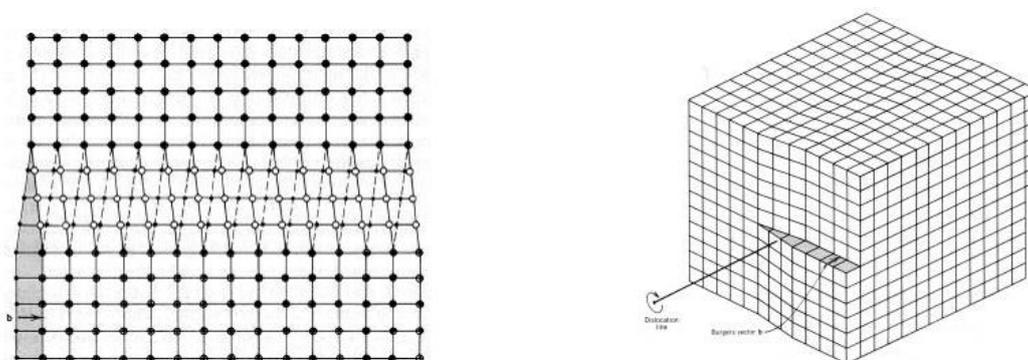
Figure I.15 Screw Dislocations (linear defect)

I.4.3 Planar defects

Planar defects, which are interfaces between homogeneous regions of the material. Planar defects include grain boundaries, stacking faults and external surfaces. The crystalline structure of each grain is identical but there orientations are not. The grain boundaries is a narrow zone where the atoms are not properly spaced.
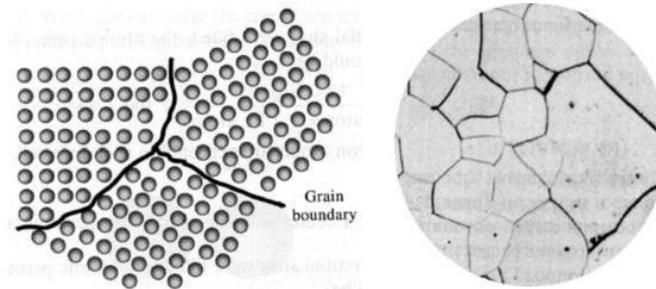
Figure I.16 grain boundaries defects (Planar defects).

I.4.4 Volume or Bulk Defects

Bulk defects occur on a much bigger scale than the rest of the crystal defects discussed in this section. However, for the sake of completeness and since they do affect the movement of dislocations, a few of the more common bulk defects will be mentioned. Voids are regions where there are a large number of atoms missing from the lattice. The image to the right is a void in a piece of metal. The image was acquired using a Scanning Electron Microscope (SEM). Voids can occur for a number of reasons. When voids occur due to air bubbles becoming trapped when a material solidifies, it is commonly called porosity. When a void occurs due to the shrinkage of a material as it solidifies, it is called cavitation [17].
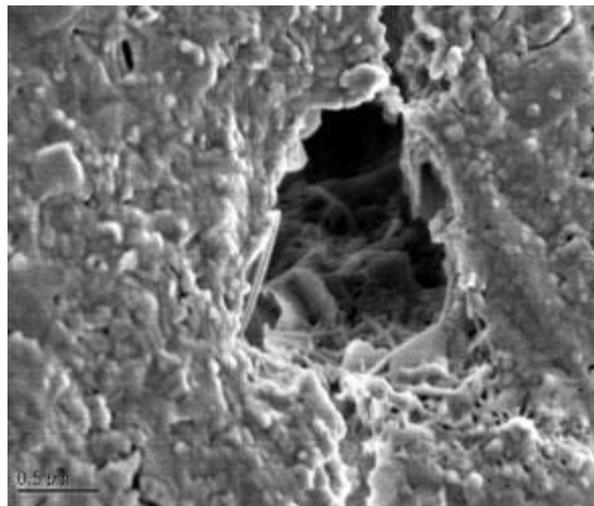
Figure I.17Voids (Bulk Defects). Image acquired using a Scanning Electron Microscope (SEM).

B- Lanthanum perovskites oxides La (Ni,Fe)O₃

Perovskites, of the general stoichiometry ABO_3 (where A is a trivalent rare earth metal ion and B is a trivalent first row transition metal ion), Find use in such applications as CO and NO oxidation catalysis, piezoelectrics and, more recently, high-temperature superconductors. The $ANiO_3$ class of perovskites is considered extremely important due to its electronic properties. Lanthanum nickel oxide $LaNiO_3$ is one of the better known of these materials but has not been studied extensively. Nickel usually adopts a formal charge of Ni^{+2} but can, in rare earth or alkaline earth ternary metal oxides, form the 3+ cation [18].

It was also reported that substituted $LaMO_3$ materials (where M is a transition metal) are interesting for the combustion of hydrocarbons, and in particular for methane. In particular, studies performed on $LaNiO_3$ evidenced that nickel into this type of structure stabilizes the active metal at high temperature and it limits the sintering and the coke formation. Moreover, the combination of nickel with a second element of the VIII group into a lanthanum phase (La (Ni,M)O₃) generally forms perovskite structures. Also in this case the strong interactions between nickel and the perovskite structure limits crystallites growth and carbon deposition [19].

Provendier et al. obtained $LaNiO_3$, $LaFeO_3$ and $LaNi_xFe_{1-x}O_3$ from aqueous solutions of the precursors with addition of oxalic acid and precipitation of the oxides, while Delmon et al. have proposed 30 years before a citrate route. More recently, Kienemann and co-workers have proposed a sol-gel method which allows the synthesis of $LaNi_xFe_{1-x}O_3$ perovskite single phase by using the propionic acid as the solvent. The critical point of this method is the decomposition of nitrate anions with violent NO_2 production which is especially observed in large scale preparations during the evaporation of the solvent. At this regards, this method is even more dangerous than the original route based on citrate because of the presence of propionic acid instead of water [19].

Norman and Morris reported diffractograms were Rietveld refined using the trigonal space group, $R\overline{3}C$, and crystallographic parameters for the $LaNiO_3$

system. For the modelling of the structure, the rhombohedric structure was used with the cell parameters (a = 5.4412, b = 5.4389 and c = 13.1715, α = β = 90◦ and γ = 119.8573◦) and the atomic positions of the ions in the unit cell given in. The corresponding representation is given in *Figure I.17*. The ions Ni^{3+} are in a perfect hexagonal environment, the La^{3+} ions are in a deformed environment of 12 O^{2-} [20].
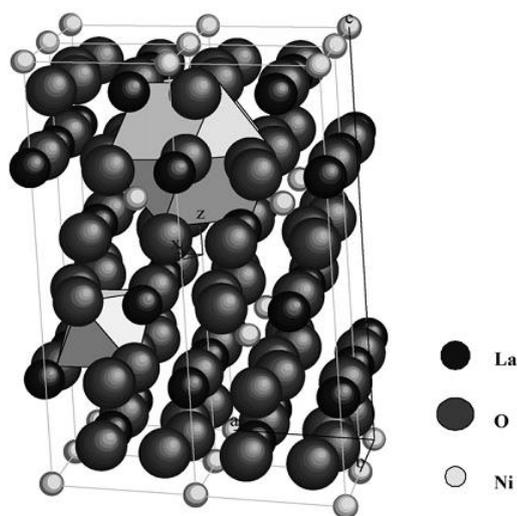
Figure I.18 *The structure of LaNiO₃ obtained with the parameters proposed by Norman and Morris.* [20]
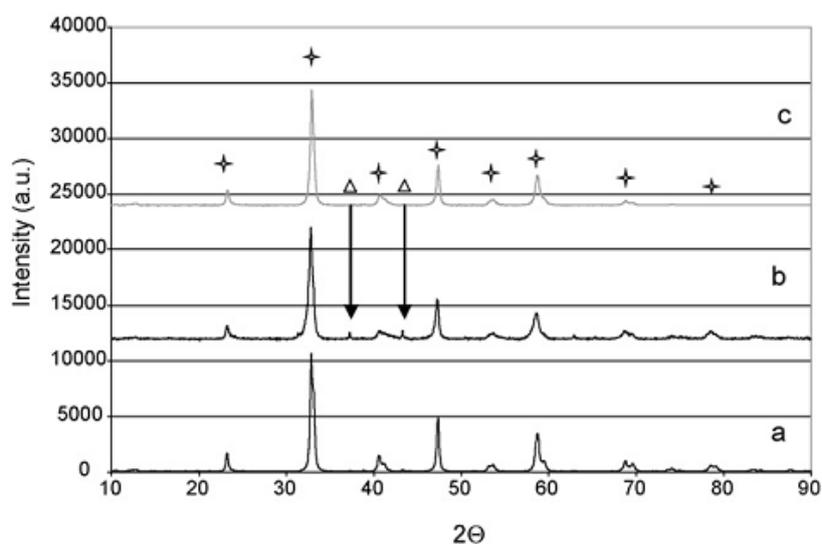
Figure I.19 *XRD of LaNiO₃ prepared by (a) citrate method; (b) Pechini's method; (c) propionate method after a treatment at 900 ˚C* [20].

The effect of substitution in the B site on the structural properties (XRD diffractograms) is shown in the following figures:
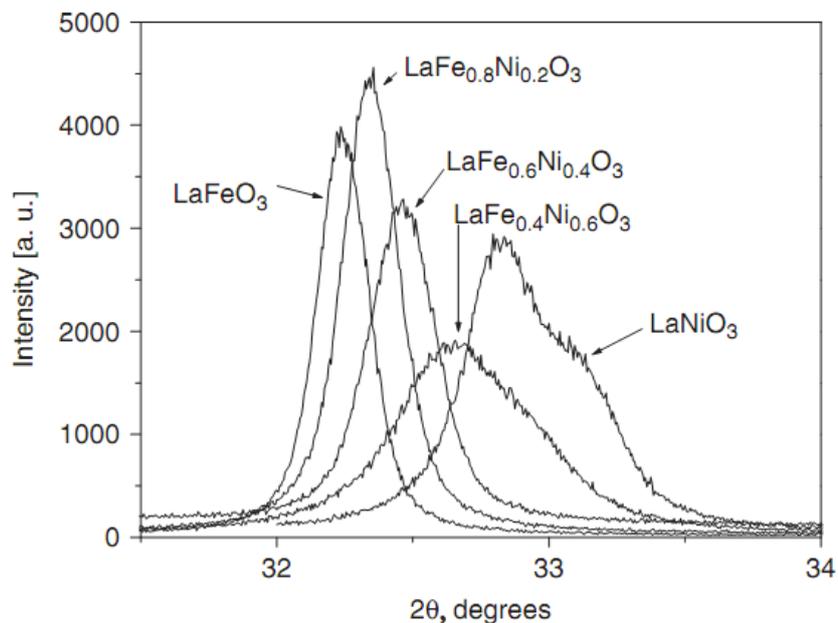
Figure I.20 XRD pattern of the largest peak for calcined

LaFe$_{1-x}$Ni$_x$O$_3$; x = 0, 0.2, 0.4, 0.6, 1. [21].
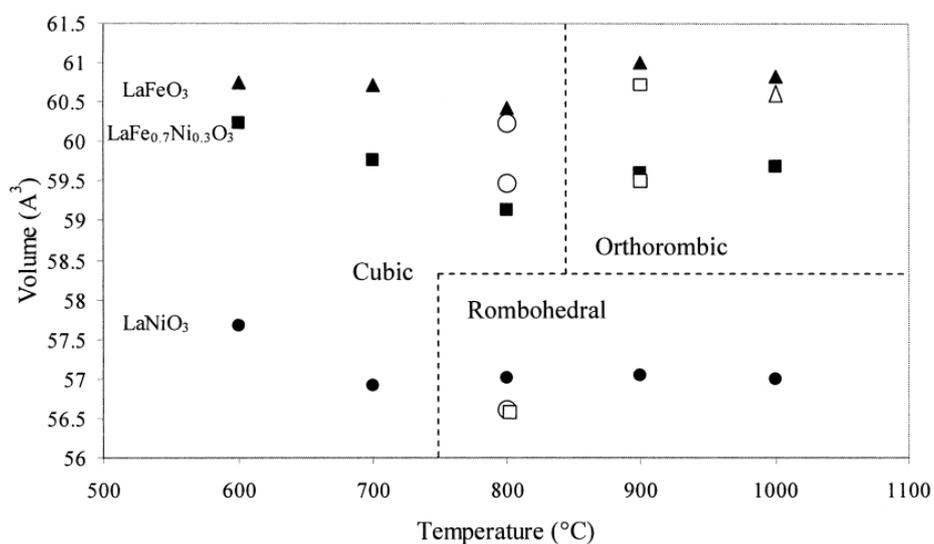
Figure I.21 The cell volumes, as a function of annealing temperature for all the samples (filled symbols). As a comparison Falcon et al. (□), Sangaletti et al. (Δ) and Provendier et al. results are also considered (○) [19].

C- Applications of perovskite oxides

I.5.1 catalytic and photocatalytic perovskites

Because of the variety of component elements and their high chemical stability, perovskite oxides have been also extensively studied as catalysts for various reactions. Two types of research trends clearly emerged from these characteristics. The objective of the first trend is the development of oxidation catalysts or oxygen -activated catalysts as an alternative to catalyst containing precious metals, whereas the second trend regards perovskite as a model for active sites. The stability of the perovskite structure allows preparation of compounds with an unusual valence state of elements or a high extent of oxygen deficiency.

Table I.2 summarizes the reactions studied by using perovskite oxides as catalysts. Evidently, the high catalytic activity of perovskite oxides is based partially on the high surface activity to oxygen reduction ratio or oxygen activation resulting from the large number of oxygen vacancies present.

Among the various catalytic reactions studied, those applicable to environmental catalysis (e.g., automobile exhaust gas cleaning catalyst) attract particular attention. Initially, it was reported that perovskite oxide consisting of Cu, Co, M n, or Fe exhibited superior activity to NO direct decomposition at higher temperatures. The direct NO decomposition reaction ($2NO = N_2 + O_2$) is one of the ''dream reactions'' in the catalysis field. In this reaction, the ease of removal of surface oxygen as a product of the reaction plays an important role, and due to the facility of oxygen deficiency present, perovskite oxides are active with respect to this reaction at high temperatures. I t is pointed out that doping is highly effective in enhancing NO decomposition activity. Under an oxygen-enriched atmosphere (up to 5 %), arelatively high NO decomposition activity was reported for Ba (La)Mn(Mg)O_3 perovskite. Recently, another interesting application of perovskite oxides as automobile catalysts has been reported, namely, the so- called intelligent catalysts [3].

Table I.2 Main catalytic reactions studied by using perovskite oxides [3].

Catalytic reaction		Example
Oxidation	CO, lower hydrocarbon, Methanol Catalytic combustion	$LaCoO_3$, $LaMnO_3$
deNOx	Selective reduction	$LaAlO_3$, $SrTiO_3$
	NO decomposition	$BaMnO_3$, $SrFeO_3$, $YBa_2Cu_3O_7$
	NO absorption	$LaAlO_3$, $BaCeO_3$, $BaFeO_3$
Hydrogenation	C_2H_4 hydrogenation	$LaCoO_3$
CH_4 coupling	Oxidative CH_4 coupling	$BaTiO_3$, $Ba_{0.5}Sr_{0.5}Fe_{0.2}Co_{0.8}O_3$
Oxygen electrode	Oxygen reduction (alkaline solution)	$LaCoO_3$, $LaMnO_3$
	Oxygen generation (alkaline solution)	$LaCoO_3$, $LaFeO_3$
	Cathode for Solid Oxide Fuel Cell	$LaCoO_3$, $LaMnO_3$
	Oxygen sensor	$LaCoO_3$, $LaMnO_3$
Gas sensor	Oxygen sensor, Humidity sensor, Alcohol Sensor	$SrTiO_3$, $BaSnO_3$, $LaCr(Ti)O_3$, $GdCoO_3$

The photocatalytic activities of ABO_3 perovskite-type oxides such as $BaCo_{0.5}Nb_{0.5}O_3$, Ca-doped $LaFeO_3$ and $SrFeO_{3-x}$ have been found in dye degradation and other catalysis. Besides, some other related compound oxides such as spinel-type oxides $CuAl_2O_4$, $BaCr_2O_4$ and CuM_2O_4 (M = Al, Cr, Mn, Fe and Co) also have been found to show photocatalytic activity in dye degradation and other catalysis. However, the reducibility of perovskite-type oxides and the related compound oxides, which can also cause the degradation activity in organic dye degradation, also cannot be ignored. These compound oxides such as perovskite-type oxides and spinel-type oxides usually contain various transition metal ions at A-site or B-site, and then the reducibility can be caused by these transition metal ions [22].

Catalysts with the perovskite structure exhibited higher catalytic activity as compared with the catalysts with the spinel and wolframite structures. $LaCoO_3$, which stabilizes Co(III) species in the perovskite structure, exhibited the highest catalytic activity in the photocatalytic water oxidation compared with $CoWO_4$, Co_3O_4 and $La_{0.7}Sr_{0.3}CoO_3$ which contain Co(II) or Co(IV) species in the matrices. The high catalytic reactivity of $LaCoO_3$ possessing perovskite structure was maintained in $NdCoO_3$ and $YCoO_3$ which exclusively contain Co(III) species. Thus, the catalytic activity of Co ions can be controlled by the additional metal

ions, which leads to development of highly reactive and robust catalysts for the photocatalytic water oxidation [23].
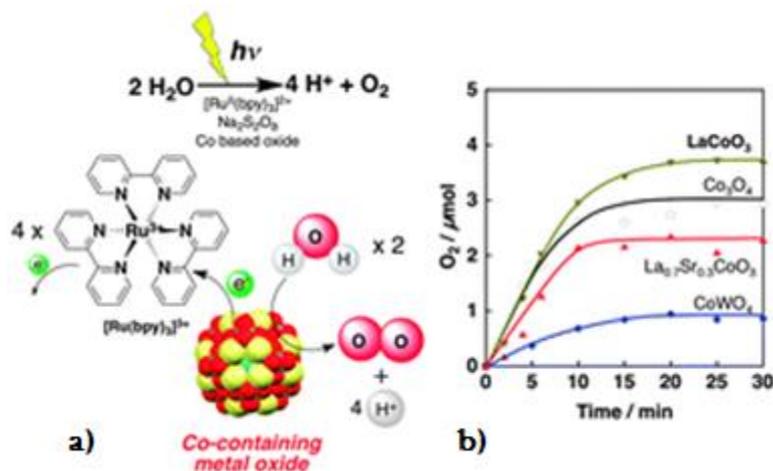
Figure I.22 *(a) Photocatalytic cycle of water oxidation with $Na_2S_2O_8$ and $[Ru(bpy)_3]^{2+}$ (b) Time courses of O_2 evolution under visible light irradiation (Xe lamp, $\lambda > 420$ nm) of a phosphate buffer solution.*

The nanocrystalline $LaMnO_3$ powders exhibited a good activity in the degradation of MO under UV light irradiation. The degradation percentage of MO after 36 h on $LaMnO_3$ powders was about 76%, indicating good photocatalytic activity of the obtained LaMnO3 powders [24].
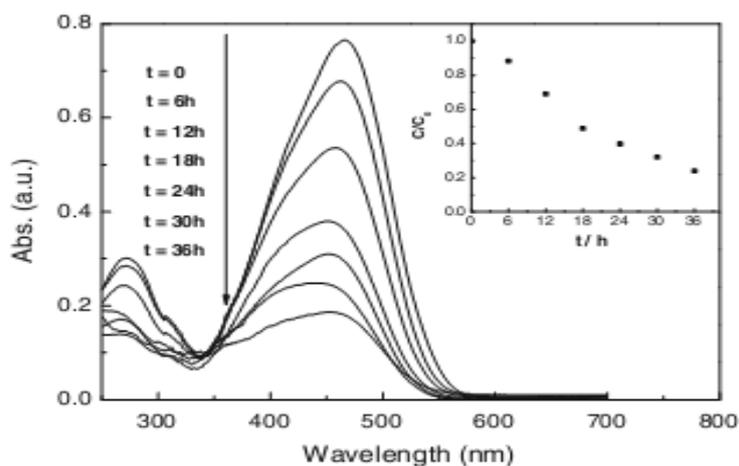
Figure I.23 *Photodegradation of MO monitored as the normalized concentration change versus irradiation time under UV light irradiation (insert) and absorption changes of MO solution on $LaMnO_3$ powders.* [24]

1. Nitogen cylinder   2. Regulator   3. Control panel
4. N$_2$ Mass flow controller   5. Gas inlet   6. Gas outlet
7. Water inlet   8. Water outlet   9. Inner Hg lamp
10. Quartz condenser   11. Glass reactor   12. Magnetic stirrer
13. Thermocouple   14. Moisture trap   15. Gas open/close valve
16. Reactor chamber   17. Gas sampling valve   18. Gas chromatograph
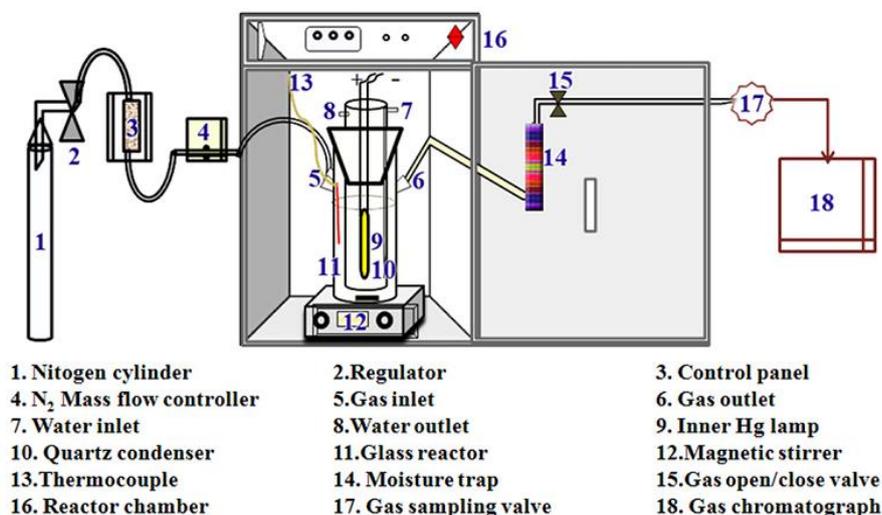
Figure I.24 *Schematic illustration of lab-scale evaluation systems for photocatalytic water splitting reactions.* [25]

I.5.2 Perovskites and Solar Cells

Although perovskites come from a seemingly different world of crystallography, they can be incorporated very easily into a standard OPV (or other thin film) architecture. While the best perovskite structures have been vacuum deposited to give better, more uniform film qualities, this process requires the co-evaporation of the organic (methylammonium) component at the same time as the inorganic (lead halide) components. The accurate co-evaporation of these materials to form the perovskite therefore requires specialist evaporation chambers that are not available to many researchers. This may also cause the practical issues of calibration and cross-contamination between organic and non-organic sources which would be difficult to clean.

However, the development of low temperature solution deposition routes offer a much simpler method to incorporate perovskites and can even be used with existing materials sets. Although the perovskite solar cells originally came out of DSSC research, the fact that they no longer require an oxide scaffold means the field is bifurcating and that many device architectures now look very similar to

thin film photovoltaics except with the active layers substituted with the perovskite. The key to enabling this is that the perovskite precursor materials use relatively polar solvents for deposition therefore an orthogonal solvent systems for the different layers can be fairly easily developed.

The below structure in (Figure I.25) represents a standard (non-inverted) perovskite solar cell based upon a standard glass/ITO substrates with metal back contact. All that is required to form a working device from the perovskite are two charge selective interface layers for the electrons and holes respectively.

Many of the standard interface layers from the world of organic photovoltaics work relatively well. For example PEDOT:PSS and the PTAA-class of polymers work well as hole interface layers while PCBM, C_{60}, ZnO and TiO_2 makes an effective electron interfaces. However, the field is so new that there is a vast archive of possible interface materials to be explored. Understanding and optimising the energy levels and interactions of different materials at these interfaces offers a very exciting area of research [26, 27, 28, 29].
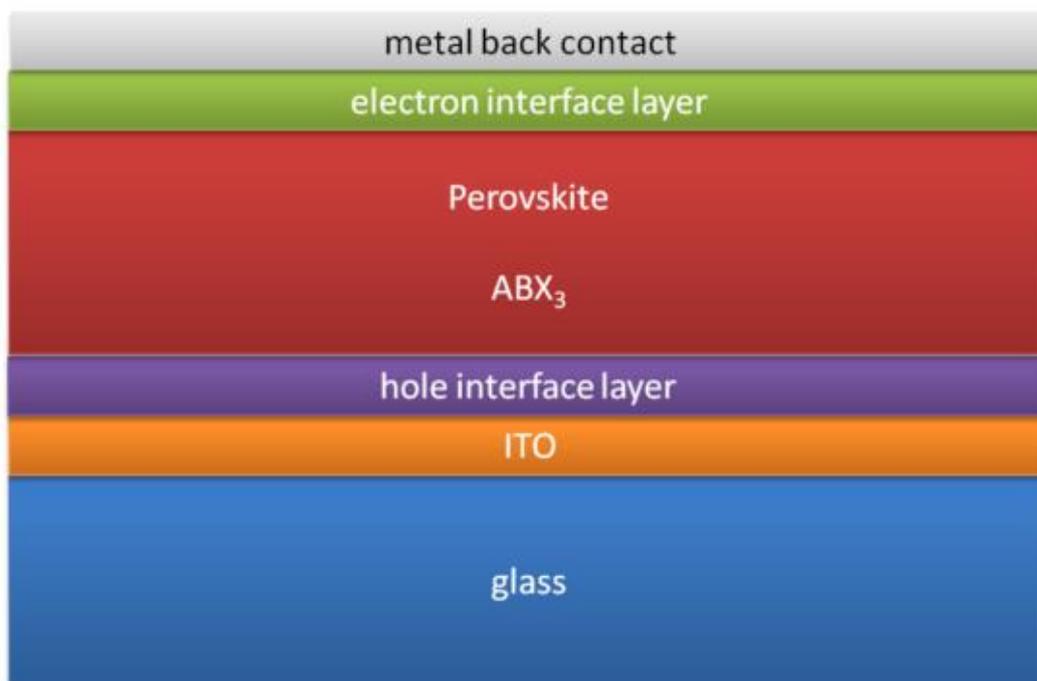
Figure I.25 *Generic structure of a standard (non-inverted) perovskite solar cell.*

I.5.3 Perovskites used in fuel cells

Fuel cells are devices that convert the chemical energy of a fuel directly into electrical energy and heat. The most common fuel is H_2, but other hydrocarbon compounds such as methanol, methane, natural gas, ethanol or others can also be used. A single cell is composed of three main components: anode, cathode and electrolyte [30, 31, 32, and 33].
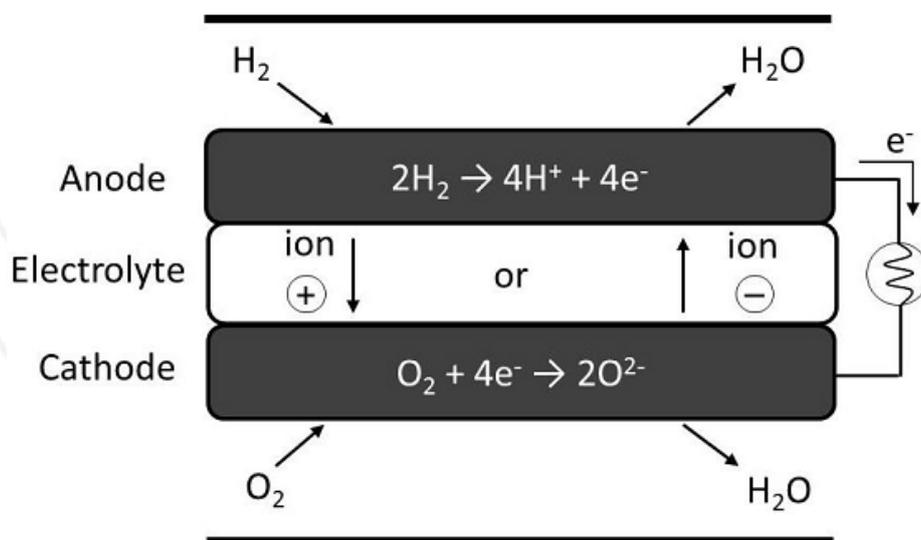
Figure I.26 *General operation scheme of a fuel cell running with H_2.* [30]

Due to their good stability and high electrical conductivity, it is also anticipated that $LaCrO_3$-based interconnect materials can be modified to anode materials through appropriate elemental substitution. Therefore, various transition metal elements e.g., (Ru, V, Mn, Fe, Co, Ni) with 3–10 atom % concentration were inserted into the Cr site of the perovskite lattice, and the Ni substitution seemed most promising. However, further investigations revealed nickel segregation from the perovskite lattice upon reduction, Thus, the observed good electrocatalytic activity of 10 atom % Ni-substituted (La, Sr)CrO_3 could be ascribed to the well-dispersed metallic Ni because the catalytic effect of only a small fraction of Ni in an anode has been demonstrated by other investigations. Recently, a high level Mn-substituted lanthanum strontium chromite, $La_{0.75}Sr_{0.25}Cr_{0.5}Mn_{0.5}O_{3-\delta}$ (LSCM),

was reported to display rather good electrochemical performance. The electrode polarization resistance at 900°C was 0.26 and 0.87Ω cm^2 in wet H$_2$ and wet CH$_4$, respectively. The observed good performance of this material could be linked to its possibly improved ionic conductivity by the 50 atom % Mn substitution for Cr because the ionic conductivity was found to be crucial for a mixed ionic/electronic conductor to have good electrocatalytic activity for fuel oxidation.1 In reducing atmosphere and at high temperatures, the reduction of Mn leads to an oxygen loss of as much as 0.25 mol O^{2-} per mol of LSCM, giving rise to a high concentration of oxygen vacancies. The strong ability of oxygen incorporation/release of LSCM upon redox cycling is essentially due to the presence of 50 atom % Mn, which is capable of adjusting its valence (+4, +3, and +2) according to the ambient oxygen partial pressure (p(O$_2$)), as in (La, Sr)MnO$_3$ [34].

I.5.4 Perovskites and biomedical science

To evaluate the ability of manganese perovskite nanoparticles (lanthanum-strontium manganite) to heat the tumor tissue in vivo under action of external alternating magnetic field. A magnetic fluid on the basis of nanoparticles of perovskite manganite was tested in the heating experiments using of alternating magnetic field of frequency 300 kHz and amplitude 7.7 kA/m. Guerin carcinoma was transplanted into the muscle of rat. Magnetic fluid was injected intramuscularly or intratumorally. Temperature was measured by copper-constantan thermocouple. As Results: Temperature of magnetic fluid was increased by 56 °C for 10 min of alternating magnetic field action. Administration of magnetic fluid into the muscle followed by alternating magnetic field resulted in the elevation of muscle temperature by 8 °C after 30 min post injection. Temperature of the tumor injected with magnetic fluid and treated by alternating magnetic field was increased by 13.6 °C on the 30 min of combined influence.

As Conclusion of this study: In vivo study with rat tissue has demonstrated that magnetic fluid of manganite perovskite injected in the tumor increases the tumor temperature under an alternating magnetic field. Obtained results emphasize that

magnetic fluid of manganite perovskite can be considered as effective inducer of tumor hyperthermia [35].

Figure I.27 *Photograph of rat in the special created net-hammock (the femur is located in the coil of magnetic field generator)* [35].

References

[1] Johnsson, M., & Lemmens, P. (2007). Crystallography and chemistry of perovskites. Handbook of magnetism and advanced magnetic materials.

[2] Marucco, J. F. (2004). Chimie des solides. EDP sciences.

[3] Ishihara, T. (Ed.). (2009). Perovskite oxide for solid oxide fuel cells. Springer Science & Business Media.

[4] Geller, S., Jeffries, J. B., & Curlander, P. J. (1975). The crystal structure of a new high-temperature modification of $YGaO_3$. Acta Crystallographica Section B: Structural Crystallography and Crystal Chemistry, 31(12), 2770-2774.

[5] Geller, S. (1956). Crystal structure of gadolinium orthoferrite, $GdFeO_3$. The Journal of Chemical Physics, 24(6), 1236-1239.

[6] Feteira, A., Gillie, L. J., Elsebrock, R., & Sinclair, D. C. (2007). Crystal structure and dielectric properties of $LaYbO_3$. Journal of the American Ceramic Society, 90(5), 1475-1482.

[7] Malashevich, A., & Ismail-Beigi, S. (2015). First-principles study of oxygen-deficient $LaNiO_3$ structures. Physical Review B, 92(14), 144102.

[8] Nelmes, R. J., & Kuhs, W. F. (1985). The crystal structure of tetragonal $PbTiO_3$ at room temperature and at 700 K. Solid state communications, 54(8), 721-723.

[9] Mabud, S. A., & Glazer, A. M. (1979). Lattice parameters and birefringence in $PbTiO_3$ single crystals. Journal of Applied Crystallography, 12(1), 49-53.

[10] Shirako, Y., Kojitani, H., Oganov, A. R., Fujino, K., Miura, H., Mori, D & Akaogi, M. (2012). Crystal structure of $CaRhO_3$ polymorph: High-pressure intermediate phase between perovskite and post-perovskite. American Mineralogist, 97(1), 159-163.

[11] West, D. V., & Davies, P. K. (2011). Triclinic and monoclinic structures of $SrLaCuNbO_6$ and $SrLaCuTaO_6$ double perovskites. Journal of Applied Crystallography, 44(3), 595-602.

[12] Roth, R. S. (1957). Classification of perovskite and other ABO_3-type compounds. J. Res. Nat. Bur. Stand, 58(2), 75-88.

[13] Pradhan, S., & Roy, G. S. (2013). Study the crystal structure and phase transition of $BaTiO_3$-A pervoskite. Researcher, 5(3), 63-67.

[14] Handbook, A. S. M. (1985). Metallography and microstructures,vol. 9ASM International. Materials Park, OH.

[15] Callister, J. (2004). WD "Material science and engineering an introduction," Sixth Edition, Jhon Wiley and Son. INC. New York.

[16] Michel, D. (2013). Sciences des matériaux, 3eme édition. Dunod, Paris.

[17] Mohammad J. R, (2005) Lecture Notes on Structure of Matter, Department of Physics, BUET, and Dhaka.

[18] Norman, A. K., & Morris, M. A. (1999). The preparation of the single-phase perovskite $LaNiO_3$. Journal of Materials Processing Technology, 92, 91-96.

[19] Bontempi, E., Garzella, C., Valetti, S., & Depero, L. E. (2003). Structural study of $La\,Ni_x\,Fe_{1-x}O_3$ prepared from precursor salts. Journal of the European Ceramic Society, 23(12), 2135-2142.

[20] Kuras, M., Roucou, R., & Petit, C. (2007). Studies of $LaNiO_3$ used as a precursor for catalytic carbon nanotubes growth. Journal of Molecular Catalysis A: Chemical, 265(1), 209-217.

[21] Erri, P., Dinka, P., & Varma, A. (2006). Novel perovskite-based catalysts for autothermal JP-8 fuel reforming. Chemical engineering science, 61(16), 5328-5333.

[22] Sun, M., Jiang, Y., Li, F., Xia, M., Xue, B., & Liu, D. (2010). Structure, dye degradation activity and stability of oxygen defective $BaFeO_{3-x}$. Materials transactions, 51(11), 1981-1989.

[23] Yamada, Y., Yano, K., Hong, D., & Fukuzumi, S. (2012). $LaCoO_3$ acting as an efficient and robust catalyst for photocatalytic water oxidation with persulfate.Physical Chemistry Chemical Physics, 14(16), 5753-5760.

[24] Li, Y., Yao, S., Xue, L., & Yan, Y. (2009). Sol–gel combustion synthesis of nanocrystalline LaMnO3 powders and photocatalystic properties. Journal of materials science, 44(16), 4455-4459.

[25] Labhasetwar, N., Saravanan, G., Megarajan, S. K., Manwar, N., Khobragade, R., Doggali, P., & Grasset, F. (2016). Perovskite-type catalytic materials for environmental applications. Science and Technology of Advanced Materials.

[26] Lee, M. M., Teuscher, J., Miyasaka, T., Murakami, T. N., & Snaith, H. J. (2012). Efficient hybrid solar cells based on meso-superstructured organometal halide perovskites Science, 338(6107), 643-647.

[27] Eperon, G. E., Burlakov, V. M., Docampo, P., Goriely, A., & Snaith, H. J. (2014). Morphological Control for High Performance, Solution-Processed Planar Heterojunction Perovskite Solar Cells. Advanced Functional Materials, 24(1), 151-157.

[28] Malinkiewicz, O., Yella, A., Lee, Y. H., Espallargas, G. M., Graetzel, M., Nazeeruddin, M. K., & Bolink, H. J. (2014). Perovskite solar cells employing organic charge-transport layers. Nature Photonics, 8(2), 128-132.

[29] http://www.ossila.com/pages/perovskites-and-perovskite-solar-cells-an-introduction.

[30] Diego Pereira Tarragó, Berta Moreno, Eva Chinarro and Vânia Caldas de Sousa (2016). Perovskites Used in Fuel Cells Perovskite Materials - Synthesis, Characterisation, Properties, and Applications. Dr. Likun Pan (Ed.), InTech, DOI: 10.5772/61465.

[31] Andújar, J. M., & Segura, F. (2009). Fuel cells: History and updating. A walk along two centuries. Renewable and sustainable energy reviews, 13(9), 2309-2322.

[32] Kirubakaran, A., Jain, S., & Nema, R. K. (2009). A review on fuel cell technologies and power electronic interface. Renewable and Sustainable Energy Reviews, 13(9), 2430-2440.

[33] Handbook, fuel cell. (2002). Prepared by EG&G Technical Services. Parsons Inc., and Science Applications International Corporation for the National Energy Technology Laboratory, USA.

[34] Fu, Q. X., Tietz, F., & Stöver, D. (2006). $La_{0.4}Sr_{0.6}Ti_{1−x}Mn_xO_{3−\delta}$ Perovskites as Anode Materials for Solid Oxide Fuel Cells. Journal of the Electrochemical Society, 153(4), D74-D83.

[35] Bubnovskaya, L., Belous, A., Solopan, A., Podoltsev, A., Kondratenko, I., Kovelskaya, A., ... & Osinsky, S. (2012). Nanohyperthermia of malignant tumors. II. In vivo tumor heating with manganese perovskite nanoparticles.Experimental oncology, 34(4), 336-339.

Second chapter

Synthesis methods, physicochemical characterization techniques and description of catalytic tests.

This chapter is devoted primarily to the description of the methods of preparation, second to characterization techniques and thirdly the catalytic tests: catalytic combustion CO.

II.1 Synthesis of perovskites

The physical properties of perovskites are greatly dependent on synthesis methods. In general, perovskites are usually formed at elevated temperatures, and the solid-state synthesis method is quite commonly used to prepare perovskites in pure form due to the availability of impurity-free precursors. Such synthesis methods are often suitable for electronic and electrical applications, but they pose problems when perovskites are subjected to surface-related studies. Obviously, perovskites with higher surface areas are required for catalytic and adsorption-related applications. Therefore, efforts have been devoted to synthesizing perovskites at lower temperatures with improved porosity. Close contact with precursors is essential for attaining the lowest possible synthesis temperature to achieve high surface area. The concept of maintaining high homogeneity of precursors (mixed-metal form) has been exploited for the purpose of achieving close contact with a view to synthesizing perovskites in the pure phase at low temperature. Low-temperature synthesis of perovskites results in higher surface area with smaller particle size, typically between the submicron and nano levels. Co-precipitation, citrate sol–gel, and solution combustion techniques have been commonly reported as ways to synthesize perovskites for catalytic applications. Serious attempts have been made to evaluate perovskite-based catalysts on a prototype scale, and the synthesis of perovskites on commercial honeycomb substrates has been successfully demonstrated. [1]

To obtain fine particles of perovskite oxides, some advanced synthetic methods that generally involve the use of organic compounds have been developed. However, the preparation of perovskite oxide powders with a large surface area is quite a difficult subject, and the BET surface area is generally smaller than 50 m^2/g. This restriction is easily understood by considering a simple relationship

between the specific surface area (S) an d the diameter of a spherical particle (D) [2]:

$$S = 6 / (\rho D)$$

Where ρ is the density of the sample. Figure II.1 shows the relationship between the geometrical surface area (S) of a spherical body and radius (D): the density of $LaCoO_3$ perovskite oxide is much lower than that of a general single oxide such as MgO or Al_2O_3.
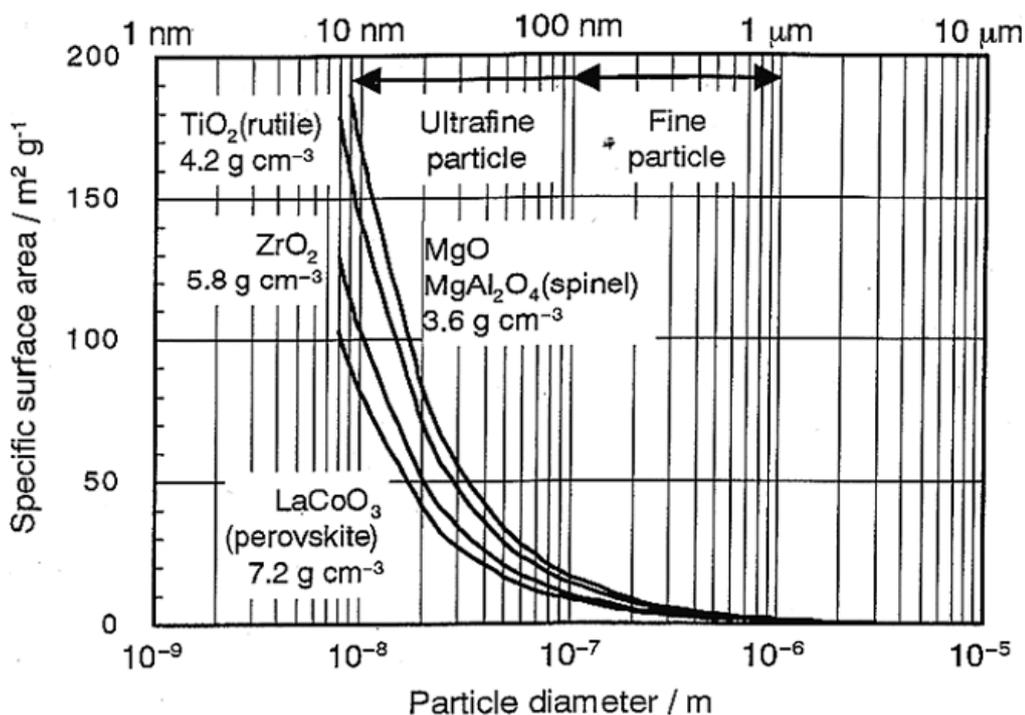
Figure II.1 Relationship between geometrical surface area (S) of a spherical body and radii (D) [2]

II.1.1 Sol–gel method

This synthetic route based on the use of the complexing agent and in particular of citric acid for the preparation. The complexing agents used are varied: citric acid, EDTA, malic acid, propionic acid, sucrose, ascorbic acid … the preparation method is schematically shown in Figure II.2. It provides solids with surface area (~20-40 m^2/g). [3, 4]
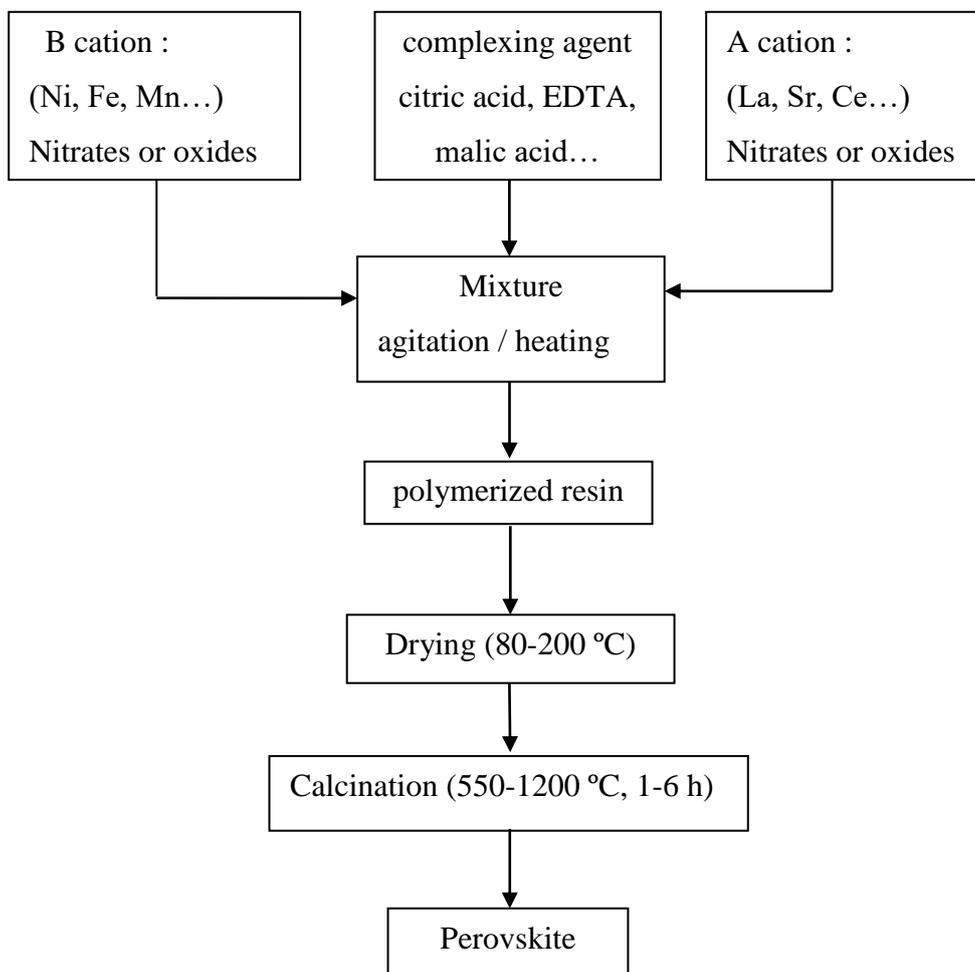
Figure II.2 general diagram of sol-gel route.

$LaNi_{1-x}Co_xO_3$ perovskite-type oxides have been successfully synthesized by the sol–gel citrate method employing $La(NO_3)_3 \cdot 6H_2O$, $Ni(NO_3)_2 \cdot 6H_2O$, $Co(NO_3)_2 \cdot 6H_2O$, citric acid, and ammonium carbonate as materials. The decomposition of the precursor complex at 800 °C for 5 h led to the formation of $LaNi_{1-x}Co_xO_3$ powder as confirmed by XRD [5]. The effect of the preparation methods in the perovskite structure formation and the effect of partial substitution of Ni for Co in the B sites of $LaNiO_3$ perovskites on the structural, morphological and surface properties were studied by *Silva et al*, using lanthanum, nickel and cobalt nitrates, citric acid and using ethylenediaminetetraacetic acid (EDTA) as

chelating agent [6]. The 'amorphous citrate' gel method is a simple and easy to use technological method that allows the preparation of single-phase ceramic powders of $LaNiO_3$ with controlled grain size by thermal annealing. *LE, Ngo Thi Hong* obtained single-phase $LaNiO_3$ nanopowders at 650 °C with particle sizes from 30 to 65 nm at annealing temperatures from 650 to 750 °C, while the crystalline size, given by XRD measurements, varied from 10 to 15 nm [7].

II.1.2 Sol-gel combustion synthesis (SGC).

This method based on the combustion of the precursor to form the perovskite phase. an acidic solution containing the metal ions (La, Fe, Ni ..) and the fuel (sucrose, urea, citric acid, glycine, ...) is heated to obtain a resin and then dried.
The solid foam obtained is then ignited in a reactor, and the ashes produced after burning ground to get the final product. this product can be a pure perovskite phase or require Additional calcination [8].

Gel formed by heating a solution containing lanthanum(III) nitrate, nickel(III) nitrate and sucrose underwent self-sustaining smoldering type of combustion synthesis upon continued heating on a hot plate. The combustion was of complex nature, as evidenced by TGA–DSC plot. The TGA–DSC plot of the dried gel revealed that combustion reaction took place in two steps, one at 160 °C and the other at 350–525 °C. Variation in crystallite size was observed as the calcinations temperature increased, which was reflected in the values of specific surface area. TEM analysis revealed that hard agglomerates of the powder range from 20 to 60 nm. The powders calcined at different temperatures showed different behavior to optical absorption in the UV–visible range of optical spectrum, which is basically due to the various crystallographic structures. Phase pure rhombohedral $LaNiO_3$ can be used as electrode material since it has electronic conducting property. SEM study showed that sucrose combustion route produces highly agglomerated porous powder [9].
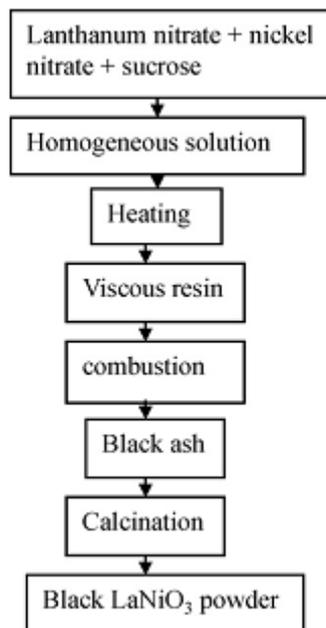
Figure II.3 *Process flow chart.* [9].

New supports for the LaNiO$_3$ oxide were successfully made use of Ni foam. It was found that the oxide preparation procedure by the self-combustion method, using citric acid, in combination with the use of Ni foam as support, enhanced the electrode surface properties [10].

A photocatalyst LaNiO$_3$ with perovskite structure was synthesized via a sol–gel combustion technique by *Li Yuanyuan et al.* they studied The effect of calcination process on the crystallinity, structure and visible-light-driven photocatalytic property of LaNiO$_3$. The results showed that a single perovskite phase of LaNiO$_3$ was obtained by suitable calcination process. The powder had high surface area [11].

II.2 Characterization Methods

II.2.1 X-ray diffraction

II.2.1.1 Introduction

The X-ray diffraction (XRD) is one of the main analytical techniques non-destructive of crystalline materials. The interaction of monochromatic radiation (X) with the ordered material produces a diffraction pattern which is characteristic of the material under investigation and can be considered a 'fingerprint'. The geometric crystallography shows that any ordered three-dimensional assembly of atoms can be described by a stack in the three spatial directions of a fundamental unit called a unit cell. This allows to identify different lattice planes, each of which is identified by its Miller indices (hkl noted see during geometric crystallography). In the crystal, they form families of parallel and equidistant planes each other a distance called interplanar distance (denoted d_{hkl}), unique to each family and depending on the dimensions of the unit cell (a, b, c, α, β, γ).

The lattice structure of crystals and the vibratory nature of X-rays whose wavelengths (~ 1Å) are of the same order of magnitude as the interplanar spacings allow the diffraction phenomenon. If an X-ray beam is deflected by an angle 2θ by the material, then the incident and reflected beams make an angle θ with only one set of lattice planes of the studied material, the interplanar spacing is connected to the angle θ by the law of Bragg: $2d_{hkl} \sin\theta = \lambda$

Where λ is the wavelength of the X-radiation used.
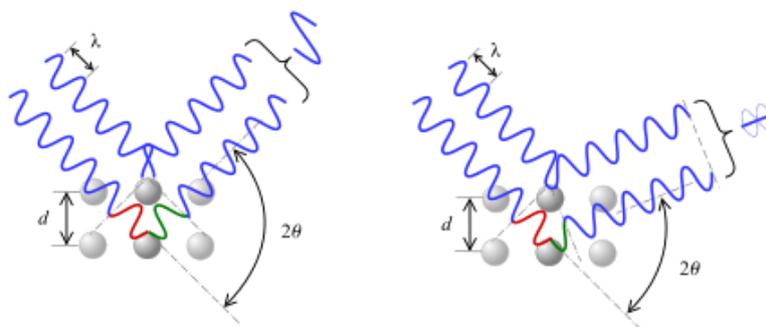
Figure II.4 *According to the 2θ deviation, the phase shift causes constructive (left figure) or destructive (right figure) interferences.*

If a polycrystalline sample is subjected to X-monochromatic beam, due to the random sharing and statistic of many microcrystals constituent of the sample, all lattice planes of families will be diffraction position simultaneously. Experimentally, the collection (electronic counter or photographic film) of all the diffracted beams leads to a diffraction pattern or diffractogram .

The angular position of the diffracted beams is a function of the geometry of the unit cell characteristic of the crystallized substance. Bragg's equation reflects this aspect of the X-ray diffraction intensity of the diffracted beams (integrated peak area) in turn depends on the nature (number of electrons) and the position of the atoms in this mesh elementary.

Indeed, the X electromagnetic radiation interacts with the electron clouds of the atoms constituting the material. It is therefore understood that the intensity of a diffracted beam is dependent on both the position of the atom and an electronic specific factor (fj) of the electronic structure of the considered atom.

This means that two substances crystallized in the same unit cell but whose constituent atoms are different or occupy different sites will present some similar patterns from the viewpoint of the intensity distribution of diffracted beams (unless atoms have scattering factors fj very similar).

Physical theories make today well aware of the phenomenon of X-ray diffraction. Intensity of the diffracted beam is described by a mathematical expression linking the coordinates of the atoms of the mesh, electronic distribution factor (fj) and indices h, k, l of the diffraction position plans family (Miller indices) [12].

$$I_{hkl} = K * \mid F(hkl) \mid^2$$

where $\mid hkl \mid$ is the intensity of a diffraction peak, k is a constant which includes experimental parameters, the Lorentz factor, polarization, multiplicity (m) of a family of planes (eg in a cubic unit cell , the line (100) at a multiplicity of 6 because 6 following plans are equivalent (thus even d_{hkl} same angular position

on the diffractogram): (100) (010) (001) (-100), (0-10) and (00-1)) and the structure factor which includes Debye U factors (thermal agitation).

$$F(hkl) = \sum_{j=1}^{n} f_j \exp(2\pi i(hx_j + ky_j + lz_j)) \bullet \exp(-\frac{8\pi^2 U \sin^2 \theta}{\lambda^2})$$

Where n is the total number of atoms in the unit cell, $8\pi 2\ U = B$, is called thermal agitation factor. Its order of magnitude: from 1 to 5 A.

It is theoretically possible to calculate and even simulate diffraction.It allows tracing two types of information:

- The analysis of a diffraction pattern using the Bragg equation and geometric crystallography to determine the geometry of the unit cell.

- analyzing the relative intensities of the diffracted beams may allow, under certain conditions, to rise to the position of atoms in the unit cell (for structural resolution).

II.2.1.2 Calculation of average crystallite size

We can use Scherrer methods [13, 14, and 15] to estimate the average crystallite size in the field 2-100 nm. In many cases, this approximate method is sufficient to characterize the catalysts. In addition, it is simple and quick to implement.The Scherrer equation can be written as: $D = \frac{K\lambda}{\beta \cos\theta}$, where:

- D is the mean size of the ordered (crystalline) domains, which may be smaller or equal to the grain size;

- K is a dimensionless shape factor, with a value close to unity. The shape factor has a typical value of about 0.9, but varies with the actual shape of the crystallite;

- λ is the X-ray wavelength;

- β is the line broadening at half the maximum intensity (FWHM), after subtracting the instrumental line broadening, in radians. This quantity is also sometimes denoted as $\Delta(2\theta)$;

- θ is the Bragg angle.
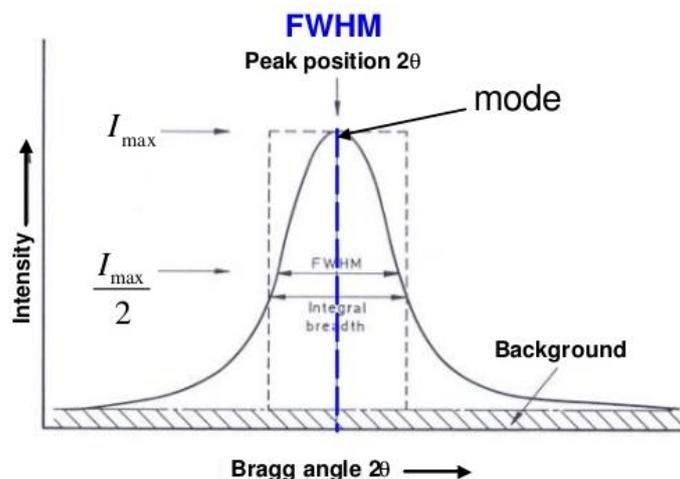
Figure II.5 *Peak width-full width at half maximum.*

II.2.1.3 Apparatus used

XRD Patterns were collected on a Bruker AXS D8- advance diffractometer (Institute of Catalysis and Petrochemical ICP-CSIC University Autonoma. Madrid) employing Cu Kα radiation. In all diffractograms, a step size of 0.02° (2θ) was used with a data collection time of 15 s.

Figure II.6 *Bruker D8 Advance diffractometer.*

II.2.2 Infrared spectroscopy

II.2.2.1 Introduction

Infrared spectroscopy is certainly one of the most important analytical techniques available to today's scientists. One of the great advantages of infrared spectroscopy is that virtually any sample in virtually any state may be studied. Liquids, solutions, pastes, powders, films, fibres, gases and surfaces can all be examined with a judicious choice of sampling technique. As a consequence of the improved instrumentation, a variety of new sensitive techniques have now been developed in order to examine formerly intractable samples. Infrared spectrometers have been commercially available since the 1940s. At that time, the instruments relied on prisms to act as dispersive elements, but by the mid 1950s, diffraction gratings had been introduced into dispersive machines. The most significant advances in infrared spectroscopy, however, have come about as a result of the introduction of Fourier-transform spectrometers.

This type of instrument employs an interferometer and exploits the well established mathematical process of Fourier-transformation. Fourier-transform infrared (FTIR) spectroscopy has dramatically improved the quality of infrared spectra and minimized the time required to obtain data. In addition, with constant improvements to computers, infrared spectroscopy has made further great strides. Infrared spectroscopy is a technique based on the vibrations of the atoms of a molecule. An infrared spectrum is commonly obtained by passing infrared radiation through a sample and determining what fraction of the incident radiation is absorbed at a particular energy. The energy at which any peak in an absorption spectrum appears corresponds to the frequency of a vibration of a part of a sample molecule. In this introductory chapter, the basic ideas and definitions associated with infrared spectroscopy will be described. The vibrations of molecules will be looked at here, as these are crucial to the interpretation of infrared spectra [16].

II.2.2.2 Inorganic Molecules

As with organic compounds, inorganic compounds can produce an infrared spectrum. Generally, the infrared bands for inorganic materials are broader, fewer

in number and appear at lower wavenumbers than those observed for organic materials. If an inorganic compound forms covalent bonds within an ion, it can produce a characteristic infrared spectrum. The bands in the spectrum of ionic or coordination compounds will depend on the structure and orientation of the ion or complex [16].

Several factors have an impact on the appearance of the infrared spectra of inorganic compounds. The crystal form of the compound needs to be considered. Crystalline lattice bands manifest themselves in the far-infrared region and changes to the crystal structure will be observed in the spectra. The consequence is that non-destructive sampling techniques are preferred for such samples. Techniques such as alkali halide discs or mulls can produce pressure-induced shifts in the infrared bands of such materials. The degree of hydration of an inorganic compound is also a factor when interpreting spectra. The water molecules that are incorporated into the lattice structure of a crystalline compound produce characteristic sharp bands in the 3800–3200 and 1700–1600 cm^{-1} regions, due to O–H stretching and bending, respectively.
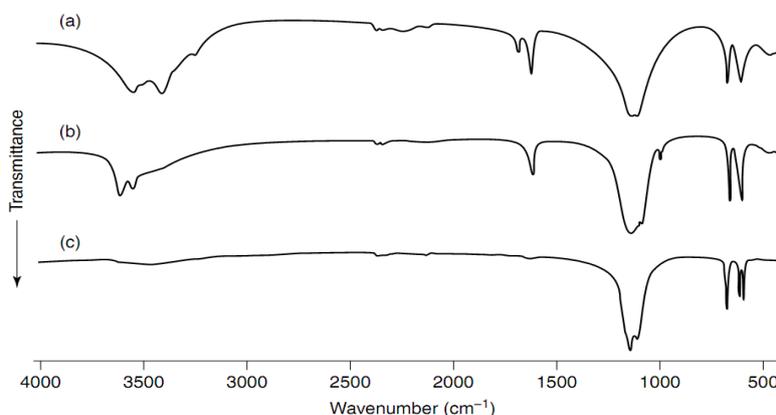
Figure II.7 Infrared spectra of (a) dihydrate, (b) hemihydrate and (c) anhydrous CaSO$_4$ [16].

The lattice environment of the water molecules determines the position of the infrared bands of water and whether they are single or split. The hydroxy stretching bands in the 3800–3200 cm^{-1} range show unique patterns that may be used to characterize the compositions of hydrated inorganic compounds [16].

In spite of the differences in cell symmetry and composition of the investigated materials, their IR spectra are very similar, showing two strong and well-defined absorption bands, typical of perovskite materials. These bands are mainly assigned to the antisymmetric stretching and deformational modes of the octahedral BO_6 moieties. Because both, the B and B' cations are present as octahedral MO_6 building blocks, strong vibrational coupling between them may be expected. On the other hand, the M–O bonds of these units, involving metal cations of charges ranging between +3 and +6 are undoubtedly stronger than those belonging to the 12-coordinated A(II)–O units. On the basis of this simple argument one may predict that the MO_6 units behave as approximately ''isolated'' groupings that dominate the spectroscopic behavior. In some cases, if the charges and/or masses of the B and B' cations are very different it should be possible to make some additional differentiation between BO_6 and $B'O_6$ vibrators [17].
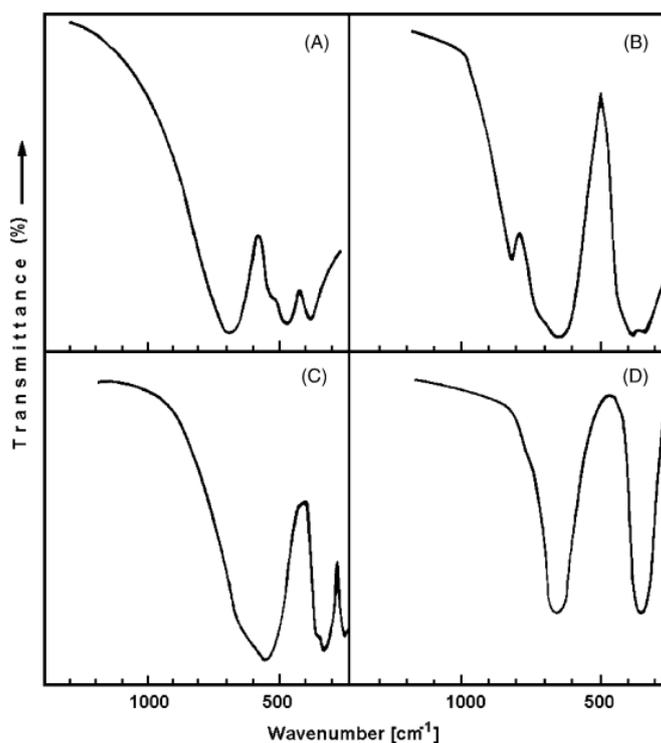
Figure II.8 *Typical FT-IR spectra of some of the investigated perovskite materials: Ca_2AlTaO_6 (A), Sr_2MgMoO_6 (B), Ba_2YNbO_6 (C) and Ba_2InSbO_6 (D)* [17].

II.2.2.3 Apparatus used

Infrared transmission spectra were performed on a Fourier transform spectrometer (FTIR) Shimadzu 8400S (chemistry laboratory, Department of Material Sciences, University of Biskra). A granular technique employing KBr (1 mg of sample added to 200 mg of KBr) was used and the spectra were recorded in the 400-4000 cm-1 range.

Figure II.9 Fourier transform spectrometer (FTIR) Shimadzu 8400S.

II.2.3 Thermal analysis

Thermal analysis, Techniques in which a physical property of a substance is measured as a function of temperature whilst the substance is subjected to a controlled temperature programme. In addition to being more accurate, this definition has the advantage that it can be adapted to define any thermoanalytical technique by alteration of only a few words in each instance[18].

II.2.3.1 Thermogravimetry (TG):

A technique in which the mass of a substance is measured as a function of temperature while the substance is subjected to a controlled temperature program. The record is the thermogravimetric or TG curve; the mass should be plotted on the ordinate decreasing downwards and temperature (T) or time (t) on the abscissa increasing from left to right [19].
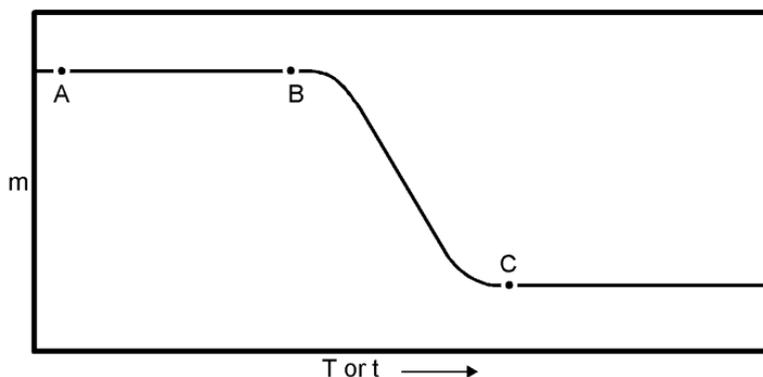
Figure II.10 Formalized TG Curve.

II.2.3.2 Differential Thermal Analysis (DTA)

A technique in which the temperature difference between a substance and a reference material is measured as a function of temperature whilst the substance and reference material are subjected to the same controlled temperature program. The record is the differential thermal or DTA curve; the temperature difference (ΔT) should be plotted on the ordinate with endothermic reactions downwards and temperature or time on the abscissa increasing from left to right. The term quantitative differential thermal analysis (quantitative DTA) covers those uses of DTA where the equipment is designed to produce quantitative results in terms of energy and/or any other physical parameter [20].
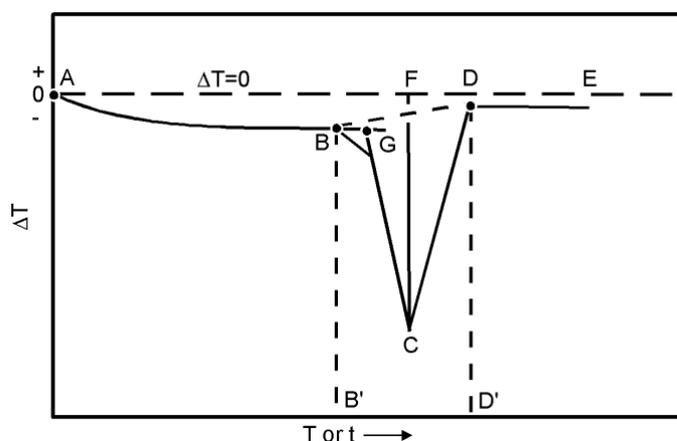
Figure II.11 Formalized DTA Curve.
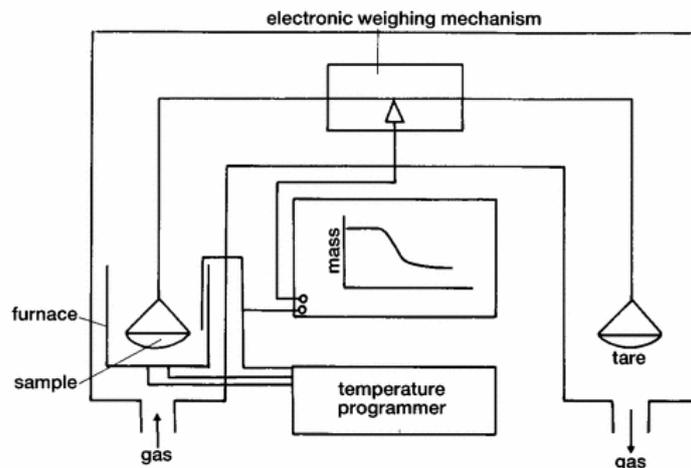
Figure II.12 *Schematic thermobalance* [20].

II.2.3.2.1 Apparatus used

Thermogravimetric and differential thermal analyses (TGA-DTA) of the precursor decomposition were performed on a Perkin-Elmer TGA7 and a Perkin-Elmer DTA7 devices (Institute of Catalysis and Petrochemical ICP-CSIC University Autonoma. Madrid), respectively, from 20 to 900 ℃ at a heating rate of 20 ℃ min^{-1} and under an air flow of ca. 60 ml min^{-1}.

Figure II.13 *Perkin-Elmer TGA7 and a Perkin-Elmer DTA7 devices*.

II.2.4 Determination of the specific surface area by BET method

II.2.4.1 Principle

The gas adsorption method is a method for measuring the amount of gas adsorbed on the surface of a powder sample as a function of the pressure of the adsorbate gas, and is used to determinate the specific surface area of a powder sample. Measurement are usually performed at the boiling point of liquid nitrogen (-196 °C).

When the gas is physically adsorbed by the powder sample, the following relationship holds when P/P_0 is in the range of 0.05 to 0.3 for pressure P of the adsorbate gas in the equilibrium for the volume gas adsorbed, V_a [21].

$$\frac{1}{V_a \left(\frac{P_0}{P} - 1 \right)} = \frac{(C-1)}{V_m C} \times \frac{P}{P_0} + \frac{1}{V_m C}$$

Where:

- P: Partial vapor pressure of adsorbate gas in equilibrium (kPa)
- P_0: Saturated pressure of adsorbate gas at -196 °C (kPa)
- V_a: volume of adsorbate gas at equilibrium (mL)
- V_m: volume of adsorbate gas in a monolayer (mL)
- C: Dimensionless constant related to the enthalpy of adsorption and condensation of the adsorbate gas.

The specific surface area, S, is determined from V_m, the volume of gas adsorbed in a monolayer on the sample.

$$S = \frac{V_m \times N \times a}{m \times 22400}$$

- S: Specific surface area (m^2/g)
- N: Avogadro constant
- a: Effective cross-sectional area of one adsorbate molecule (m^2)
- m: Mass of the test powder (g)

II.2.4.2 Apparatus used

The specific surface area of the samples (S_{BET}) was determined by applying the BET method to nitrogen adsorption/desorption isotherms recorded at -196 °C, using a Micrometrics apparatus model ASAP-2000 (Institute of Catalysis and Petrochemical ICP-CSIC University Autonoma. Madrid).

Figure II.14 *Micrometrics apparatus model ASAP-2000.*

II.2.5 Particle Size Distribution and its Measurement

II.2.5.1 Introduction

The population of particles in a powder, as described by its particle size distribution (PSD), affects the properties of a powder and dispersions in many important ways. For example, in industrial applications, it determines the setting time of cement, the hiding power of pigments, the activity of catalysts, the taste of food, and the sintering shrinkage of metallurgical compositions. The relevance to the Pharmaceutical industry is that the stability, aesthetics, rate of absorption and total bioavailability, to name a few properties, are all strongly affected by the size

of the particles that comprise the powder or dispersion. In addition, regulatory agencies are becoming increasingly aware of the importance of the PSD and requiring developers to have greater control and understanding of this aspect of their drug products. So, what is Particle Size? Surprisingly, it is not a question that can be easily answered. This is because in the real world, depending upon the material properties, conditions of manufacture and storage, three distinct species (Figures 1 and 2) will always exist in any powder, wet or dry [22,23], the existence of which results from a variety of different binding mechanisms. Please note that we are talking about solid particles dispersed alone or in liquids and not, for instance, the internal phase of an emulsion. The three species are:

- Primary particles: These are inorganic or organic structures held together by atomic or molecular bonding. They are the "fundamental" particles; they cannot be separated into smaller particles except by the application of ultrahigh energy. In any sample they are usually present at only a fraction of a percent.

- Aggregates: These comprise two or more primary particles tightly bound together by rigid chemical bonding resulting from sintering or cementation, which is the coalescence of particles by processes other than heat/pressure, i.e., precipitation of ionic salts onto surfaces during manufacture. Aggregates are typically formed when powders are heated, compressed, or dried from suspension. They have a large interfacial area of contact between each particle and the force necessary to rupture these bonds is considerable. Aggregates constitute, for all practical purposes, the largest single fraction of any particle size distribution (PSD) that one can hope to achieve in formulation.

- Agglomerates. These are collections of aggregates, loosely held together at point-to-point contact by weak electromagnetic forces, van der Waals forces, mechanical friction, and interlocking. Agglomerates are formed when fine particles are handled, shaken, rolled or stored undisturbed in a

single position. They can readily be broken apart with proper dispersion techniques. During the formulation process, while it is critical to obtain an initial suspension in which the particles are narrowly distributed, it is equally important that the PSD remains the same at the end of any formulating process. The end result of a correct dispersing process is to effectively narrow the PSD: to reduce the agglomerates to aggregates [23].
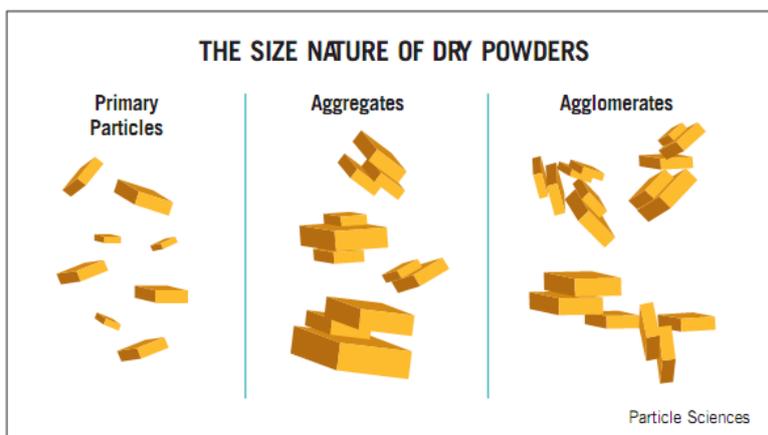
Figure II.15 the size nature of dry powder.
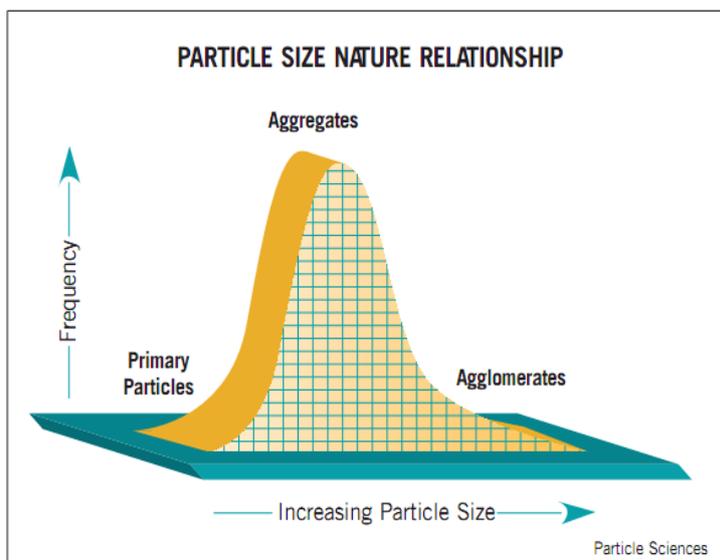
Figure II.16 particle size relationship.

II.2.5.2 Principle

Laser diffraction measures particle size distributions by measuring the angular variation in intensity of light scattered as a laser beam passes through a dispersed particulate sample. Large particles scatter light at small angles relative to the laser beam and small particles scatter light at large angles. The angular scattering intensity data is then analyzed to calculate the size of the particles responsible for creating the scattering pattern, using the Mie theory of light scattering. The particle size is reported as a volume equivalent sphere diameter [24].

II.2.5.3 Apparatus used

Powder size distribution was characterized with a laser particle size analyzer (Mastersizer 2000, Malvern). (chemistry laboratory, Department of Material Sciences, University of Biskra).

Figure II.17 Mastersizer 2000, Malvern.

II.2.6 X-ray photoelectron spectroscopy (XPS)

II.2.6.1 Introduction

X-ray photoelectron spectroscopy works by irradiating a sample material with monoenergetic soft x - rays causing electrons to be ejected the identification of the elements in the sample can be made directly from the kinetic energies of these ejected photoelectrons [25]. The relative concentrations of elements can be determined from the photoelectron intensities. An important advantage of XPS is

its ability to obtain information on chemical states from the variations in binding energies, or chemical shifts, of the photoelectron lines.

II.2.6.2 History

X-ray Photoelectron Spectroscopy (XPS) was developed in the mid -1960s by Kai Siegbahn and his research group at the University of Uppsala, Sweden. The technique was first known by the acronym ESCA (Electron Spectroscopy for Chemical Analysis). The variation of photopeak energy with chemistry allowed the development of this surface sensitive chemical analysis method. The advent of commercial manufacturing of surface analysis equipment in the early 1970s enabled the placement of equipment in laboratories throughout the world. In 1981, Siegbahn was awarded the Nobel Prize for Physics for his work with XPS [25].

II.2.6.3 Principle

Photoelectron spectroscopy is based on the incoming photon / electron-out process, and in many ways, this process remains a relatively simple physical phenomenon, at least in comparison with the Auger electron emission.

The energy of a photon is given by the Einstein relation: $E = h\nu$

Where h is Planck's constant (6.62×10^{-34} J s) and ν is the frequency of the radiation (s^{-1} or Hz).

Although this is not always the case, generally it used sources of monochromatic radiation in experiments photoemission. The incident photons then have a fixed energy. In XPS, the photons are absorbed by an atom in a molecule or solid. This leads to ionization and emission of a heart of electron (inner layers). The kinetic energy of the emitted photoelectrons can be measured by an electron energy analyzer, such as a concentric hemispherical analyzer (CHA), to finally record a spectrum of the number of photoelectrons emitted according to their kinetic energy [26].

The photoionization process can be described in several ways. One of them, whereas an atom or molecule A is to take:

$$A + h\nu \longrightarrow A^+ + \acute{e}$$

The energy conservation law then requires the following equation:

$$E(A) + h\nu = E(A^+) + E(\acute{e})$$

The energy of the electron E (e) is essentially in the form of kinetic energy (KE for kinetic energy). We can then rewrite the above equation as photoelectron KE:

$$KE = h\nu - [E(A^+) - E(A)] = h\nu - BE$$

The term in braces is simply the difference in energy between the atom ionized and the neutral atom, so-called "binding energy" (BE for binding energy) of the electron. More schematically, we can also write the photoionization process as follows:
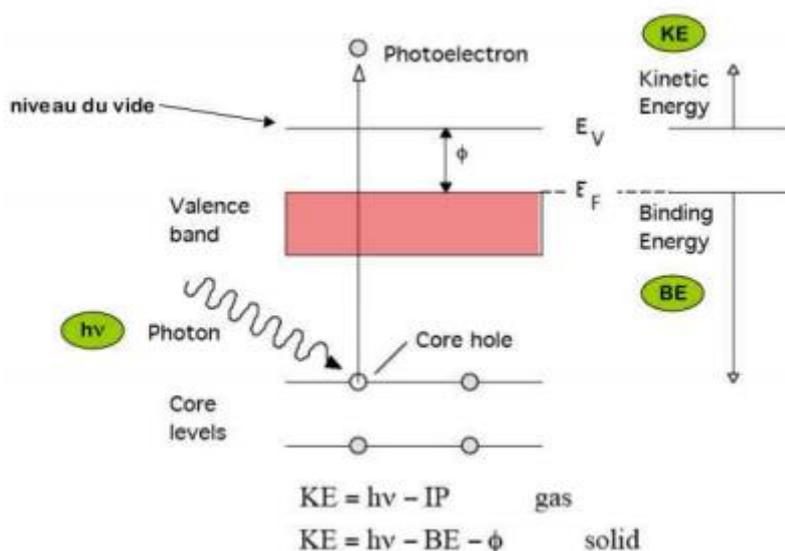
Figure II.18 *Process of heart photoionization of electrons.*

The binding energy BE of the energy levels in solids is conventionally measured relative to the Fermi level of the solid, rather than the vacuum. This implies a correction to the above equations in order to take account of the work function (work function) of the solid. In the following discussion, this correction will be neglected. We then, set $\phi = 0$.

So atomic orbital of each heart of an element has a specific BE binding energy, that is to say each element will result in a set of peaks in the spectrum of photoelectrons whose kinetic energy KE is determined by energy of the photons

and the respective binding energies. The presence of peaks at energies data then indicates the presence of a specific component in the sample considered. In addition, the intensity of the peaks is related to the concentration of the element in the sample probed region. The presence of peaks at energies then data indicates the presence of a specific component in the sample regarded. In addition, the intensity of the peaks is related to the concentration of the element in the sample probe area. The two main sources of radiation used in XPS are based on emissions of rays Kα magnesium (hν = 1253.6 eV) and aluminum (hν = 1486.6 eV). With these sources, kinetic energy KE of emitted photoelectrons will be in the interval 0-1250 eV or 0-1480 eV for magnesium and aluminum respectively. The inelastic mean free path of such electrons is particularly small in solids, which makes this particularly sensitive technical elements present in the sample surface [27].
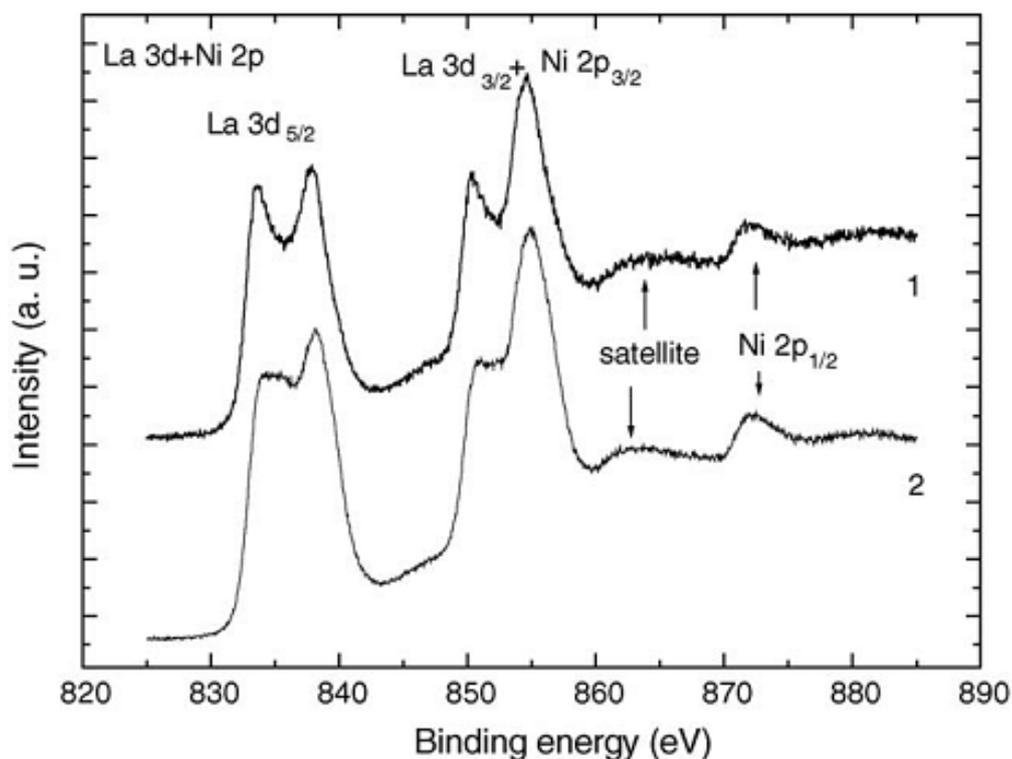
Figure II.19 *La 3d and Ni 2p core level spectra of the LaNiO$_{3-x}$ thin films taken at:*

(1) Normal emission and (2) grazing emission angles [28].

II.2.6.4 Apparatus used

X-ray photoelectron spectroscopy was performed with a VG Escalab 200 R spectrometer employing Al Kα (1486 eV) as x-ray source. (Institute of Catalysis and Petrochemical ICP-CSIC University Autonoma. Madrid).

Figure II.20 VG Escalab 200 R spectrometer.

II.2.7 Catalytic activity (CO oxidation)

II.2.7.1 Introduction

The oxidation of carbon monoxide is a very important reaction, and low temperature carbon monoxide oxidation reaction catalysts are important in many applications. Low temperature CO oxidation catalysts are used in residential and automotive air cleaning technologies, gas masks for mining applications, CO detectors, and selective oxidation of CO in reformer gas for fuel cell applications. Research interest in the catalytic oxidation of carbon monoxide has surged because of the possible uses for air cleaning, orbiting, closed-cycle CO_2 lasers,

and other remote sensing applications. Characteristic properties of a catalyst and pretreatment conditions have an effect on the catalytic activity of catalysts. Metal oxide catalysts are preferred for carbon monoxide oxidation reactions [29].

II.2.7.2 History

The first CO oxidation studies in the presence of perovskite back to the 50s by Parravano (1953). Later this oxidation reaction was described suprafacial reaction Voorhoeve et al. The suprafacial mechanism involves a reaction between species adsorbed on the catalyst surface. The solid surface present adequate atomic orbitals of symmetry and energy to activate the reactive molecules. Thus, the reaction rate depends on the degree of occupation of d orbitals (Fermi level).

A reaction mechanism on $LaCoO_3$ has been proposed by Tascon et al. (1981):

$$O_{2(g)} \rightarrow O_{2(ads)} \rightarrow 2.O_{(ads)}$$

$$CO_{(g)} \rightarrow CO_{(ads)}$$

$$CO_{(ads)} + 2.O_{(ads)} \rightarrow CO_{3(ads)} \quad (EDV)$$

$$CO_{3(ads)} \rightarrow CO_{2(ads)} + O_{(ads)}$$

$$CO_{2(ads)} \rightarrow CO_{2(g)}$$
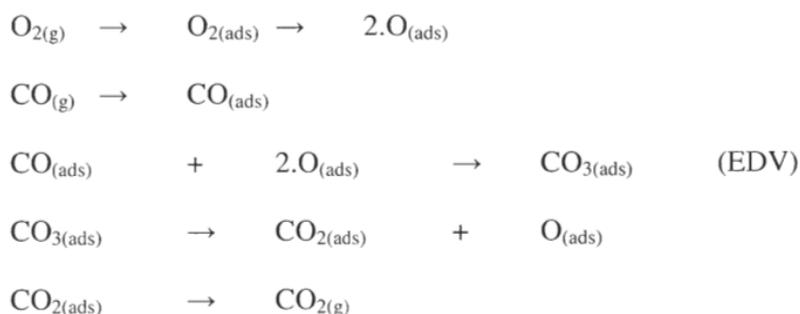
In this mechanism, the rate determining step (SDR) is the surface reaction between the adsorbed CO and adsorbed oxygen. Oxygen gas is adsorbed on the Co^{2+} ions surface and dissociates to form atomic oxygen (O^-). On the other hand CO is adsorbed at sites O^{2-} surface, leading to the formation of a labile species which reacts with atomic oxygen. This reaction produces a carbonate structure itself decomposed forming gaseous CO_2 [30].

II.2.7.3 Catalytic properties of $LaNiO_3$

$LaNiO_3$ with perovskite structure is considered of great interest because of its electronic and catalytic properties which make it a promising base material for its use as electrode material for storage and conversion of energy, as well as a

catalyst for the methane reforming reaction, for redox reactions involving NO, CO or soot [31–33] or for VOC's combustion reactions.

Rida. K et al studied the effect of calcination temperature on structural properties and catalytic activity in oxidation reactions of $LaNiO_3$ perovskite prepared by Pechini method. They found that, tests on the two catalytic oxidation reactions of C_3H_6 and CO over the system calcined between mentioned temperatures were examined on the basis of characterization results and showed that optimum catalytic properties for such reactions were achieved for the perovskite calcined at 600 °C [34].

II.2.7.4 Apparatus used

The catalysts were tested for the CO oxidation reaction at atmospheric pressure. 100 mg of powder sample was mixed homogeneously with SiC to obtain a total volume of ca. 1 ml. The mixture was then loaded in a cylindrical Pyrex reactor tube. The products of the reaction were analysed by infrared spectroscopy using a Perkin-Elmer 1725X FTIR spectrometer fitted with a multiple reflection transmission cell for gas analysis (Infrared Analysis). (Institute of Catalysis and Petrochemical ICP-CSIC University Autonoma. Madrid).

Figure II.21 different parts used in tests of catalytic activity for CO oxidation.

References

[1] Labhasetwar, N., Saravanan, G., Megarajan, S. K., Manwar, N., Khobragade, R., Doggali, P., & Grasset, F. (2016). Perovskite-type catalytic materials for environmental applications. Science and Technology of Advanced Materials.

[2] Ishihara, T. (Ed.). (2009). Perovskite oxide for solid oxide fuel cells. Springer Science & Business Media.

[3] Miquel, P. (2009). Réduction catalytique de NO_x par les hydrocarbures sur des catalyseurs à base de perovskite: application à la dépollution de moteurs Diesel (Doctoral dissertation, Lille 1).

[4] Pechini, M. P. (1967). US Pat. No. 3330697. US Pat. No. 3330697.

[5] Yarbay, R. Z., Figen, H. E., & Baykara, S. Z. (2012). Effects of Cobalt and Nickel Substitution on Physical Properties of Perovskite Type Oxides Prepared by the Sol-Gel Citrate Method. Acta Physica Polonica-Series A General Physics, 121(1), 44.

[6] Silva, G. R. O., Santos, J. C., Martinelli, D. M., Pedrosa, A. M. G., de Souza, M. J. B., & Melo, D. M. A. (2010). Synthesis and characterization of LaNixCo1-xO3 perovskites via complex precursor methods. Materials Sciences and Applications, 1(02), 39.

[7] Le, N. T. H., Calderón-Moreno, J. M., Popa, M., Crespo, D., & Phuc, N. X. (2006). LaNiO $_3$ nanopowder prepared by an 'amorphous citrate'route. Journal of the European Ceramic Society, 26(4), 403-407.

[8] Sierra Gallego, G., Batiot-Dupeyrat, C., & Mondragón, F. (2010). Methane partial oxidation by the lattice oxygen of the $LaNiO_3$-d perovskite. A pulse study. Dyna, 77(163), 141-150.

[9] Biswas, M. (2009). Synthesis of single phase rhombohedral LaNiO 3 at low temperature and its characterization. Journal of Alloys and Compounds, 480(2), 942-946.

[10] Soares, C. O., Carvalho, M. D., Jorge, M. E., Gomes, A., Silva, R. A., Rangel, C. M., & Pereira, M. I. (2011). Improving electrocatalytic activity of $LaNiO_3$ films by deposition on foam nickel substrates. Portugaliae Electrochimica Acta, 29(5), 335-342.

[11] Li, Y., Yao, S., Wen, W., Xue, L., & Yan, Y. (2010). Sol–gel combustion synthesis and visible-light-driven photocatalytic property of perovskite $LaNiO_3$.Journal of Alloys and Compounds, 491(1), 560-564.

[12] Gravereau, P. (2011). Introduction à la pratique de la diffraction des rayons X par les poudres (Doctoral dissertation, Sciences Chimiques).

[13] Scherrer, P. (1918). Nachrichten von der Gesellschaft der Wissenschaften zu Göttingen, Mathematisch-Physikalische Klasse.

[14] Patterson, A. L. (1939). The Scherrer formula for X-ray particle size determination. Physical review, 56(10), 978.

[15] Singh, A. K. (2005). Advanced x-ray techniques in research and industry. IOS Press.

[16] Stuart, B. (2004). Infrared spectroscopy: fundamentals and applications. JohnWiley & Sons, Ltd. ISBNs: 0-470-85427-8 (HB). 0-470-85428-6 (PB).

[17] Lavat, A. E., & Baran, E. J. (2003). IR-spectroscopic characterization of A 2 BB′ O 6 perovskites. Vibrational spectroscopy, 32(2), 167-174.

[18] Brown, M. E., Dollimore, D., & Galwey, A. K. (Eds.). (1980). Reactions in the solid state (Vol. 22). Elsevier.

[19] Moukhina, E. (2012). Determination of kinetic mechanisms for reactions measured with thermoanalytical instruments. Journal of thermal analysis and calorimetry, 109(3), 1203-1214.

[20] Wilburn, F. W. (1989). Introduction to thermal analysis, techniques and applications: Michael E. Brown, published by Chapman and Hall, London.

[21] Brunauer, S., Emmett, P. H., & Teller, E. (1938). Adsorption of gases in multimolecular layers. Journal of the American chemical society, 60(2), 309-319.

[22] Lawrence,S.G., (1981) ."Dispersion of Powders in Liquids", (Ed.), G.D. Parfitt, Third Edition, Ap-plied Science Publishers, London

[23] http://www.particlesciences.com/docs/technical_briefs/TB_2Final.pdf.

[24] http://www.malvern.com/en/products/technology/laser-diffraction/

[25] Engelhard, M. (2002). X-Ray Photoelectron Spectroscopy XPS. *EMSL*, 1-28.

[26] Venezia, A. M. (2003). X-ray photoelectron spectroscopy (XPS) for catalysts characterization. *Catalysis Today*, *77*(4), 359-370.

[27] Van der Heide, H., Hemmel, R., Van Bruggen, C. F., & Haas, C. (1980). X-ray photoelectron spectra of 3d transition metal pyrites. *Journal of Solid State Chemistry*, *33*(1), 17-25.

[28] Mickevičius, S., Grebinskij, S., Bondarenka, V., Vengalis, B., Šliužienė, K., Orlowski, B. A., Drube, W. (2006). Investigation of epitaxial LaNiO 3− x thin films by high-energy XPS. Journal of alloys and compounds, 423(1), 107-111.

[29] Balikçi, F., & Güldür, Ç. (2007). Characterization and CO Oxidation Activity Studies of Co-Based Catalysts. Turkish Journal of Chemistry, 31(5), 465-471.

[30] ASSEUR, B. L. (2009). Effet des cations A et B dans la structure pérovskite AB03 sur la catalyse de l'oxydation du méthanol.

[31] Norman AK, Morris MA (1999) The preparation of the single-phase perovskite $LaNiO_3$. Mater Proc Technol 92:91-96.

[32] Russo N, Fino D, Saracco G, Specchia V (2008) Promotion effect of Au on perovskite catalysts for the regeneration of diesel particulate filters. Catal Today 137(2):306-311.

[33] Rida K, Pena MA, Sastre E, and Martinez-Arias A (2012) Effect of calcination temperature on structural properties and catalytic activity in oxidation reactions of $LaNiO_3$ perovskite prepared by Pechini method. J of Rare Earths 30(3):210-216.

[34] Pecchi G, Reyes P, Zamora R, Cadús LE, Fierro JLG (2008) Surface properties and performance for VOCs combustion of $LaFe_{1-y}Ni_yO_3$ perovskite oxides. Solid State Chem 181(4):905-912.

Third chapter

Effect of the synthesis method, complexing agent and solvent on the physicochemical properties of LaNiO$_3$.

III.1 Introduction

A sol-gel (Pechini approach) and sol-gel combustion methods has been used to prepare different LaNiO$_3$ using different solvents and different agents of complexation [1].

The aim of this chapter, to study the physicochemical properties of the perovskite LaNiO$_3$, for that, the samples prepared by the method sol-gel and sol-gel combustion with Ethanol and distilled water as solvents and citric acid, ascorbic acid and sucrose as agents of complexation .the samples calcined at 800 °C were characterized by the X-ray diffraction (XRD, Fourier transform infrared (FTIR), thermal analysis (TGA) and powder size distribution (PSD) as a basis to explain their properties.

III.2 Preparation of the oxides LaNiO$_3$:

III .2.1 Preparation by sol-gel method

III .2.1.1 Using distilled water and ethanol as solvents

LaNiO$_3$ was prepared by the sol-gel method (Pechini approach) using citrate as complexing agent [1]. La (NO$_3$)$_3$.6H$_2$O (Sigma Aldrich), Ni (NO$_3$)$_3$.6H$_2$O (Sigma Aldrich), Ethanol (99%, from Fluka), distilled water (H$_2$O) and citric acid monohydrate C$_6$H$_8$O$_7$ (Sigma Aldrich) were used as reagents. Water and Methanol solutions of citric acid and of the metal nitrates were prepared separately and then mixed together and agitated for 5 h. The resulting solution was then concentrated by slowly evaporating the methanol at 80 C° until a gel was obtained. This gel was then dried in an oven slowly upon increasing the temperature to 100 °C and maintaining this temperature overnight in order to produce a solid amorphous citrate precursor. The resulting precursor was finally calcined in air at 800 °C for 5 h [2, 3]; such calcination temperature was selected on the basis of analysis of the decomposition of the precursor under air atmosphere.

```
┌─────────────────┐   ┌─────────────────┐   ┌─────────────────┐
│  La(NO₃).6H₂O   │   │   H₂O / Ethanol  │   │  Ni(NO₃)₃.6H₂O  │
└─────────────────┘   └─────────────────┘   └─────────────────┘
         │                     │                     │
         │                     ▼                     │
         │            ┌─────────────────┐            │
         └──────────▶ │     Mixture      │ ◀──────────┘
                      └─────────────────┘ ◀───┌─────────────────┐
                               │                │   C₆H₈O₇.H₂O    │
                               ▼                └─────────────────┘
                   ┌──────────────────────────┐
                   │  Heating the homogenous   │
                   │  solution at 80 C°, 5 hours│
                   └──────────────────────────┘
                               │
                               ▼
                   ┌──────────────────────────┐
                   │      Gel formation        │
                   └──────────────────────────┘
                               │
                               ▼
                   ┌──────────────────────────┐
                   │ Drying in an oven at 100 °C, 24 │
                   └──────────────────────────┘
                               │
                               ▼
                   ┌──────────────────────────┐
                   │       Fine Powder         │
                   └──────────────────────────┘
                               │
                               ▼
                   ┌──────────────────────────┐
                   │ Calcination in air at 800 C° for 5 h │
                   └──────────────────────────┘
```

Figure III.1: The different steps of sol-gel synthesis (water-Ethanol –citric acid).

Montage used

Solutions before mixing

Fine Powder S1

After calcination

Fine Powder S2

III .2.1.2 Using citric acid, ascorbic acid and sucrose as agents of complexation

LaNiO$_3$ was prepared by the sol-gel method (Pechini approach) using citrate as complexing agent [1]. La (NO$_3$)$_3$.6H$_2$O (Sigma Aldrich), Ni (NO$_3$)$_3$.6H$_2$O (Sigma Aldrich), distilled water (H$_2$O) and citric acid monohydrate C$_6$H$_8$O$_7$ (Sigma Aldrich), ascorbic acid C$_6$H$_8$O$_6$ (Fluka) and sucrose C$_{12}$H$_{22}$O$_{11}$ (Fluka) were used as reagents. Water solutions of complexing agent and of the metal nitrates were prepared separately and then mixed together and agitated for 5 h. The resulting solution was then concentrated by slowly evaporating the methanol at 80 C° until a gel was obtained. This gel was then dried in an oven slowly upon increasing the temperature to 100 °C and maintaining this temperature overnight in order to produce a solid amorphous citrate precursor. The resulting precursor was finally calcined in air at 800 °C for 5 h [2, 3]; such calcination temperature was selected on the basis of analysis of the decomposition of the precursor under air atmosphere.

Samples after Drying in an oven at 100 °C, 24h

| **S1** | **S4** | **S3** |

Samples after Calcination in air at 800 C° for 5 h

Citric acid $C_6H_8O_7.H_2O$

Ascorbic acid $C_6H_8O_6$

Sucrose $C_{12}H_{22}O_{11}$

$La(NO_3).6H_2O$

$Ni(NO_3)_3.6H_2O$

Mixture

H_2O

Heating the homogenous solution at 80 C°, 5 hours

Gel formation

Drying in an oven at 100 °C, 24 h

Fine Powder

Calcination in air at 800 C° for 5 h
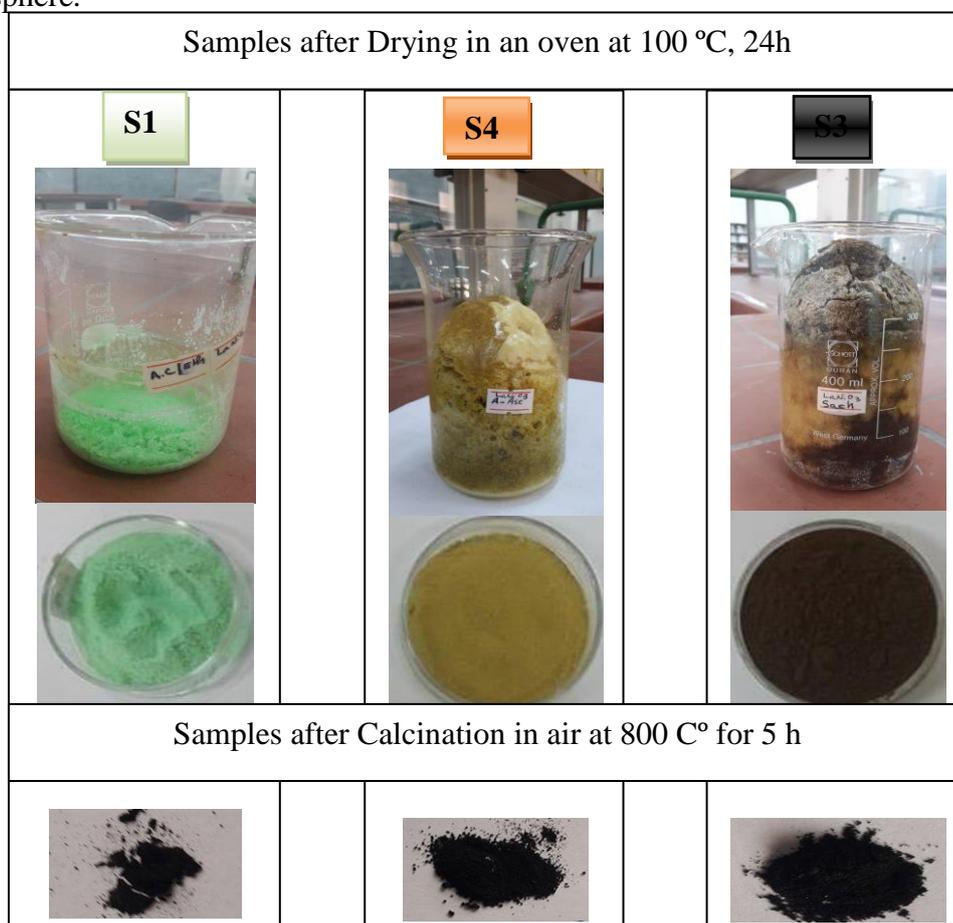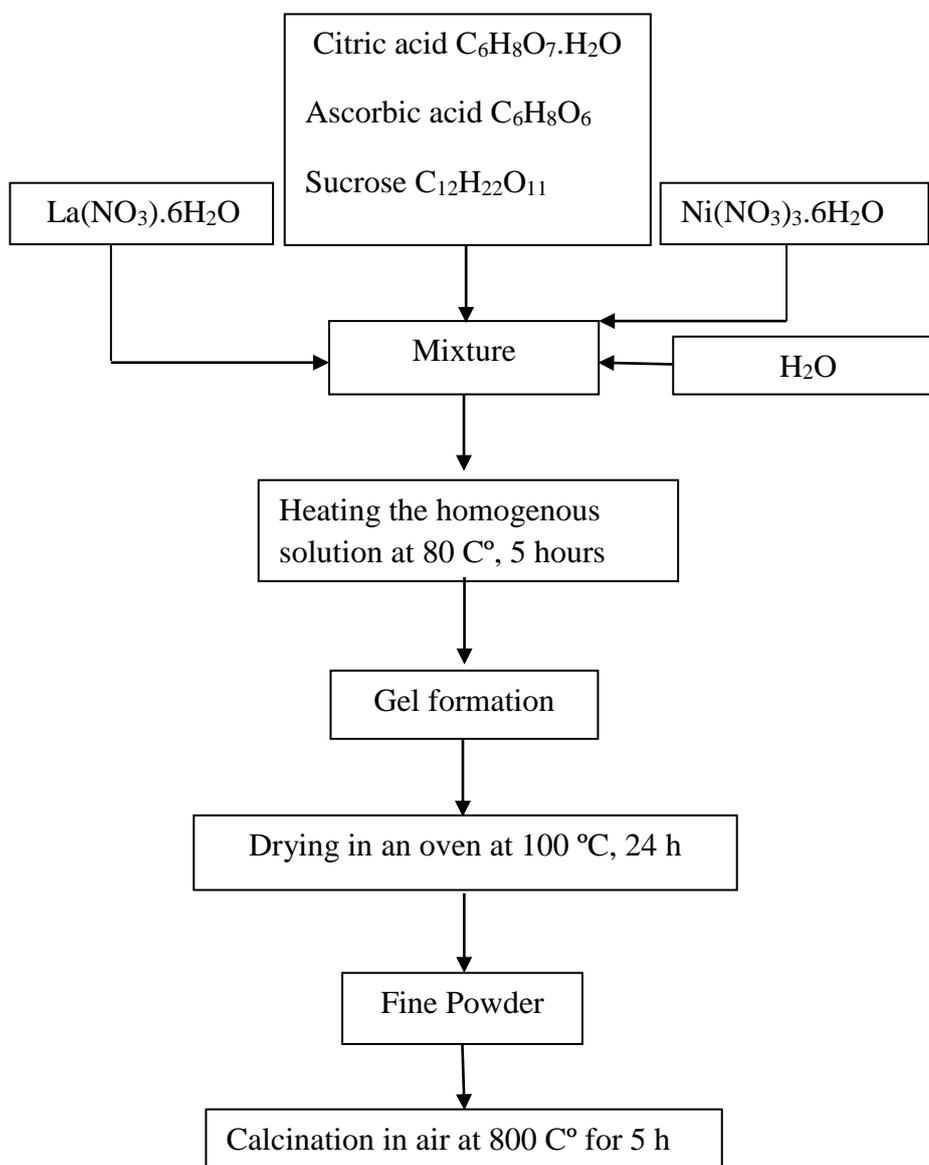
Figure III.2: The different steps of sol-gel synthesis (citric acid, ascorbic acid and sucrose as agents of complexation)

.

III .2.1 Preparation by sol-gel combustion

LaNiO$_3$ was prepared by the sol-gel combustion method using citrate as complexing agent [1]. La (NO$_3$)$_3$.6H$_2$O (Sigma Aldrich), Ni (NO$_3$)$_3$.6H$_2$O (Sigma Aldrich), distilled water (H$_2$O) and citric acid monohydrate C$_6$H$_8$O$_7$ (Sigma Aldrich) were used as reagents. Water solutions of citric acid and of the metal nitrates were prepared separately and then mixed together and agitated for 1 h. The resulting solution was then concentrated by slowly evaporating the methanol at 80 C° until a gel was obtained. This gel was then heated at 250 ºC, we looked a rise in very sharp temperature, a combustion of all precursors, then cooling to room temperature. The resulting precursor was finally calcined in air at 800 ºC for 5 h [2, 3]; such calcination temperature was selected on the basis of analysis of the decomposition of the precursor under air atmosphere.

Sample S5 after combustion of all precursors at 250 ºC

Sample S5 after Calcination

```
┌──────────────────┐   ┌──────────┐   ┌──────────────────┐
│  La(NO₃).6H₂O    │   │   H₂O    │   │  Ni(NO₃)₃.6H₂O   │
└──────────────────┘   └──────────┘   └──────────────────┘
            │                │                 │
            │                ▼                 │
            │          ┌──────────┐            │
            └─────────▶│ Mixture  │◀───────────┘
                       └──────────┘◀───┌──────────────────┐
                            │          │   C₆H₈O₇.H₂O     │
                            ▼          └──────────────────┘
```

$La(NO_3).6H_2O$ H_2O $Ni(NO_3)_3.6H_2O$

Mixture

$C_6H_8O_7.H_2O$

Heating the homogenous solution at 80 C°, 5 hours

Gel formation

Heating at 250 °C

Combustion of all precursors

Cooling to room temperature (Fine Powder)

Calcination in air at 800 C° for 5 h
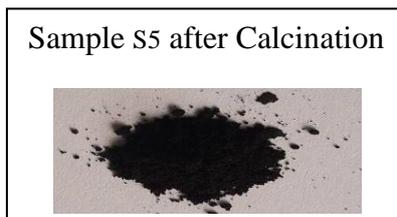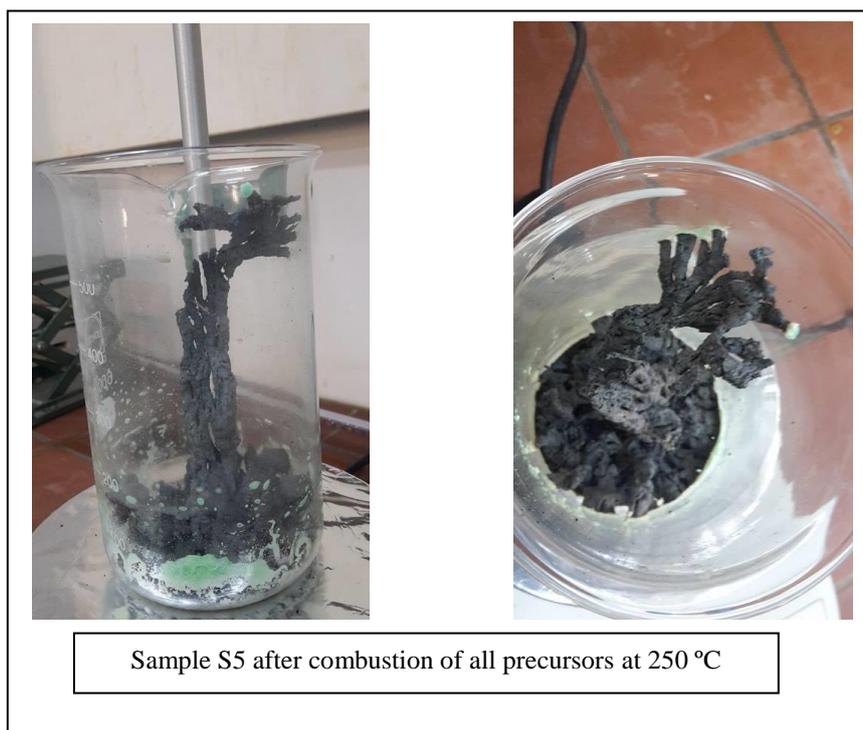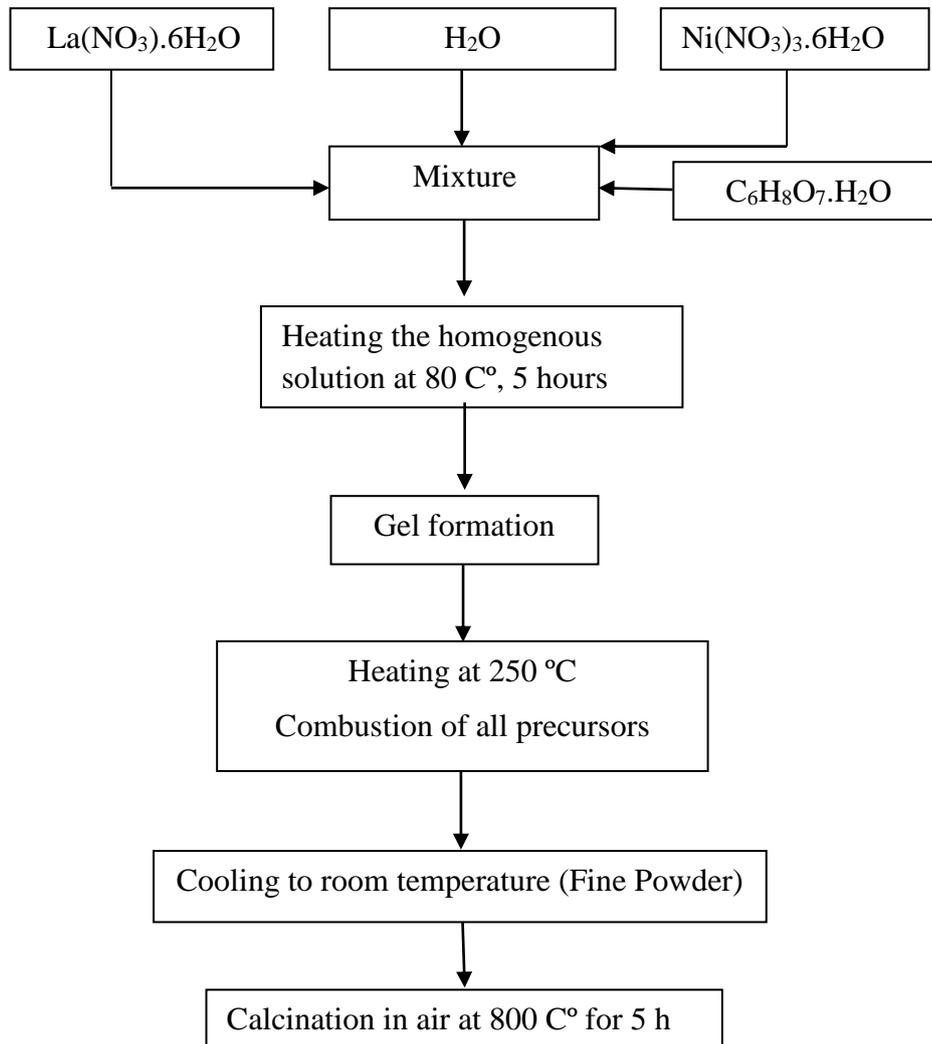
Figure III.3: The different steps of sol-gel combustion synthesis.

III .3 Characterization of Samples:

III .3.1 X-ray diffraction

XRD Patterns were collected on a Bruker AXS D8- advance diffractometer employing Cu Kα radiation. In all diffractograms, a step size of 0.02 o (2θ) was used with a data collection time of 15s. Data were collected between 2θ values of geometry. Identification of crystalline phases was carried out θ10° and 80° using standard θ/2 by comparison with JCPDS standards. The unit cell parameters were obtained by fitting the peak position of the XRD pattern using the Match and X'pert Highscore programs. The result obtained for the compounds under study is shown in the following figures:
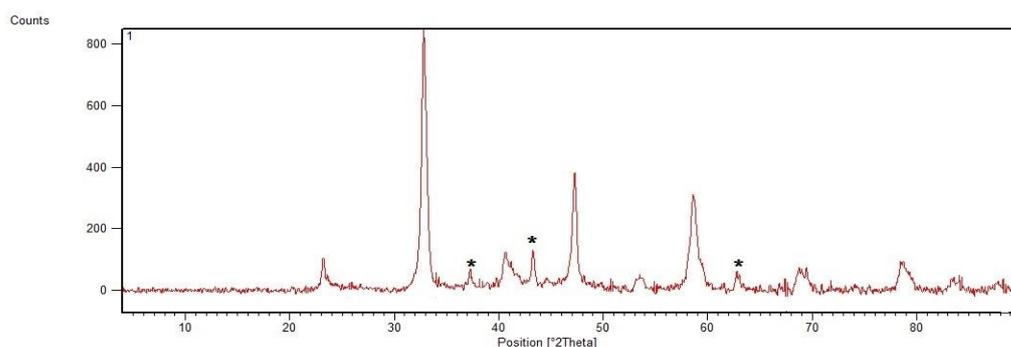
Figure III .4 XRD patterns of LaNiO₃ prepared by sol-gel
*(Water - citric acid S1) Peaks marked with * correspond to NiO.*
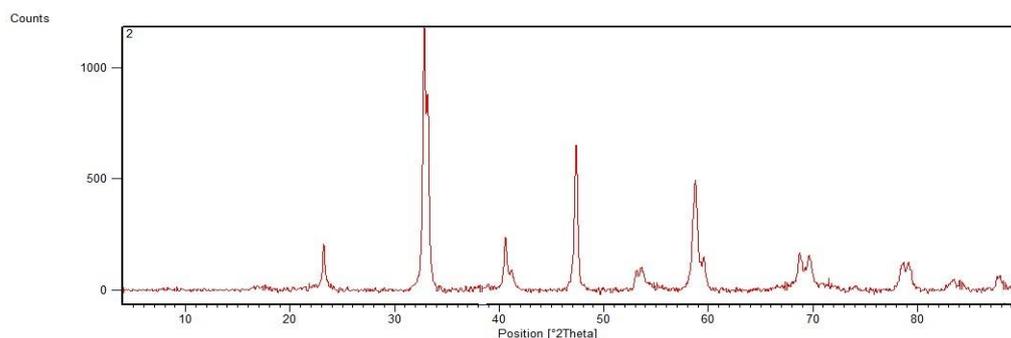
Figure III .5 XRD patterns of LaNiO₃ prepared by sol-gel
(Ethanol - citric acid S2)
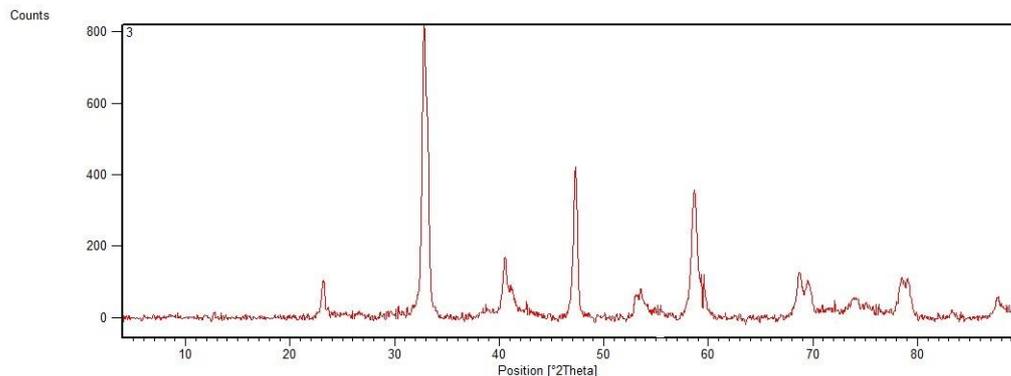
Figure III .6 *XRD patterns of LaNiO₃ prepared by sol-gel*

(Sucrose – water S3)
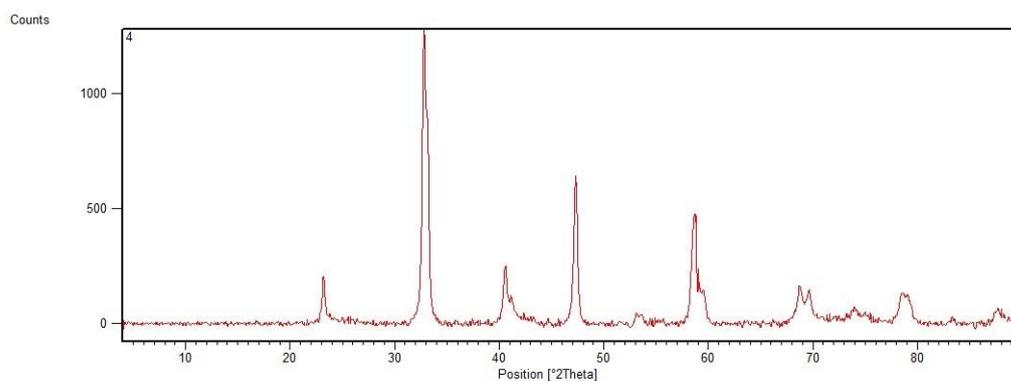
Figure III .7 *XRD patterns of LaNiO₃ prepared by sol-gel*

(Ascorbic acid – water S4)

The observed values of the 2θ with JCPDS standards for this type of compound (X'pert highscore software) it shows us the presence of a single phase which is the perovskite LaNiO₃ (S1, S2, S3, S4) Perovskite-type phase with rhombohedral symmetry, space group R3m [4, 5, 6], Additional peaks are shown in the diffractogram of the sample S1 (LaNiO₃ prepared by water and citric acid), the most intense ones appearing at 2θ~ 37.2, 43.3 and 62.80 which correspond to cubic NiO [4, 7]

- JCPDS standard of LaNiO$_3$. (Reference code 00-033-0711)

Date: 20/03/2016 Time: 18:23:53   File: 00-001-1239   User: microtel

Name and formula

Reference code: 00-033-0711

PDF index name: Lanthanum Nickel Oxide

Empirical formula: LaNiO$_3$
Chemical formula: LaNiO$_3$

Crystallographic parameters

Crystal system: Rhombohedral
Space group: R-3m
Space group number: 166

a (Å):   5,4570
b (Å):   5,4570
c (Å):   6,5720
Alpha (°):   90,0000
Beta (°):   90,0000
Gamma (°):   120,0000

Calculated density (g/cm^3):   7,22
Volume of cell (10^6 pm^3):   169,49
Z: 3,00

RIR: -

Subfiles and Quality

Subfiles: Inorganic
       Corrosion
Quality: Indexed (I)

Comments

General comments: Increase of temperature causes a decrease of the rhombohedral
       Room temperature form.
       distortion leading to cubic cell parameters at about 1020 C.
       Form II.
       Above 825 C, LaNiO$_3$ slowly decomposes into NiO and an "unidentified phase" of
       LaNiO$_2$ (PDF 00-012-0751), which changes irreversibly into La$_2$NiO$_4$ at 1166 C.
       The doubling of the c-axis could not be confirmed by
       superstructure reflections in this powder pattern.
Sample preparation: Sample was spray-dried from aqueous solution and annealed at 1000 C in an oxygen
       flow.
Additional pattern: To replace 00-010-0341.
Unit cell: Rhombohedral cell data: a=3.8375, a=90.44.
       Space group R-3c and doubling of the c-axis has been reported by Megaw and
       Darlington [Acta Crystallogr., Sec. A, 31 161 (1975)] for related compounds.

References

Primary reference: Wustenberg, H., Hahn, Inst. fur Kristallogr., Technische Hochschule, Aachen,
       Germany., ICDD Grant-in-Aid, (1981)

Date: 20/03/2016 Time: 18:23:53 File: 00-001-1239 User: microtel

Peak list

No.	h	k	l	d [A]	2Theta[deg]	I [%]
1	1	0	1	3,84000	23,144	35,0
2	1	1	0	2,73200	32,754	100,0
3	0	1	2	2,70100	33,140	85,0
4	0	2	1	2,22300	40,548	25,0
5	0	0	3	2,18900	41,207	11,0
6	2	0	2	1,92000	47,306	70,0
7	2	1	1	1,72400	53,078	8,0
8	1	1	3	1,70800	53,615	7,0
9	3	0	0	1,57650	58,499	25,0
10	1	2	2	1,57020	58,757	35,0
11	1	0	4	1,55150	59,536	16,0
12	2	2	0	1,36400	68,768	14,0
13	0	2	4	1,34840	69,678	12,0
14	1	3	1	1,28490	73,668	2,0
15	3	0	3	1,27860	74,092	6,0
16	3	1	2	1,21780	78,475	15,0
17	2	1	4	1,20900	79,157	15,0
18	2	2	3	1,15770	83,422	7,0
19	2	0	5	1,14870	84,224	5,0
20	0	4	2	1,11200	87,691	9,0
21	3	2	1	1,06940	92,160	3,0
22	1	2	5	1,05850	93,393	5,0
23	4	1	0	1,03070	96,724	4,0
24	1	3	4	1,02480	97,469	17,0
25	1	1	6	1,01680	98,501	14,0

Stick Pattern
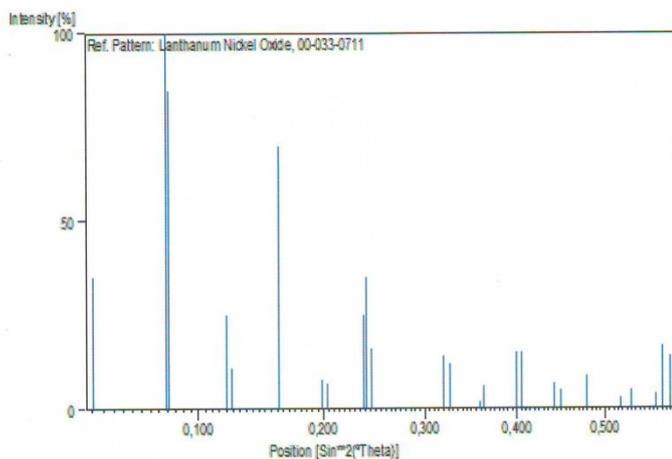
- JCPDS standard of NiO. (Reference code 00-047-1049)

Date: 20/03/2016 Time: 18:31:19   File: 00-001-1239   User: microtel

Name and formula

Reference code: 00-047-1049

Mineral name: Bunsenite, syn
PDF index name: Nickel Oxide

Empirical formula: NiO
Chemical formula: NiO

Crystallographic parameters

Crystal system: Cubic
Space group: Fm-3m
Space group number: 225

a (Å):   4,1771
b (Å):   4,1771
c (Å):   4,1771
Alpha (°):   90,0000
Beta (°):   90,0000
Gamma (°):   90,0000

Calculated density (g/cm^3):   6,81
Volume of cell (10^6 pm^3):   72,88
Z: 4,00

RIR: 6,15

Subfiles and Quality

Subfiles: Inorganic
                         Mineral
                         Alloy, metal or intermetalic
                         Corrosion
                         Common Phase
                         Forensic
Quality: Star (S)

Comments

Color: Green
General comments: Average relative standard deviation in intensity of the 5 strongest reflections for 3
                         specimen mounts = 1.1%.
                         Validated by calculated pattern.
Sample source: Sample obtained from J.T. Baker Chemical Corporation.
Sample preparation: Sample annealed for 72 hours at 1100 C.
Optical data: B=2.27
Additional pattern: To replace 00-004-0835.

References

Primary reference: Martin, K., McCarthy, G., North Dakota State Univ., Fargo, ND, USA., *ICDD Grant-in-Aid*, (1991)
Optical data: Winchell, Winchell., *Elements of Optical Mineralogy*, 58, (1964)

1 Of 2

Date: 20/03/2016 Time: 18:31:19 File: 00-001-1239 User: microtel

Peak list

No.	h	k	l	d [A]	2Theta[deg]	I [%]
1	1	1	1	2,41200	37,249	61,0
2	2	0	0	2,08900	43,276	100,0
3	2	2	0	1,47680	62,879	35,0
4	3	1	1	1,25940	75,416	13,0
5	2	2	2	1,20580	79,409	8,0
6	4	0	0	1,04430	95,059	4,0
7	3	3	1	0,95830	106,993	3,0
8	4	2	0	0,93400	111,123	7,0

Stick Pattern

Ref. Pattern: Bunsenite, syn, 00-047-1049
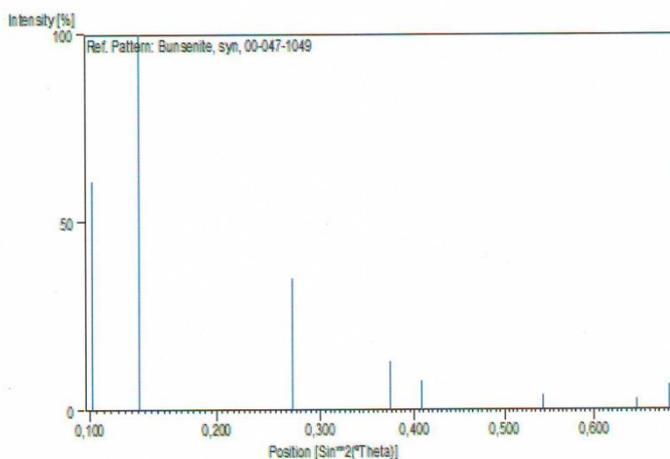
XRD patterns of $LaNiO_3$ prepared by sol-gel the combustion using water and citric acid, before and after calcination are shown in the following figures:
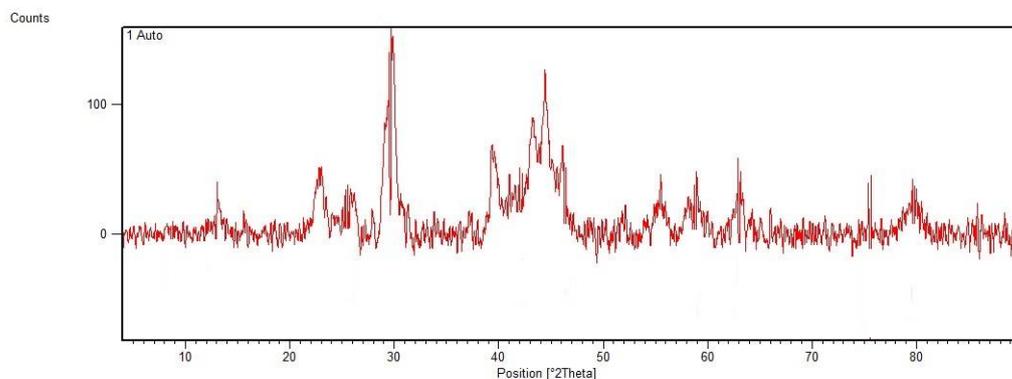
Figure III .8 *XRD patterns of $LaNiO_3$ prepared by sol-gel combustion (Citric acid – water S5) before calcination.*
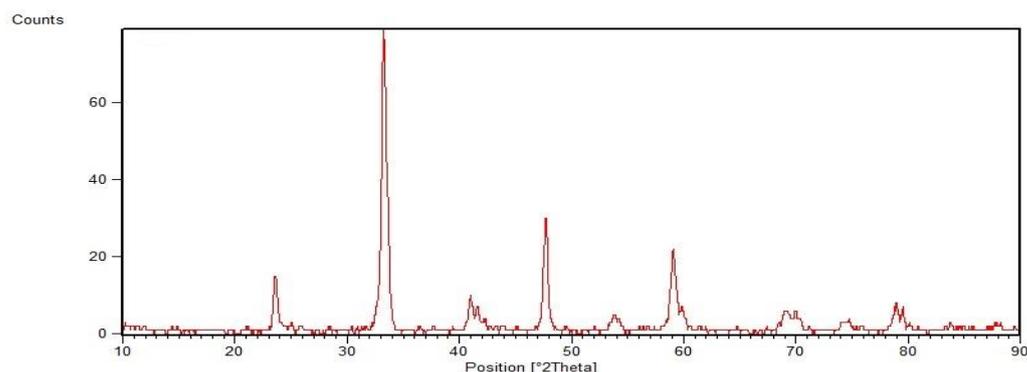
Figure III .9 *XRD patterns of $LaNiO_3$ prepared by sol-gel combustion (Citric acid – water S5) after calcinations.*

The sample S5 $LaNiO_3$ prepared by sol-gel combustion need a calcination at 800 °C for 5 hours with a rate of 5 °C.min^{-1} to form the perovskite phase of rhombohedral symmetry and space group of R3m.

The observed values of the 2θ with JCPDS standards for this type of compound (X'pert highscore software) it shows us the presence of a single phase which is the perovskite $LaNiO_3$ [8, 9].

III .3.2 Infrared spectroscopy

Infrared transmission spectra were performed on a Fourier transform spectrometer (FTIR) Shimadzu 8400S. A granular technique employing KBr (1 mg of sample added to 200 mg of KBr) was used and the spectra were recorded in the 400-4000 cm^{-1} range. The infrared spectra of the 5 samples (S1, S2, S3, S4 and S5) before calcination are shown in the following figures:
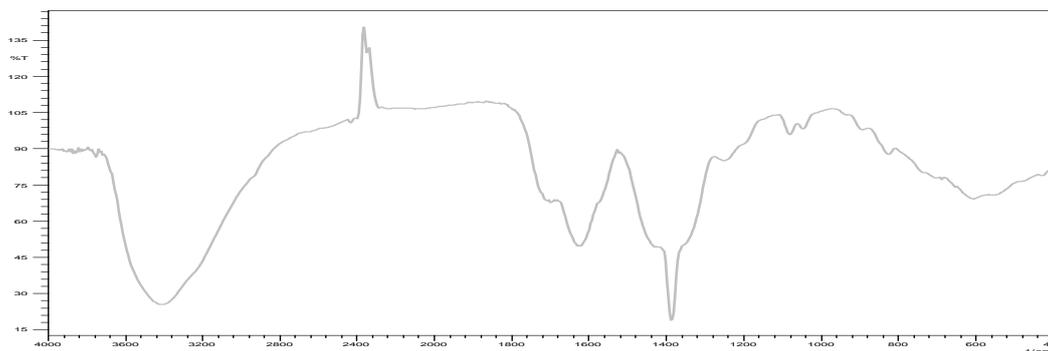
Figure III .10 *Infrared spectrum of LaNiO₃ prepared by sol-gel*
(water - citric acid S1) before calcination.
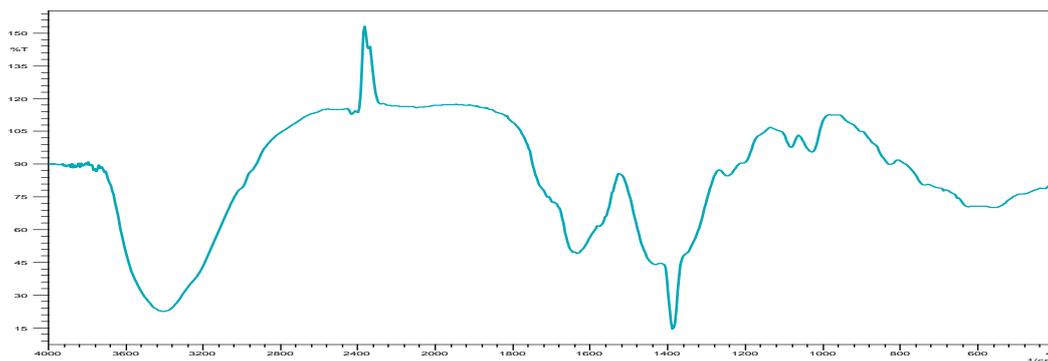
Figure III .11 *Infrared spectrum of LaNiO₃ prepared by sol-gel*
(Ethanol - citric acid S2) before calcination.
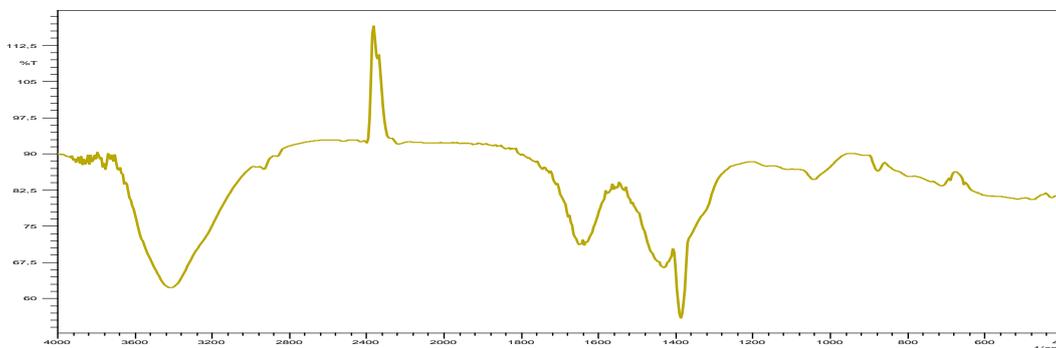
Figure III .12 *Infrared spectrum of LaNiO₃ prepared by sol-gel*

(Sucrose – water S3) before calcination.
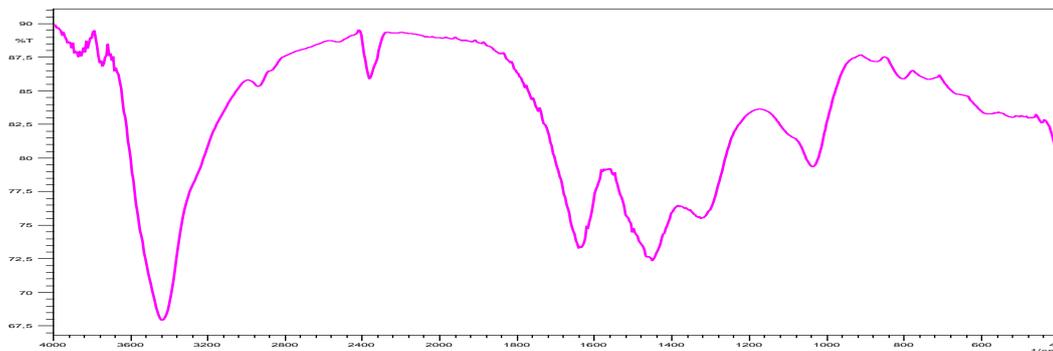
Figure III .13 *Infrared spectrum of LaNiO₃ prepared by sol-gel*

(Ascorbic acid – water S4) before calcination.
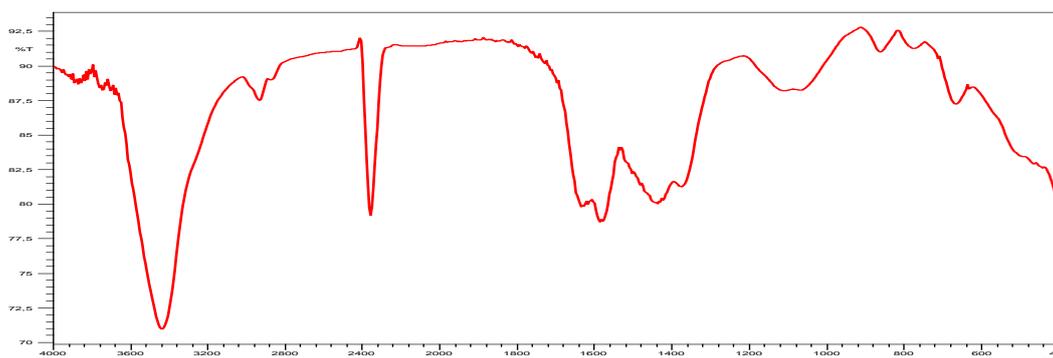
Figure III .14 *Infrared spectrum of LaNiO₃ prepared by sol-gel combustion*

(Citric acid – water S5) before calcination.

Infrared spectra obtained for these samples prepared by different complexing agent exhibit a wide absorption band, the characteristic is: 3450 cm^{-1}. The wide band appear obvious to about 3450 cm^{-1} attributed to the stretching vibration of hydroxide (OH) of the solvent (water or Ethanol) absorbed by the molecules [10] Or attributed to (OH) of complexation agents (acid citric, ascorbic acid and sucrose). The infrared spectrum of the sample S4 shows an intense band at about 1705 cm^{-1} which characterizes the carboxyl (C=O) ascorbic acid. While this band is less intense in the spectra of samples S1, S2 and S5 when we used citric acid as a complexation agent. There is also an intense band at 1330-1410 cm-1 and about 1280 to 1380 cm-1 characteristic vibration of deformation in the plane of each of alcohol and carboxylic acids [11, 12].
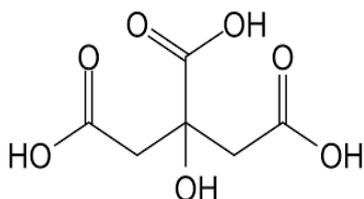
Citric acid C$_6$H$_8$O$_7$
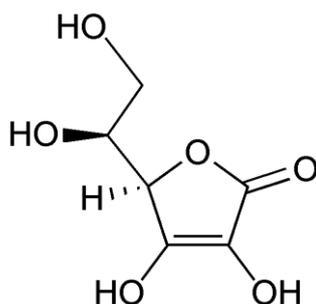
Ascorbic acid C$_6$H$_8$O$_6$
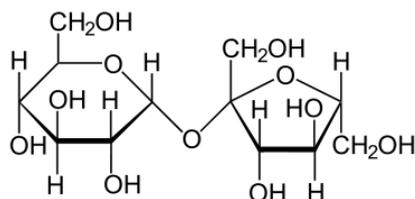
Sucrose C$_{12}$H$_{22}$O$_{11}$

Infrared spectra of samples prepared by various agents of complexation and different methods of synthesis after calcination are shown in the following figures:
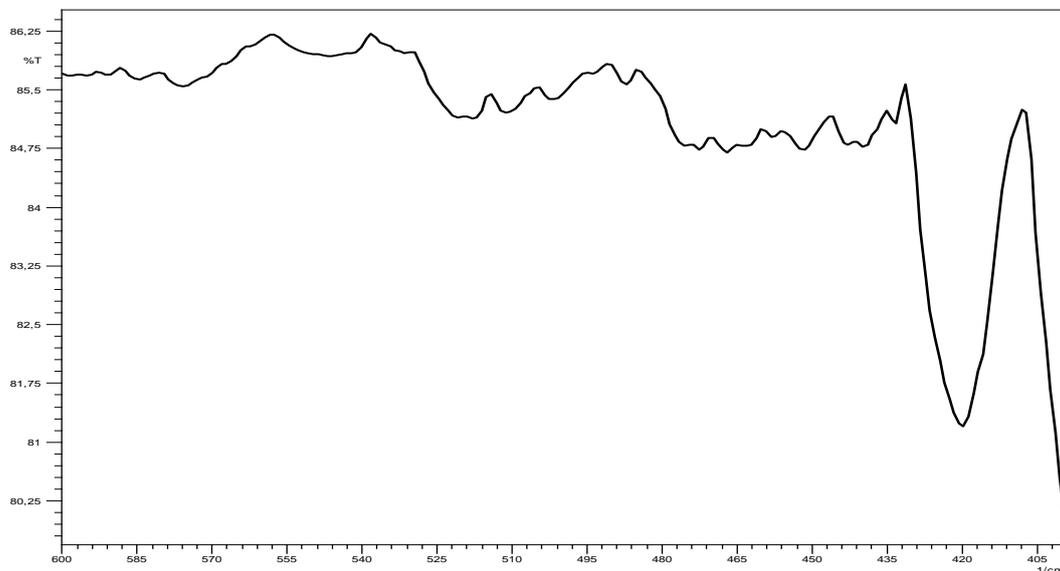
Figure III .15 *Infrared spectrum (400-600 cm^{-1}) of LaNiO$_3$ prepared by sol-gel (Water - citric acid S1) after calcination.*
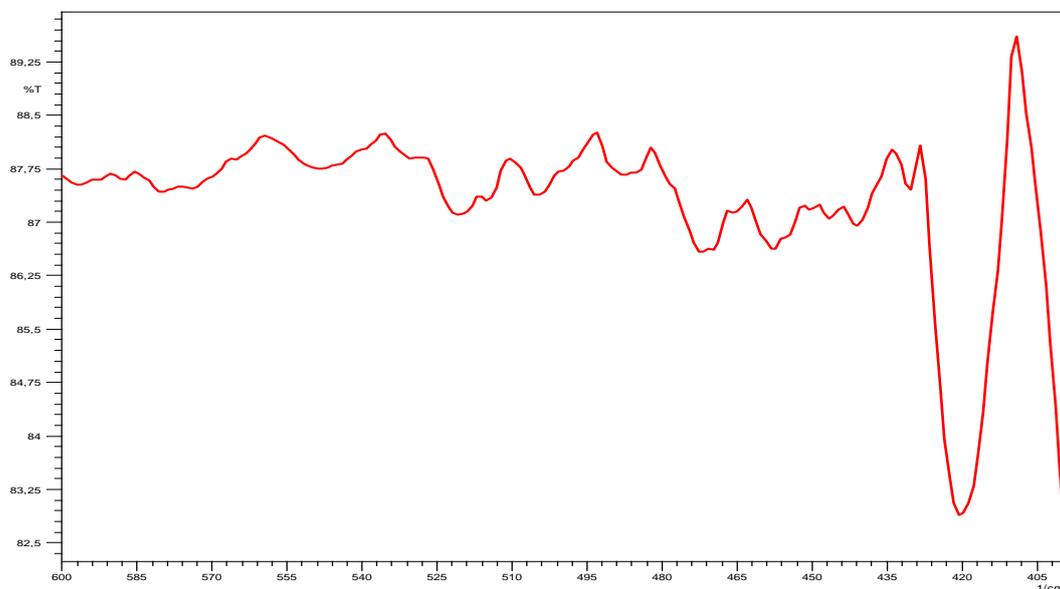
Figure III .16 *Infrared spectrum (400-600 cm^{-1}) of LaNiO$_3$ prepared by sol-gel (Ethanol - citric acid S2) after calcination.*
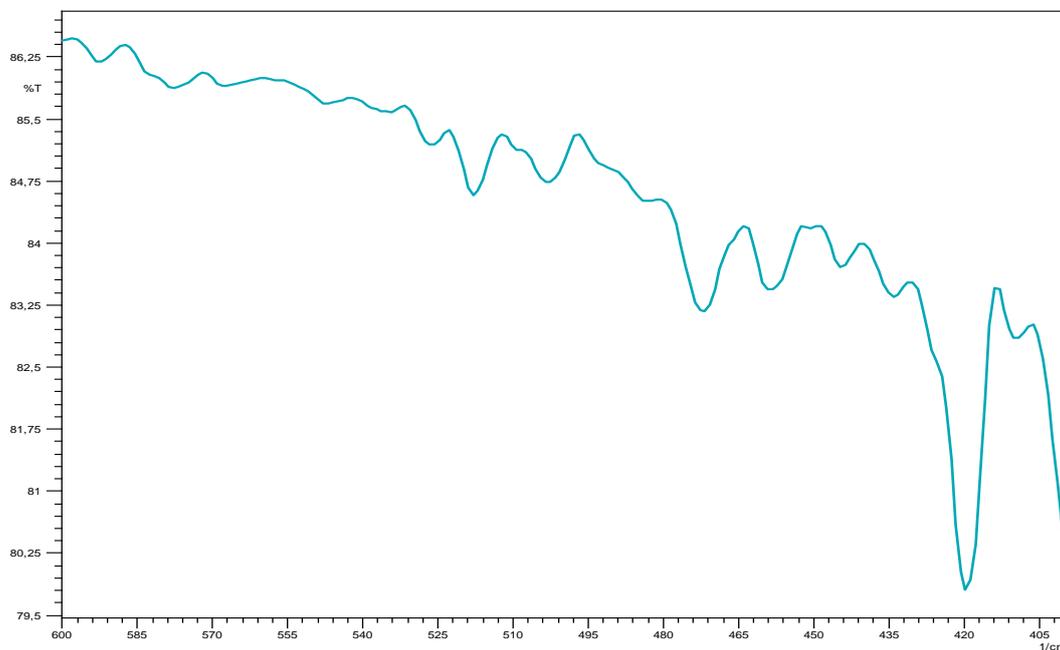
Figure III .17 *Infrared spectrum (400-600 cm^{-1}) of LaNiO$_3$ prepared by sol-gel*

(Sucrose – water S3) after calcination.
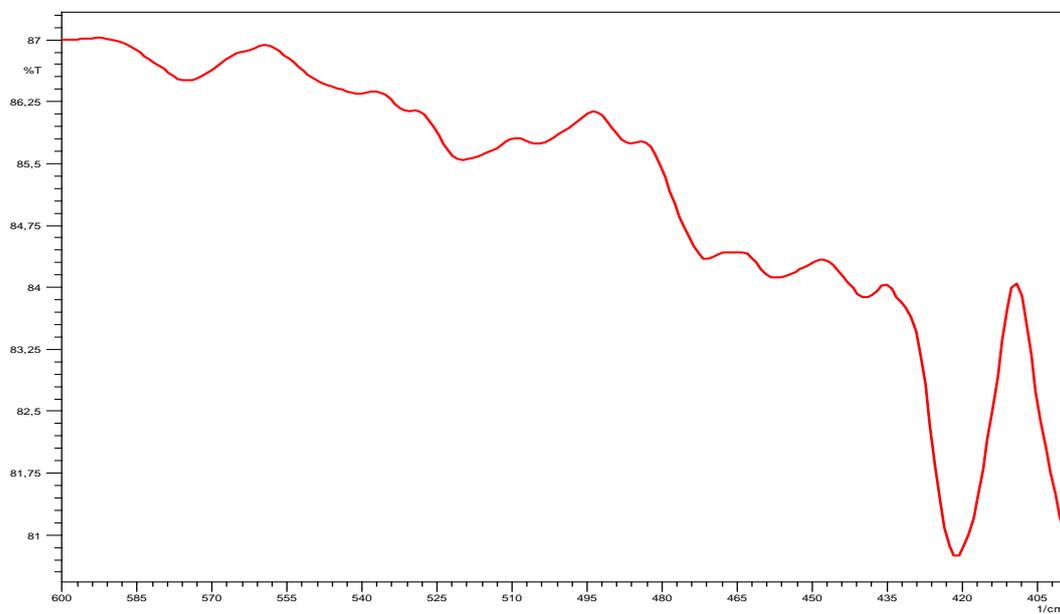
Figure III .18 *Infrared spectrum (400-600 cm^{-1}) of LaNiO$_3$ prepared by sol-gel*

(Ascorbic acid – water S4) after calcination.
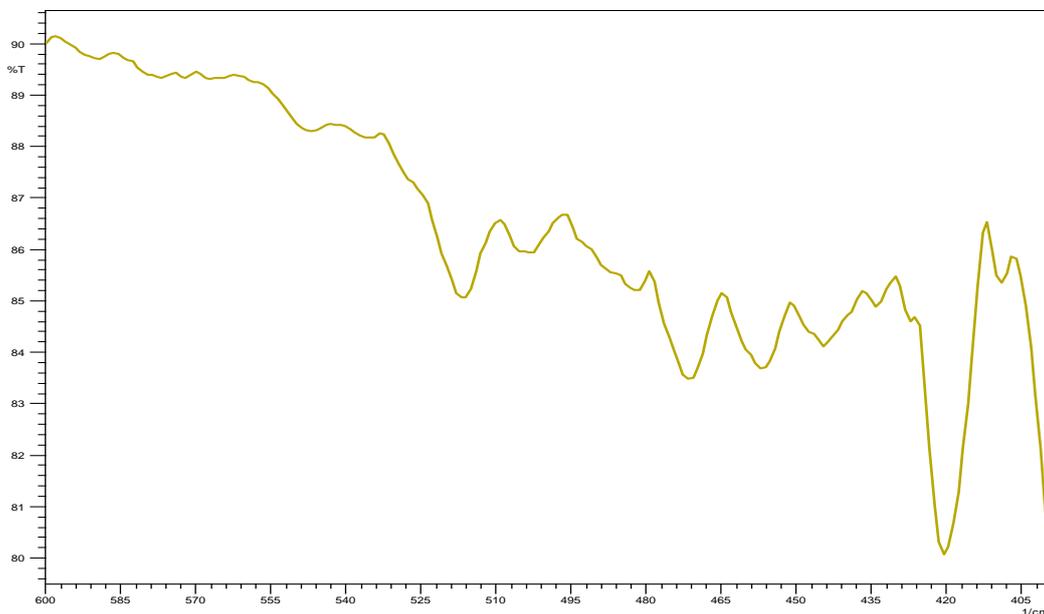
Figure III .19 *Infrared spectrum (400-600 cm^{-1}) of LaNiO$_3$ prepared by sol-gel combustion (Citric acid – water S5) after calcination.*

The infrared spectra of these five samples after calcination at 800 °C show strong and well-defined absorption bands, typical of perovskite oxides [13]; Typically, the vibrations the M-O (M = Ni) vibrations of octahedral MO$_6$ units dominate the spectra. The infrared spectra show a value of absorption band about 420 cm^{-1} attributed to vibrations of the Ni-O bond in the perovskite LaNiO$_3$ compared the infrared spectra before calcinations [14].

III .3.3 Thermal characterizations (TGA) of precursors

Thermogravimetric analyze (TGA) of the precursor decomposition were performed on a Perkin-Elmer TGA7 device, respectively, from 20 to 900 ℃ at a heating rate of 10 ℃ min^{-1}.

The precursors (after the drying step of the preparation at 100 C°) were examined by TGA in order to explore their decomposition under atmospheric air and with the aim of establishing most adequate calcination conditions for them. The results are displayed in the following figures:
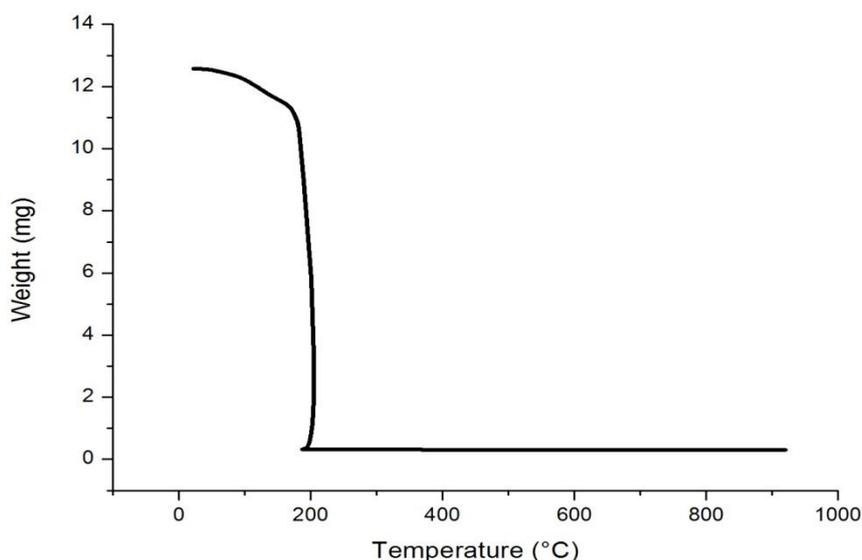
Figure III .20 TGA curve during heating of LaNiO$_3$ powder prepared by sol-gel (water - citric acid S1).

Figure (III .18) shows the TGA plot of the gel (S1), TGA shows two decomposition processes:

- Weight loss of 95% between 25-190 °C indicates the desorption of adsorbed or hydration water that may remain in the precursors and the sudden charring of citric acid polymer [8, 15, 16].
- Weight loss of 1% between 190-250 °C corresponds the slow combustion of carbon and the oxidative decomposition of citrates complexing the

metals in the precursors and complete removal of organic matters took place at the temperature below 250 °C [17, 18].
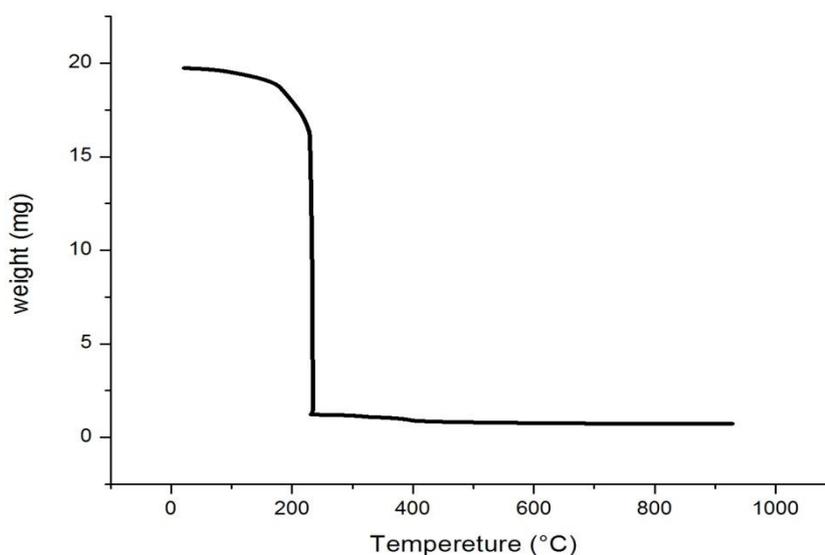
Figure III .21 *TGA curve during heating of LaNiO₃ powder prepared by sol-gel*
(Ethanol - citric acid S2).

Figure (III .19) shows the TGA plot of the gel (S2), TGA shows three decomposition processes:

- Weight loss of 92% between 25-220 °C indicates the desorption of adsorbed or hydration water that may remain in the precursors and the sudden charring of citric acid polymer [8, 15, 16].

- Weight loss of 2% between 220-400 °C corresponds the slow combustion of carbon and the oxidative decomposition of citrates complexing the metals in the precursors [17, 19].

- Weight loss of 1% up to 400 °C, indicates complete removal of organic matters took place at the temperature below 400 °C [18].
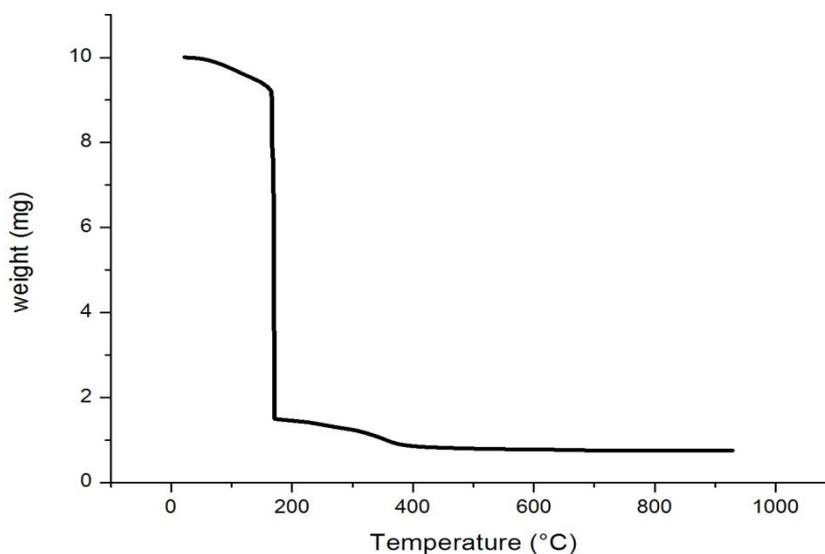
Figure III .22 *TGA curve during heating of LaNiO₃ powder prepared by sol-gel*
(Sucrose – water S3).

Figure (III .20) shows the TGA plot of the gel (S3), TGA shows three decomposition processes:

- Weight loss of 85% between 25-180 °C indicates the desorption of adsorbed or hydration water that may remain in the precursors and the sudden charring of sucrose polymer [8, 15, 16].

- Weight loss of 5% between 180-350 °C corresponds the slow combustion of carbon and the oxidative decomposition of complexing the metals in the precursors [17, 19].

- Weight loss of 30 % between 350-500 °C indicates complete removal of organic matters took place at the temperature below 400 °C [18].
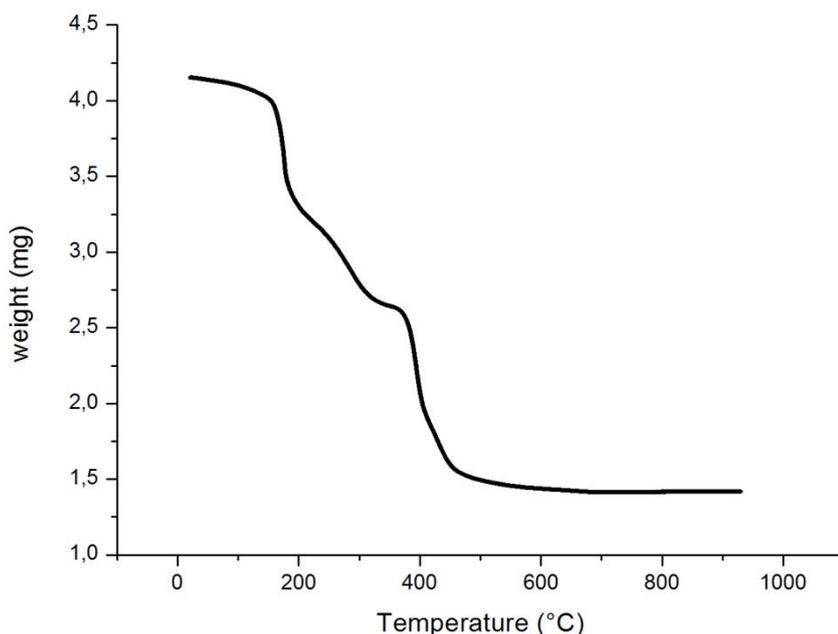
Figure III .23 *TGA curve during heating of LaNiO₃ powder prepared by sol-gel*
(Ascorbic acid – water S4).

Figure (III .21) shows the TGA plot of the gel (S4), TGA shows three decomposition processes:

- Weight loss of 5% between 25-180 °C indicates the desorption of adsorbed or hydration water that may remain in the precursors and the sudden charring of Ascorbic acid polymer.

- Weight loss of 30% between 180-350 °C corresponds the slow combustion of carbon and the oxidative decomposition of complexing the metals in the precursors [17, 19].

- Weight loss of 30% between 180-350 °Ccorresponds to the decomposition of carbonate or carboxylate-type complexes remaining in the sample [18].

III .3.4 Powder size distribution (PSD)

The analysis of the distribution of the grain size of the samples was employed in order to show the influence of the complexing agent, solvents and the synthetic methods employed on the particle size by laser granulometry. After calcination at 800 °C the powder was dispersed in deionized water in a beaker with magnetic stirring and combined under ultrasound for 15 minutes. Powder size distribution was characterized with a laser particle size analyzer (Mastersizer 2000, Malvern) [20]. The results are displayed in the following figures:
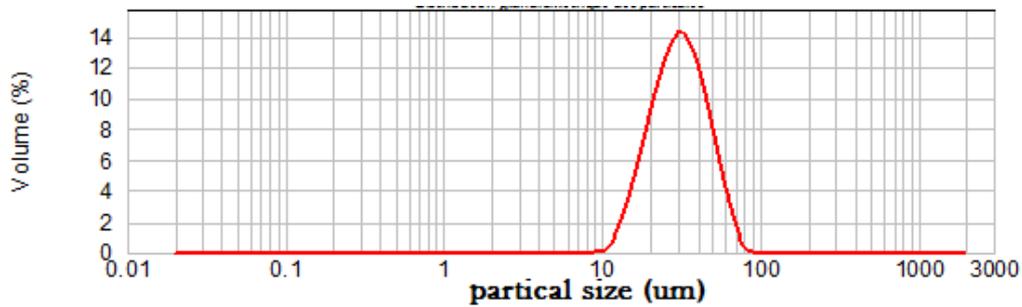
Figure III .24 Particle size distribution of LaNiO₃ prepared by sol-gel (water - citric acid S1) after calcination.

One mode of particle distribution of the sample S1 are shown, which the peak is centered at 30 microns of the volume distribution is 15%.
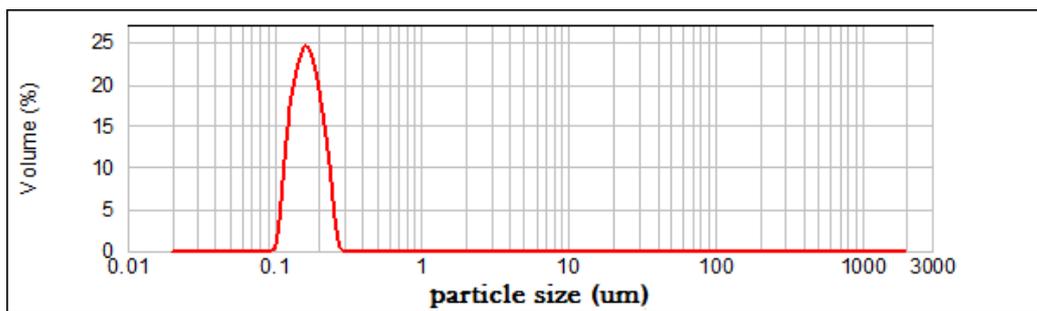
Figure III .25 Particle size distribution of LaNiO₃ prepared by sol-gel (Ethanol - citric acid S2) after calcination.

One mode of particle distribution of the samples S2 is shown, which the peak is centered at 0.159 microns of the volume distribution is 25.
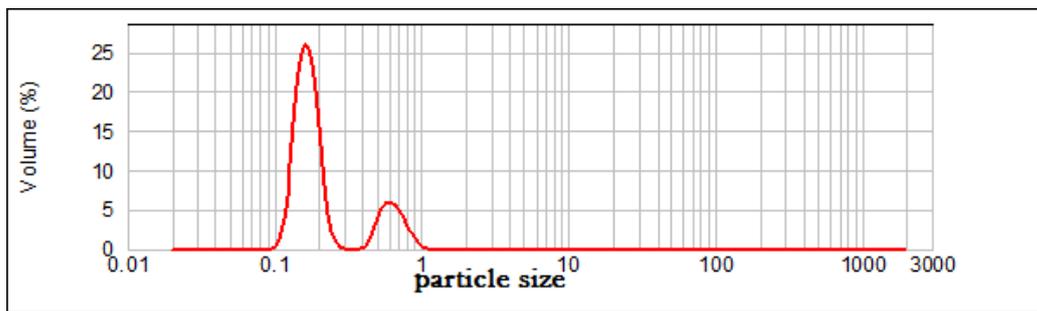
Figure III .26 Particle size distribution of LaNiO₃ prepared by sol-gel (Sucrose – water S3) after calcination.

Two modes of particle distribution of the sample S3 are shown, the first mode of which the peak is centered at 0.159 microns of the volume distribution is 26%, and it follows by second mode of 6% of the distribution whose particle diameter is 0.580 microns.
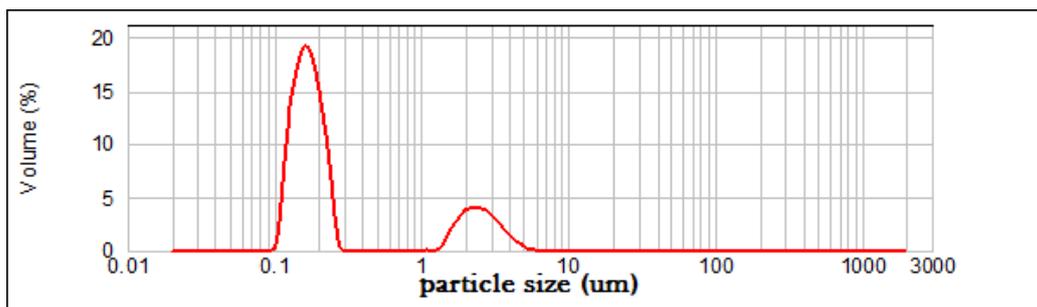
Figure III .27 Particle size distribution of LaNiO₃ prepared by sol-gel (Ascorbic acid – water S4) after calcination.

Two modes of particle distribution of the sample S4 are shown, the first mode of which the peak is centered at 0.159 microns of the volume distribution is 19%, and it follows by second mode of 4% of the distribution whose particle diameter is 2.244 microns.
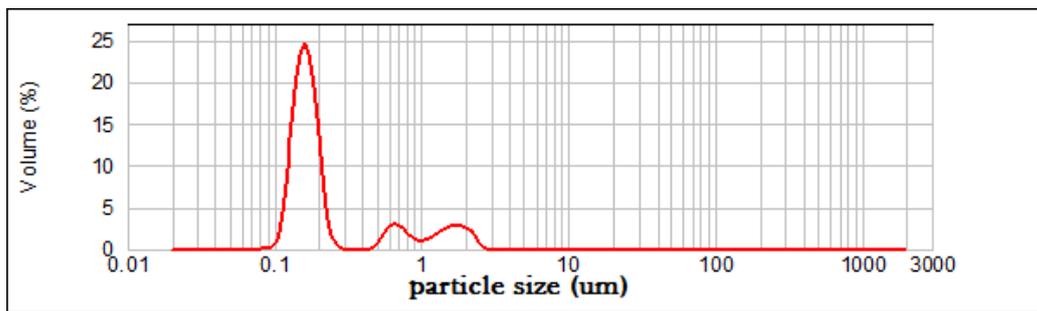
Figure III .28 *Particle size distribution of LaNiO$_3$ prepared by sol-gel combustion (Citric acid – water S5) before calcinations.*

Three modes of particle distribution of the sample S5 (before calcinations) are shown, the first mode of which the peak is centered at 0.159 microns of the volume distribution is 25%, and it follows by second mode of 2.27% of the distribution whose particle diameter is 0.630 microns, the third is at 1.589 and V= 2.16%.
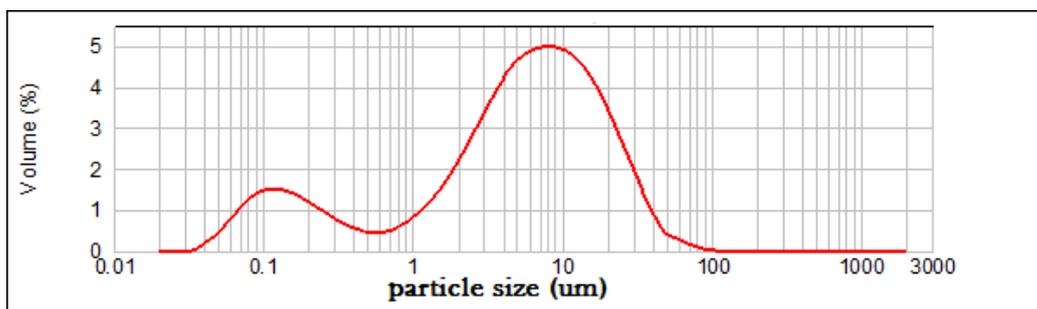
Figure III .29 *Particle size distribution of LaNiO$_3$ prepared by sol-gel combustion (Citric acid – water S5) after calcinations.*

Two modes of particle distribution of the sample S5 (before calcinations) are shown, the first mode of which the peak is centered at 0.112 microns of the volume distribution is 1.6%, and it follows by second mode of 5% of the distribution whose particle diameter is 7.096 microns.

The following table (III.1) represents the particle size of the samples prepared by different complexing agent, solvents and the synthetic methods:

Table (III.1) *particle size of the samples prepared by different complexing agent, solvents and the synthetic methods*

samples	synthetic methods	complexing agent	solvent	particle size (μm)			volume %		
S1	sol-gel	citric acid	water	12.5	-	-	15	-	-
S2	sol-gel	citric acid	ethanol	0.159	-	-	25	-	-
S3	sol-gel	sucrose	water	0.159	0.58	-	26	6	-
S4	sol-gel	ascorbic acid	water	0.159	2.244	-	19	4	-
S5 before cal	sol-gel combustion	citric acid	water	0.159	0.630	1.589	25	2.27	2.16
S5 after cal	sol-gel combustion	citric acid	water	0.112	7.096	-	1.6	5	-

It is noted that the particle size of the sample prepared by citric acid in the ethanol (0.159 μm) is similar than that prepared by the sucrose, ascorbic acid and particle size of $LaNiO_3$ prepared by sol-gel combustion (after calcination) which is lower than that synthesized by citric acid in water (12.5 μm).

The most homogeneous distribution is that of the sample prepared by citric acid in ethanol, there is one mode of distribution which is 159 nm. Not to mention the effect of dispersant and the effect of crushing ,the small particle size obtained using the sol-gel method (after calcination) but the best homogeneity is that of sample prepared by sol-gel method (citric acid - ethanol)159 nm.

III .4 Conclusion

In this work we have synthesized the perovskite LaNiO$_3$ using two methods: sol-gel and sol-gel combustion with two solvents (ethanol and water), and different complexing agents. Physicochemical characterization of the system LaNiO$_3$; have brought us to the following conclusions:

- The study by X-ray diffraction, has allows us to identify the phase of LaNiO$_3$ system at the selected temperature of calcination. And showed us that the oxides have a perovskite with rhombohedral symmetry and space group R3m.

- Chemical analysis by laser particle size, has allowed us to follow the evolution of the partical size of the oxide LaNiO$_3$ and confirm with to those of the literature; to obtain the composition of the structure of the samples initially prepared from the different precursor salts used, and to optimize their catalytic performance.

- Thermogravimetric analysis (TGA) allowed us to identify different transformations that take place during a heating cycle and the corresponding calcination temperature at the passage of the hydroxide form of the various metals in the oxide form which starts from 500 ° C to determine the stability range of the pure perovskite phase in the temperature range studied.

- Infrared spectra (IR) of the oxide LaNiO$_3$ show that the bands related to the hydroxide group and water and (C=O) have disappeared completely. The intense band observed at 420 cm^{-1} corresponds to the stretching vibration indicating the formation of the Ni-O band in all samples of oxide LaNiO$_3$ developed in both solvents (ethanol-water) and by different methods and agents of complexation to form the perovskite structure.

References

[1] Le NTH, Calderon-Moreno JM, Popa M, Crespo D, Phuc NX (2006) LaNiO$_3$ nanopowder prepared by an 'amorphous citrate' route. Eur Ceram Soc 26(4):403–407.

[2] Merino NA, Barbero BP, Grange P, Cadus LE (2005) La$_{1-x}$Ca$_x$CoO$_3$ perovskite-type oxides: preparation, characterisation, stability, and catalytic potentiality for the total oxidation of propane. J Catal 231(1):232–244.

[3] Yarbay RZ, Figen HE, Baykara SZ (2012) Effects of cobalt and nickel substitution on physical properties of perovskite type oxides prepared by the sol–gel citrate method. Acta Phys Pol A 1(121):44–46.

[4] Gonc¸alves NS, Carvalho JA, Lima ZM, Sasaki JM (2012) Size– strain study of NiO nanoparticles by X-ray powder diffraction line broadening. Mater Lett 72:36–38.

[5] Bontempi, E., Garzella, C., Valetti, S., & Depero, L. E. (2003). Structural study of LaNi $_x$Fe$_{1-x}$O$_3$ prepared from precursor salts. Journal of the European Ceramic Society, 23(12), 2135-2142.

[6] Erri, P., Dinka, P., & Varma, A. (2006). Novel perovskite-based catalysts for autothermal JP-8 fuel reforming. Chemical engineering science, 61(16), 5328-5333.

[7] Ohzeki, T., Hashimoto, T., Shozugawa, K., & Matsuo, M. (2010). Preparation of LaNi $_{1-x}$ Fe $_x$ O$_3$ single phase and characterization of their phase transition behaviors. Solid State Ionics, 181(39), 1771-1782.

[8] Rida K, Pena MA, Sastre E, Martinez-Arias A (2012) Effect of calcination temperature on structural properties and catalytic activity in oxidation reactions of LaNiO$_3$ perovskite prepared by Pechini method. J Rare Earths 30(3):210–216.

[9] Kuras, M., Roucou, R., & Petit, C. (2007). Studies of LaNiO$_3$ used as a precursor for catalytic carbon nanotubes growth. Journal of Molecular Catalysis A: Chemical, 265(1), 209-217.

[10] Barbero BP, Gamboa JA, Cadu´s LE (2006) Synthesis and characterization of La$_{1-x}$Ca$_x$FeO$_3$ perovskite-type oxide catalysts for total oxidation of volatile organic compounds. Appl Catal B 65(1):21–30.

[11] Fernandes, J. D. G., Melo, D. M. A., Zinner, L. B., Salustiano, C. M., Silva, Z. R., Martinelli, A. E., ... & Bernardi, M. I. B. (2002). Low-temperature synthesis of single-phase crystalline LaNiO$_3$ perovskite via Pechini method. Materials Letters, 53(1), 122-125.

[12] Provendier, H., Petit, C., Schmitt, J. L., Kiennemann, A., & Chaumont, C. (1999). Characterisation of the solid solution La(Ni, Fe)O$_3$ prepared via a sol-gel related method using propionic acid. Journal of materials science, 34(17), 4121-4127.

[13] Lavat AE, Baran EJ (2003) IR-spectroscopic characterization of A$_2$BB'O$_6$ perovskites. Vib Spectrosc 32(2):167–174.

[14] Zheng, W., Liu, R., Peng, D., & Meng, G. (2000). Hydrothermal synthesis of $LaFeO_3$ under carbonate-containing medium. Materials Letters, 43(1), 19-22.

[15] Devi PS, Rao MS (1992) Study of the thermal decomposition of lanthanum and chromium citrate hydrates. Anal Appl Pyrol 22(3):187–195.

[16] Wang H, Zhu Y, Liu P, Yao W (2003) Preparation of nanosized perovskite $LaNiO_3$ powder via amorphous heteronuclear complex precursor. J Mater Sci 38(9):1939–1943.

[17] Biswas, M. (2009). Synthesis of single phase rhombohedral $LaNiO_3$ at low temperature and its characterization. Journal of Alloys and Compounds, 480(2), 942-946.

[18] Oliveira, F. S., Pimentel, P. M., Oliveira, R. M. P. B., Melo, D. M. A., & Melo, M. A. F. (2010). Effect of lanthanum replacement by strontium in lanthanum nickelate crystals synthetized using gelatin as organic precursor. Materials Letters, 64(24), 2700-2703.

[19] Fernandes, J. D., Melo, D. M., Pedrosa, A. M., Souza, M. J., Gomes, D. K., & Araujo, A. S. (2005). Synthesis and catalytic properties of lanthanum nickelate perovskite materials. Reaction Kinetics and Catalysis Letters, 84(1), 3-9.

[20] Lebid M, Omari M (2014) Synthesis and electrochemical properties of $LaFeO_3$ oxides prepared via sol–gel method. Arab J Sci Eng 39(1):147–152.

Fourth chapter

Characterization and catalytic properties of La(Ni.Fe)O$_3$-NiO nanocomposites prepared by sol-gel method.

IV.1 Introduction

A sol-gel method (Pechini approach) has been used to prepare different La(Ni,Fe)O_x catalysts. In addition to the LaNiO$_3$ perovskite prepared by the same method and used as a reference sample, different formulations in which nominal amounts of Ni + Fe employed are in excess with respect to that of La have been prepared with the aim of achieving nickel substitution in the perovskite simultaneous to segregated NiO. The latter hypothesis is based on the fact that the thermodynamic stability LaFeO$_3$ is higher than that of LaNiO$_3$ [1].

In this chapter, the work is the study of physicochemical properties and structural characteristics of the perovskite La (Ni, Fe) O_x and its catalytic activity for oxidation reaction CO. For that, the samples prepared by the method sol-gel (Pechini) and calcined at 750 °C were characterized by the X-ray diffraction (XRD), surface area analysis, Fourier transform infrared (FTIR) spectroscopy and X-ray photoelectron (XPS), specific surface area (S$_{BET}$) and thermal analysis (TGA-DTA) powder size distribution (PSD) as a basis to explain their catalytic behavior for CO oxidation.

IV.2.Preparation of the oxides by the sol-gel:

Samples were prepared by the sol-gel method (Pechini approach) using citrate as complexing agent [2]. La(NO$_3$)$_3$.6H$_2$O (Sigma Aldrich), Fe(NO$_3$)$_3$.9H$_2$O (Sigma Aldrich), Ni(NO$_3$)$_3$.6H$_2$O (Sigma Aldrich), methanol (99%, from Fluka) and citric acid monohydrate C$_6$H$_8$O$_7$ (Sigma Aldrich) were used as reagents. Methanol solutions of citric acid and of the metal nitrates were prepared separately and then mixed together and agitated for 5 h. The resulting solution was then concentrated by slowly evaporating the methanol at 75 °C until a gel was obtained. This gel was then dried in an oven slowly upon increasing the temperature to 100 °C and maintaining this temperature overnight in order to produce a solid amorphous citrate precursor. The resulting precursor was finally calcined in air at 750 °C for 5 h [3, 4]; such calcination temperature was selected

on the basis of analysis of the decomposition of the precursor under air atmosphere (vide infra). Nominal amounts employed for the components in order to intend to achieve final materials with characteristics as exposed in the Introduction were of the following atomic stoichiometry: $(1-x)La + xFe + 1Ni$, with $x = 0.0, 0.1, 0.2$ and 0.3. The x value is employed for the nomenclature of the catalysts.
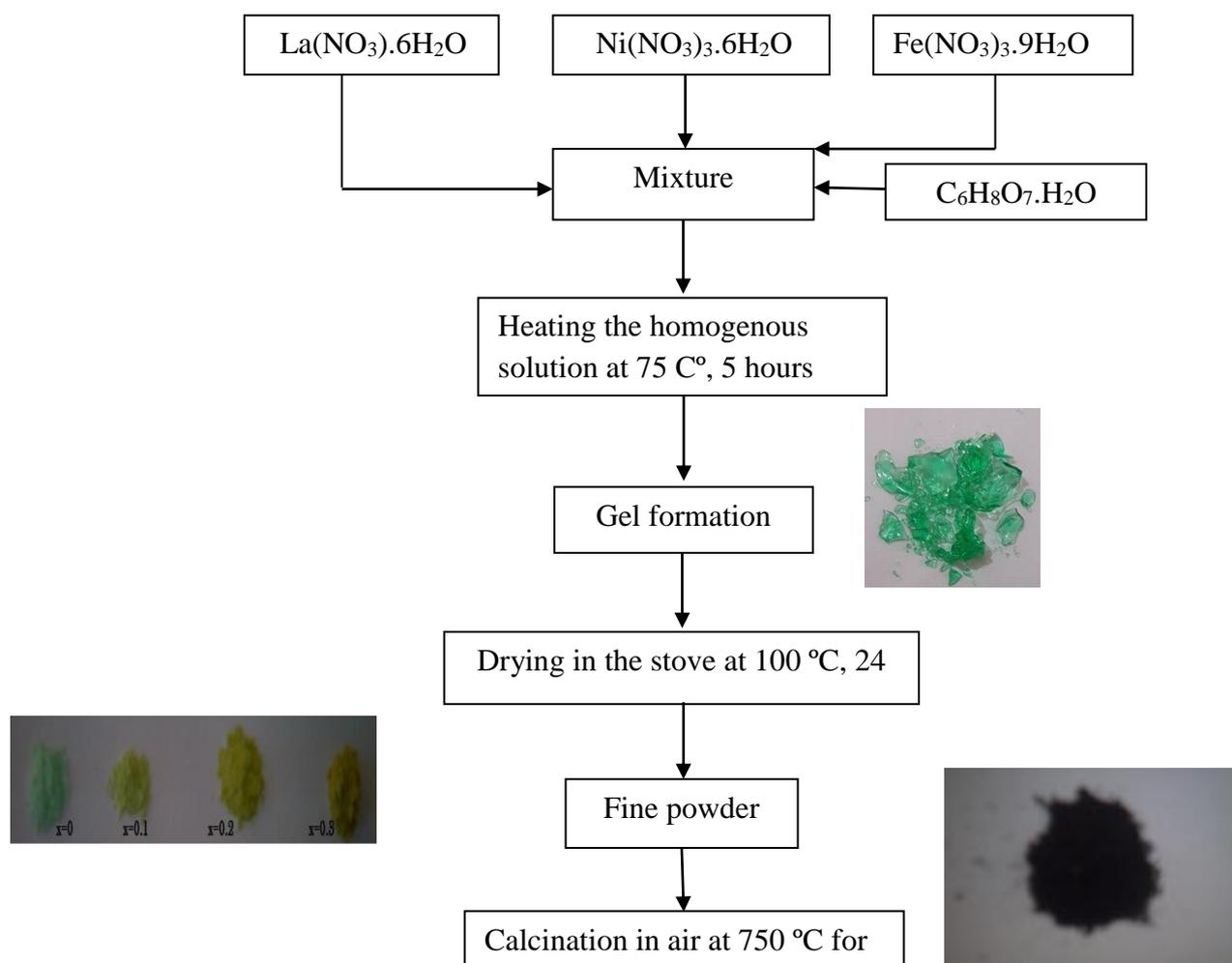
Figure IV.1 *The different steps of sol-gel synthesis.*

IV.3 Characterization and catalytic testing:

IV.3.1 X-ray diffraction

XRD Patterns were collected on a Bruker AXS D8- advance diffractometer employing Cu Kα radiation. In all diffractograms, a step size of 0.02^o (2θ) was used with a data collection time of 15 s. Data were collected between 2θ values of 10° and 80° using standard $\theta/2\theta$ geometry. Identification of crystalline phases was carried out by comparison with JCPDS standards. The unit cell parameters were obtained by fitting the peak position of the XRD pattern using the Match and X'pert Highscore programs. A reaction chamber allowing heating of the samples up to 800 ^{o}C under controlled atmosphere was also used for XRD experiments, collecting data between 30° and 60° (in 2θ) for these particular experiments. The result obtained for the compounds under study is shown in *Figure IV.2.*
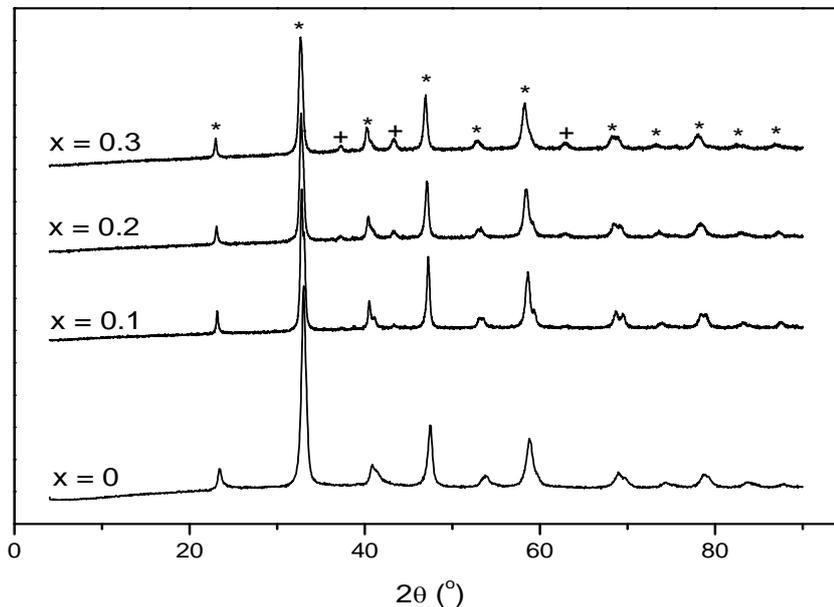
Figure IV.2 X-ray diffractograms of indicated samples calcined at 750 ^{o}C.Peaks marked with * are attributed to LaNiO$_3$ (or Fe-substituted) perovskite and those marked with + correspond to NiO.

XRD patterns of the samples are shown in *Figure IV.2*. As expected, the sample with x = 0 displays the pattern of $LaNiO_3$ perovskite-type phase with rhombohedral symmetry, space group R3m [5]. A shift to lower angle of the peaks of this perovskite phase is observed upon increasing x. This corresponds to pseudocubic lattice constant of 3.836, 3.854, 3.865 and 3.877 Å for x = 0, 0.1, 0.2 and 0.3, respectively.

The increase in lattice constant with increasing x is consistent with Ni substitution by Fe in the perovskite, taking into account pseudocubic lattice constant values of 3.84 Å for $LaNiO_3$ and 3.93 Å for $LaFeO_3$ [6,7]. This is also in accordance with mentioned thermodynamic stability of corresponding perovskites which would favor such substitution. Additional peaks are shown to grow with increasing x, the most intense ones appearing at 2θ~ 37.2, 43.3 and 62.8° which correspond to cubic NiO [8]. Crystal size estimate from use of the Scherrer equation for the major perovskite phase are of 14.7, 24.1, 19.2 and 21.1 nm for x = 0, 0.1, 0.2 and 0.3, respectively.

No direct correlation can be established between these values and those of S_{BET} and pore volumes or grain sizes (*Table IV.1* and *Figure IV.6*), suggesting that the specific surface area becomes basically determined by morphological properties of the $NiO-La(Ni,Fe)O_3$ nanoheterostructures formed in each case.

IV.3.2 Infrared spectroscopy

Infrared transmission spectra were performed on a Fourier transform spectrometer (FTIR) Shimadzu 8400S. A granular technique employing KBr (1 mg of sample added to 200 mg of KBr) was used and the spectra were recorded in the 400-4000 cm-1 range.

Samples with x = 0 and 0.3 have been explored by infrared, as shown in Figure IV.3 .The spectra show strong and well-defined absorption bands, typical of perovskite oxides; Typically, the vibrations the M-O (M = Ni, Fe) vibrations of octahedral MO_6 units dominate the spectra [9]. The bands at higher wavenumbers

(580-675 cm^{-1}) are assigned to the stretching modes of the MO_6 octahedral unit and those at 400-500 cm^{-1} to the deformation of this same polyhedral unit [9, 10].

The effect of Fe incorporation appears related to an important increase of a band at ca. 570 cm^{-1} which is attributed to Fe-O stretching vibration [11] while the increase observed in the band at ca. 470 cm^{-1} band, which can be attributed to Ni-O vibration, is attributed to formation of NiO, in accordance with XRD results (*Figure IV.2*).
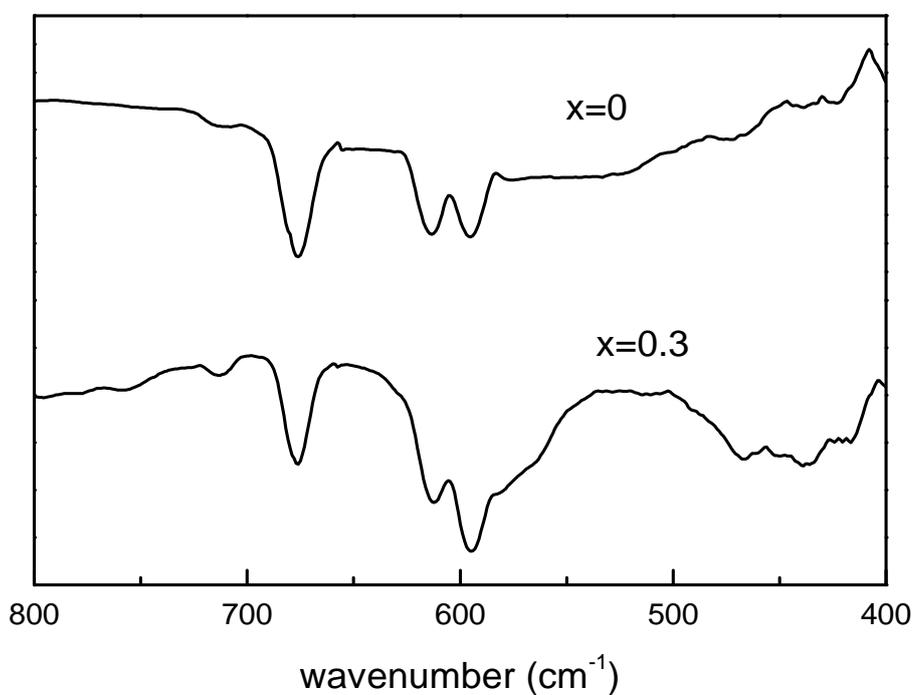
Figure IV.3 *FTIR spectra of samples with x = 0 (top) and 0.3 (bottom).*

IV.3.3 Thermal characterizations (TGA-DTA) of precursors

Thermogravimetric and differential thermal analyses (TGA-DTA) of the precursor decomposition were performed on a Perkin-Elmer TGA7 and a Perkin-Elmer DTA7 devices, respectively, from 20 to 900 ℃ at a heating rate of 20 ℃ min^{-1} and under an air flow of ca. 60 ml min^{-1}.

The precursors (after the drying step of the preparation at 100 C^{o}) were examined by TGA-DTA in order to explore their decomposition under atmospheric air and with the aim of establishing most adequate calcination conditions for them. The results are displayed in *Figure (IV -3.4).*

Basically four decomposition processes are identified. A first endothermic one taking place up to ca. 180 ℃ and which must be related to the desorption of adsorbed or hydration water that may remain in the precursors [5,12,13].

The second one represents an important mass loss (ca. 45%) and takes place between ca. 160 and 350 ℃ corresponding to an exothermic process. Such mass loss appears consistent with the oxidative decomposition of citrates complexing the metals in the precursors [5].

The third one takes place between ca. 350 and 450 ℃ and corresponds to a mass loss of about 10%. It could be related to the exothermic decomposition of carbonat or carboxylate-type complexes remaining in the samples, according to previous analogous investigation of samples of this kind by infrared [5].

The final process occurs slowly above ca. 450 ℃ and must correspond to the final exothermic crystallization of the oxides, as will be confirmed below, along with the slow decomposition of more persistent residual carbonate- or carboxylate-type species [5].

Some differences appear between the samples as a function of the iron content x. Basically, weight loss processes involving decomposition of organic precursors appear shifted to lower temperature while the final crystallization process reflected by the strong exothermic peak between 450 and 650 ℃ appears shifted to higher temperature with increasing x. The width of the different processes

generally increases with increasing x as a consequence of the increasing heterogeneity in the system.
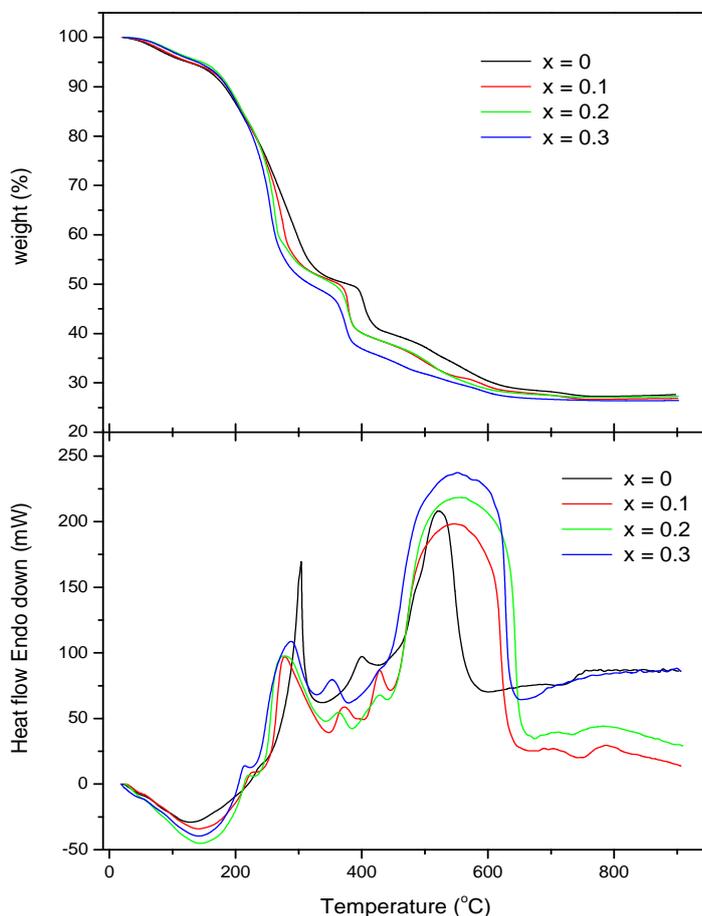
Figure IV 4. TGA (top) and DTA (bottom) curves during heating under air of the indicated powder precursors.

These results have been complemented by XRD during heating of the precursors under air in a reaction chamber. Figure IV.5 displays the results obtained for the two extreme x values. Amorphous patterns are observed in any case up to ca. 400 °C at which some peaks begin to appear most likely corresponding to the formation of residual lanthanum oxy-carbonate species [13].

LaNiO$_3$ perovskite peaks (or the corresponding perovskite partially substituted with Fe at the B position) begin to appear at 600 $^{\circ}$C for x = 0 and at 650 $^{\circ}$C for x = 3. This is consistent with TGA-DTA analysis showing that the final crystallization process becomes shifted to high temperature in the presence of iron. Noteworthy, segregated NiO appears for x = 3 and apparently starts to form above ca. 450 $^{\circ}$C and grows with the calcination temperature. In any case, the crystallization process appears complete at 750 $^{\circ}$C. On this basis and considering also the TGA-DTA results showing that decomposition processes are practically over above 750 $^{\circ}$C, this calcination temperature has been chosen to prepare the samples.
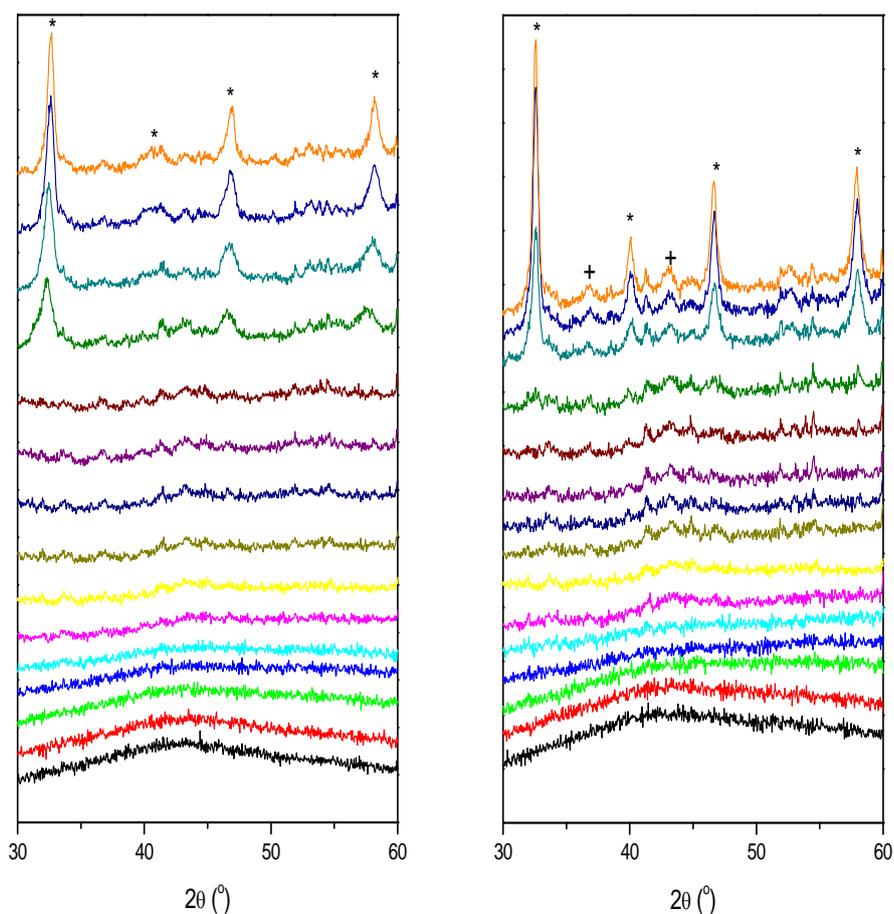
Figure IV.5 *X-ray diffractograms during heating under air of the powder precursors.*

IV.3.4 specific surface area (S_{BET})

The specific surface area of the samples (S_{BET}) was determined by applying the BET method to nitrogen adsorption/desorption isotherms recorded at -196 °C, using a Micrometrics apparatus model ASAP-2000. Prior to adsorption, the samples were degassed overnight at 140 C^o. Pore volume (single point adsorption total pore volume of pores less than ca. 80 nm diameter at P/Po ca. 0.98 and t-Plot micropore volume) was also determined from corresponding analysis of the isotherms.

Table IV.1 *Main textural properties of the La(Fe,Ni)O₃ samples*

Sample	S_{BET} (m^2g^{-1})	Total pore volume (cm^3 g^{-1})	Micropore volume (cm^3g^{-1})
x = 0	4.7	0.0175	0.000327
x= 0.1	3.8	0.0112	0.000229
x = 0.2	3.7	0.0154	0.000162
x =0.3	3.4	0.0179	0.000122

Table IV.1 summarizes the basic textural properties of the samples. As noted, the S_{BET} and micropore volume of the samples monotonically decrease with increasing x while the total pore volume shows a minimum at x = 0.1. This latter suggests that the specific surface area can be determined by the balance between the crystal size and the degree of agglomeration of the nanocrystals in each case.

The observed S_{BET} decrease can in this sense be basically determined by the crystal size increase expected upon nickel substitution by iron in the perovskite [14].

IV.3.5 powder size distribution (PSD)

The analysis of the distribution of the grain size of the samples was employed in order to show the influence of the Fe/Ni substitution and the synthetic method employed on the particle size by laser granulometry. After calcination at 750 °C the powder was dispersed in deionized water in a beaker with magnetic stirring and combined under ultrasound for 15 minutes. Powder size distribution was characterized with a laser particle size analyzer (Mastersizer 2000, Malvern) [15].
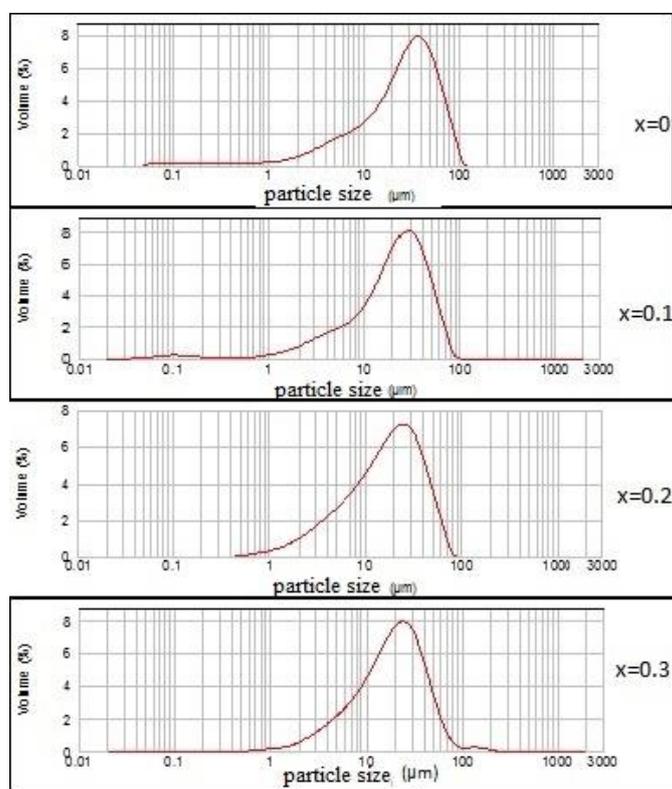
Figure IV.6 Particle size distribution of samples with x = 0, 0.1, 0.2 and 0.3.

The grain size of the different oxides calcined at 750 °C, according to PSD measurements, is shown in *Figure IV.6*. The size distribution of the x = 0, 0.1, 0.2 and 0.3 samples shows a maximum at ca. 35.6, 28.3, 24.1 and 23.8 microns, respectively .

Size distributions obtained with maximum at tens of microns must result from agglomeration of primary particles. The decrease of the particle size observed upon increasing x contrasts with the evolution observed in S_{BET} values, *Table IV.1*

IV .3.6 X-ray photoelectron spectroscopy(xps)

X-ray photoelectron spectroscopy was performed with a VG Escalab 200 R spectrometer employing Al Kα (1486 eV) as x-ray source. The sample was first placed in a stainless steel holder mounted on a sample-rod in the pretreatment chamber of the spectrometer and then outgassed (at ca 10-5 Torr) at room temperature for 1 h before being transferred to the ultrahigh vacuum analysis chamber. A selected region of the XPS spectrum (La 3d, Ni 2p, Fe 2p, O 1s, and C 1s) was then scanned for a determinate number of times such as to obtain a good signal to noise ratio.

The binding energies (BE) were referenced to the spurious C 1s peak (taken at 284.6 eV) used as internal standard to take into account charging effects. Peak areas were computed by fitting the experimental spectra to Gaussian/Lorentzian curves after removal of the background (Shirley function). Surface atom ratios were calculated from the peak areas normalized by corresponding atomic sensitivity factor [16, 17].

The surface characteristics of the samples were examined by XPS. Relevant atomic ratio values as well as binding energies determined from the fittings for the main peaks in La 3d, Ni 2p and O 1s zones are collected in *Table IV.2* while corresponding spectra are shown in *Figure IV.7, 8 and 9.* Spectra in the zone corresponding to La 3d and Ni 2p are complicated as a consequence of important overlapping between La $3d_{3/2}$ and Ni $2p_{3/2}$ components. No significant differences were detected between the spectra observed for the samples in the La 3d zone. These displayed the typical two peaks of La $3d_{3/2}$ located at ca. 853.8 and 850.3 eV and those of La $3d_{5/2}$ at ca. 837.5 and 833.9 eV, close to those expected for La^{3+} ions in an oxidic environment [18,19].

Concerning Ni 2p features, the most intense Ni $2p_{3/2}$ peak appears, according to fitting results, at around 855.4 eV while the Ni $2p_{1/2}$ component appears at ca. 872.2 eV, which are characteristic of Ni^{2+}/Ni^{3+} ions in an oxidic environment [5,20]. Additionally, a satellite line appears at ca. 7 eV higher BE. This must arise from Ni^{2+} ions, which allows concluding that the surface of all the perovskite oxides contains a certain proportion of Ni^{2+} along with Ni^{3+} ions. An analysis of the relative contribution of this satellite peak to the spectra provides in this sense hints on the relative amount of surface Ni^{2+} species. Thus, if we consider a factor $I_{sat}/(I_{Ni2p1/2} \times I_{La837})$ (normalized to one of the La $2p_{5/2}$ peaks at ca. 837 eV in order to take account that some small La Auger contribution could appear in the same zone as the Ni $2p_{3/2}$ satellite peak and taking the Ni $2p_{1/2}$ intensity, free of overlapping, as reference for the main Ni 2p XPS peaks), it evolves as (normalized to the sample x = 0) 1, 0.99, 1.84 and 1.39 for x = 0, 0.1, 0.2 and 0.3, respectively. This is consistent with a general increase of the Ni^{2+} portion with increasing x and therefore with the fact that segregated NiO locates at the surface of the La(Ni,Fe)O_3 perovskite.

   The fact that no important difference is observed in such factor between x = 0 and x = 0.1 suggests that Fe substitution of Ni cations in the perovskite could favour to some extent the stabilization of Ni^{3+} at the surface. In turn the decrease observed in such factor for the sample with x = 0.3 could be related to the sintering of NiO, also consistent with a decrease in the relative Ni atomic ratio observed for this sample (*Table IV.2*). On the other hand, the O 1s spectra show two contributions at ca. 528.5 and 531.0 eV which can be assigned to lattice oxygen and chemisorbed (in the form of hydroxyls or carbonate-related species) oxygen species, respectively [5, 21]. Apparently, the increase of x produces a decrease of the relative amount of chemisorbed oxygen species, as shown in Table 2. In turn, the Fe 2p spectra display Fe $2p_{3/2}$ peak at 712.2-711.0 and Fe $2p_{1/2}$ at 723.0-721.2 eV. Practically no satellite peak is apparent according to examination of the highest energy zone related to Fe $2p_{1/2}$ features.
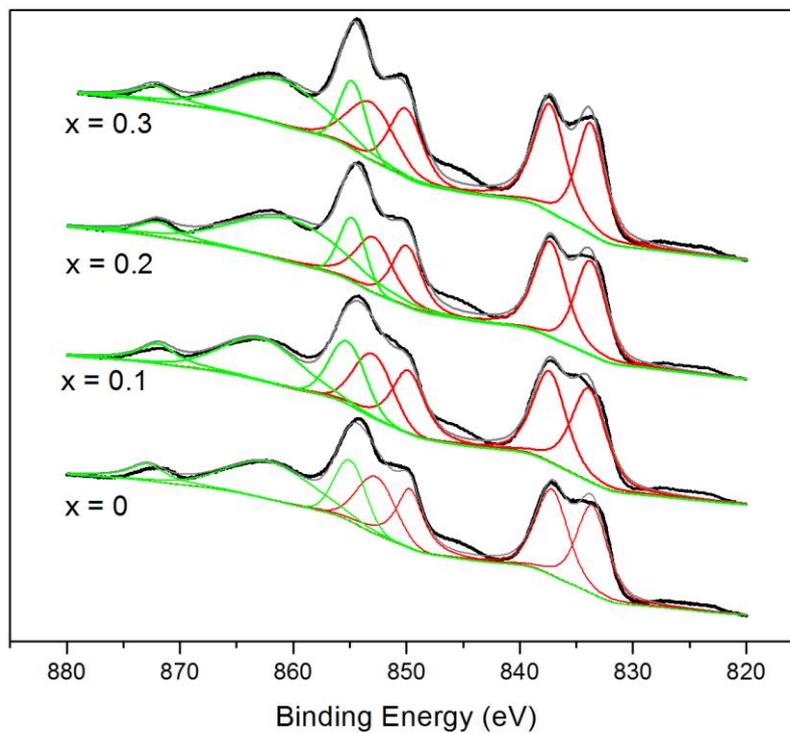
Figure IV.7 XPS spectra in the La 3d–Ni 2p region for indicated samples. Lines in red are attributed to La 3d features and those in green to Ni 2p features.
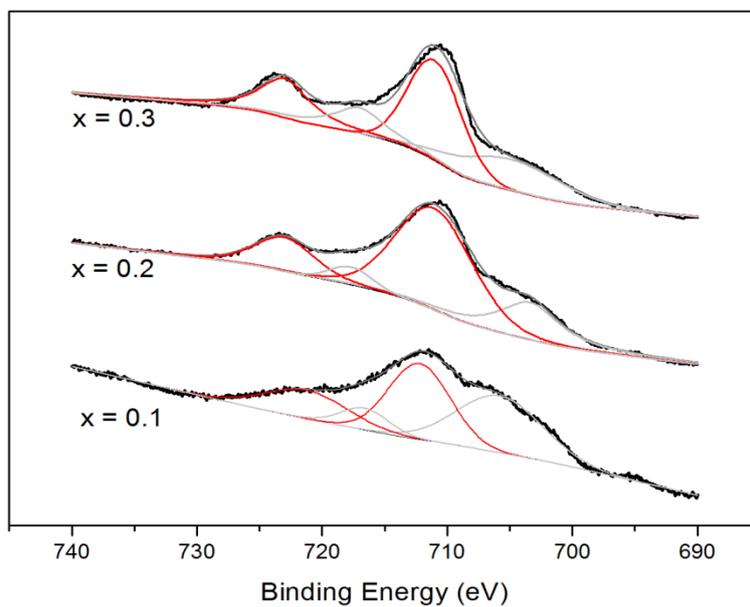
Figure IV.8 XPS spectra in the Fe 2p region for indicated samples. Red lines are attributed to Fe 2p features and those in gray to Ni Auger peaks.
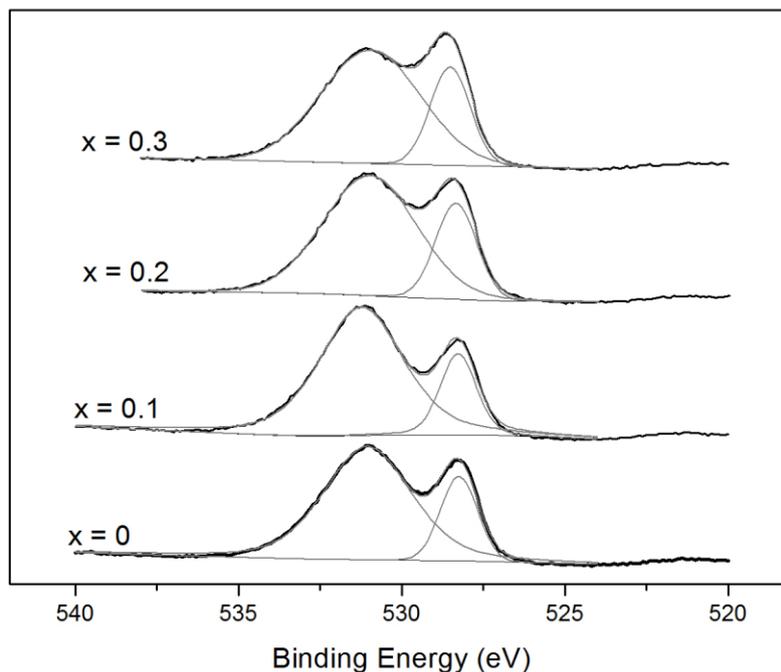
Figure IV.9 XPS spectra in the O 1s region for the indicated samples.

The spectra appear quite similar to those attributed to Fe^{3+} species in a perovskite environment like those observed in previous studies of the $LaFeO_3$ perovskite [22,23].The main difference as a function of x appears in this case related to the spectrum observed for the sample x = 0.1 which displays somewhat higher Fe $2p_{3/2}$ binding energy and apparently lower spin-orbit splitting. This reflects an electronic modification of the Fe^{3+} species for relatively low substitution level in the La-Ni perovskite and which can be related to an increase of the ionic character of the Fe^{3+} cations [24]. Finally, the C 1s core level spectra (not shown) displayed three components (*Table IV.2*). Two of them at ca. 284.5 and 285.5 eV come from spurious carbon resulting from atmospheric hydrocarbons contamination while a third peak around 289.1 can be attributed to residual carbonate species [21].

Table IV.2 Binding energies of indicated XPS peaks (values between parentheses correspond to relative contributions to the spectra) and representative atomic ratios estimated from the XPS spectra (nominal values between parentheses).

Sample	XPS binding energies (eV)					Atomic ratios	
	La 3d$_{5/2}$	Ni 2p$_{1/2}$	Fe 2p$_{3/2}$ Fe 2p$_{1/2}$	O 1s	C 1S	Ni/(La+Ni+Fe)	Fe/(La+Ni+Fe)
x = 0	833.5	872.3	-	528.3 (21.5) 531.1 (78.5)	289.1 (51.3) 285.3 (28.4) 284.4 (20.3)	0.54 (0.50)	-
x = 0.1	833.9	872.0	712.2 721.2	528.30 (25.2) 531.2 (74.8)	289.2 (58.1) 285.5 (23.3) 284.6 (18.6)	0.50 (0.50)	0.08 (0.05)
x = 0.2	833.7	872.0	711.1 723.0	528.50 (25.6) 531.08 (74.4)	289.2 (47.6) 285.7 (21.9) 284.6 (30.5)	0.52 (0.50)	0.12 (0.10)
x = 0.3	833.7	872.2	711.0 723.0	528.5 (25.7) 531.0 (75.3)	289.2 (41.8) 285.5 (30.1) 284.5 (28.1)	0.46 (0.50)	0.15 (0.15)

IV.3.7 Catalytic test on the oxidation reaction of CO

The catalysts were tested for the CO oxidation reaction at atmospheric pressure. 100 mg of powder sample was mixed homogeneously with SiC to obtain a total volume of ca. 1 ml. The mixture was then loaded in a cylindrical Pyrex reactor tube. The total flow rate employed was in all cases of 100 ml min^{-1} and a feed composition of 1% CO and 2% O_2 was employed (volume percentages balanced with N_2 employed as carrier gas; mass flow controllers being used for this purpose). The products of the reaction were analysed by infrared spectroscopy using a Perkin-Elmer 1725X FTIR spectrometer fitted with a multiple reflection transmission cell for gas analysis (Infrared Analysis).

Carbon dioxide gas bands in the 2400–2200 or 750–600 cm^{-1} range (depending on the degree of saturation of the most intense former ones) and the band of CO gas in the range of 2250-2000 cm^{-1} were employed to determine conversion levels. In all cases, the samples were pre-treated under diluted O_2 (20 % in N_2) at 500 $^{\circ}$C and then tested in light-off mode using a ramp of 5 $^{\circ}$C min^{-1} .The four samples were tested in the oxidation (conversion) of CO. *Figure IV 10* shows the catalytic activity results obtained.
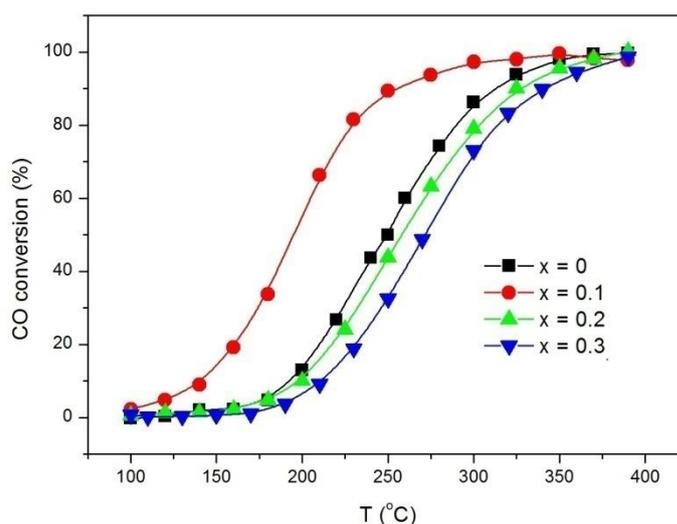
Figure IV.10 Catalytic activity for CO oxidation over the indicated samples.

The catalytic activity shows a maximum for the sample with x = 0.1 and higher x values do not provide any enhancement with respect to the reference x = 0 sample while the activity apparently decreases with increasing x above x = 0.1.

These results evidence that optimum catalytic properties for this reaction are achieved upon weak substitution of Ni by Fe in the perovskite within nanocomposite configuration interacting with very small well dispersed NiO entities. The cooperative effect of $LaFe_{1-x}Ni_xO_3$ and NiO phases was claimed in a previous study as most relevant to explain the catalytic properties of the substituted perovskite for VOC's (ethanol and acetyl acetate) combustion while the activity is shown to increase with the amount of Ni in the substituted perovskite [25] ; in turn, the enhancing effects of phase cooperation within multiphase perovskite-based catalysts have been also reported, which suggests that the specific interactions between the various phases present in the system play the most relevant on the catalytic activity [26,27].

On the other hand, achievement of optimum dispersion between the interacting active phases is most important in order to attain optimized catalytic properties [25, 28, 29, 30]; this is related not only to achievement of optimum characteristics in the supported oxide nanoparticles themselves, i.e. more defective and active surfaces which are generally attainable upon decreasing the particle size [31], but also in the active interface formed between the two active interacting phases [32].

Concerning mechanistic aspects, the catalytic differences must be generally related to differences in the oxygen handling properties (adsorption, transport) achieved in each case within a suprafacial or intrafacial catalytic mechanism [28]. In this sense,The capability of Ni^{3+} ions into the $LaFe_{1-x}Ni_xO_3$ structure for modulating oxygen adsorption and release properties along with mentioned cooperation with segregated NiO phase were pointed out previously as most important factors to enhance VOC's combustion performance [25]. Our activity results present similarities in this sense. The most active catalyst with x = 0.1 is the one exhibiting the highest surface concentration of Ni^{3+} according to XPS

results (*Figure IV.7* and *Table IV.2)*, on which oxygen activation can be most favored [25].

Nevertheless, taking into account that Ni^{3+} concentration of the sample x = 1 appears similar to that with x = 0, iron substitution in the perovskite as well as the presence of interacting segregated NiO entities are pointed out as most important factors to take into account in order to achieve maximum CO oxidation activity over the nanocomposite catalysts.

IV.4 Conclusion

A sol-gel method (Pechini approach) has been used to prepare different La(Ni,Fe)O$_x$/NiO nanocomposite materials. In addition to the LaNiO$_3$ perovskite prepared by the same method and used as a reference sample, different formulations in which nominal amounts of Ni + Fe employed are in excess with respect to that of La have been prepared with the aim of achieving nickel substitution by iron in the perovskite simultaneous to segregated NiO.

TGA-TDA and XRD analysis of the decomposition of the precursors show that minimum temperature to achieve full crystallization of the components is 750 ºC. The textural properties of corresponding materials calcined at 750 ºC have been explored by S$_{BET}$ measurements and PSD analysis, demonstrating that the agglomeration degree of primary particles increases with increasing the amount of iron. Characterisation by XRD and XPS have demonstrated the formation of mentioned nanocomposite structures for which optimum catalytic properties for the CO oxidation reaction are apparently achieved for a weak substitution level in the substituted perovskite interacting with small well-dispersed NiO entities.

References

[1] Cheng J, Navrotsky A, Zhou XD, Anderson HU (2005) Enthalpies of formation of LaMO$_3$ perovskites (M = Cr, Fe Co, and Ni). Mater Res 20(1):191–200.

[2] Le NTH, Calderón-Moreno JM, Popa M, Crespo D, Phuc NX (2006) LaNiO$_3$ nanopowder prepared by an 'amorphous citrate' route. EUR Ceram Soc 26(4):403- 407.

[3] Merino NA, Barbero BP, Grange P, Cadús LE (2005) La$_{1−x}$Ca$_x$CoO$_3$ perovskite-type oxides: preparation, characterisation, stability, and catalytic potentiality for the total oxidation of propane. J of Catal 231(1):232-244.

[4] Yarbay RZ, Figen HE, Baykara SZ (2012) Effects of Cobalt and Nickel Substitution on Physical Properties of Perovskite Type Oxides Prepared by the Sol–Gel Citrate Method. Acta Phys Polo A 1(121):44-46.

[5] Rida K, Pena MA, Sastre E, Martinez-Arias A (2012) Effect of calcination temperature on structural properties and catalytic activity in oxidation reactions of LaNiO$_3$ perovskite prepared by Pechini method. J Rare Earths 30(3):210–216.

[6] Provendier H, Petit C, Kiennemann A (2000) Catalytic behavior of Ni containing catalysts in vaporeforming of methane with low H2O/CH$_4$ ratio and free carbon deposition.Stud Surf Sci Catal 130 : 683-888.

[7] Clemens O, Berry FJ, Wright AJ, Knight KS, Perez-Mato JM, Igartua JM, Slater PR (2013) A neutron diffraction study and mode analysis of compounds of the system La$_{1- x}$Sr$_x$FeO$_3$ (x =1, 0.8, 0.5, 0.2) and an investigation of their magnetic properties. J Sol St Chem. 206 :158-169.

[8] Gonçalves NS, Carvalho JA, Lima ZM, Sasaki J M (2012) Size–strain study of NiO nanoparticles by X-ray powder diffraction line broadening. Mater Lett 72:36-38.

[9] Lavat AE, Baran EJ (2003) IR-spectroscopic characterization of A$_2$BB′O$_6$ perovskites. Vibrat Spectrosc. 32(2):167-174.

[10] Barbero BP , Gamboa JA , Cadús LE (2006) Synthesis and characterization of La$_{1−x}$Ca$_x$FeO$_3$ perovskite-type oxide catalysts for total oxidation of volatile organic compounds. Appl Catal B 65(1):21-30.

[11] Rao GV, Rao CNR, Ferraro JR (1970) Infrared and Electronic Spectra of Rare Earth Perovskites: Ortho-Chromites, -Manganites and –Ferrites. Appl Spect 24(4): 436-445.

[12] Devi PS, Rao MS (1992) Study of the thermal decomposition of lanthanum and chromium citrate hydrates. Anal and Appl Pyrolysis 22(3): 187-195.

[13] Wang H, Zhu Y, Liu P, Yao W (2003) Preparation of nanosized perovskite LaNiO$_3$ powder via amorphous heteronuclear complex precursor. J of Mat Sci 38 (9):1939-1943.

[14] Tejuca LG, Fierro JLG (1989) XPS and TPD probe techniques for the study of LaNiO$_3$ perovskite oxide. Therm Acta 147(2): 361-375.

[15] Lebid M, Omari M (2014) Synthesis and Electrochemical Properties of $LaFeO_3$ Oxides Prepared Via Sol–Gel Method. Arab J Sci Eng 39(1):147–152.

[16] Venezia AM (2003) X-ray photoelectron spectroscopy (XPS) for catalysts characterization. Catal Today 77(4):359–370.

[17] Wagner CD, Davis LE, Zeller MV, Taylor JA, Raymon RH, Gale LH (1981) Empirical Atomic sensitivity Factors for Quantitative Analysis By electron Spectroscopy for chemical analysis. Surf Interf Anal 3(5):211-225.

[18] Uwamino Y, Ishizuka T, Yamatera H(1984) X-ray photoelectron spectroscopy of rareearth compounds. Elect Spect Rel Phenom 34(1):67-78.

[19] Rida K, Benabbas A, Bouremmad F, Peña MA, Martínez-Arias A (2006) Surface properties and catalytic performance of $La_{1-x}Sr_xCrO_3$ perovskite-type oxides for CO and C_3H_6 combustion. Catal Commun 7(12):963-968.

[20] Damyanova S, Daza L, Fierro JLG(1996) Surface and Catalytic Properties of LanthanumPromoted Ni/Sepiolite Catalysts for Styrene Hydrogenation. Catal 159(1):150-161.

[21] De la Cruz RG, Falco´n H, Pen˜a MA, Fierro JLG (2001) Role of bulk and surface structures of $La_{1-x}Sr_xNiO_3$ perovskite-type oxides in methane combustion. Appl Catal B 33(1):45–55.

[22] Cho YG, Choi KH, Kim RY, Jung JS, Lee SH (2009) Characterization and Catalytic Properties of Surface La-rich $LaFeO_3$ Perovskite. Bull Kor Chem Soc 30(6):1368-1372.

[23] Parida KM, Reddy KH, Martha S, Das DP, Biswal N (2010) Fabrication of nanocrystalline $LaFeO_3$: An efficient sol-gel auto-combustion assisted visible light responsive photocatalyst for water decomposition. Int J of Hydr Ener 35(22):12161-12168.

[24] Grosvenor AP, Kobe BA, Biesinger MC, McIntyre NS(2004) Investigation of multiplet splitting of Fe 2p XPS spectra and bonding in iron compounds. Surf Interf Anal 36(12):1564-1574.

[25] Pecchi G, Reyes P, Zamora R, Cadu´s LE, Fierro JLG (2008) Surface properties and performance for VOCs combustion of $LaFe_{1-y}Ni_yO_3$ perovskite oxides. Solid State Chem 181(4):905–912.

[26] Kirchnerova J, Alifanti M, Delmon B (2002) Evidence of phase cooperation in the $LaCoO_3$–CeO_2–Co_3O_4 catalytic system in relation to activity in methane combustion. Appl Catal A 231(1):65-80.

[27] Rida K, Benabbas A, Bouremmad F, Peña MA, Sastre E, Martínez-Arias A (2007) Effect of calcination temperature on the structural characteristics and catalytic activity for propene combustion of sol–gel derived lanthanum chromite perovskite. Appl Catal A 327(2):173-179.

[28] Pen˜a MA, Fierro JLG (2001) Chemical structures and performance of perovskite oxides. Chem Rev 101(7):1981–2018.

[29]   Peren˜iguez R, Gonzalez-delaCruz VM, Caballero A, Holgado JP (2012) LaNiO$_3$ as a precursor of Ni/La$_2$O$_3$ for CO$_2$ reforming of CH$_4$: effect of the presence of an amorphous NiO phase. Appl Catal B 123:324–332.

[30] Wang CT, Ro SH (2005) Nanocluster iron oxide-silica aerogel catalysts for methanol partial oxidation. Appl Catal A 285(1):196-204.

[31] Fernández-García M, Martínez-Arias A, Hanson JC, Rodriguez JA (2004) Nanostructured Oxides in Chemistry: Characterization and Properties. Chem Rev 104(9):4063-4104.

[32] Kubacka A, Martínez-Arias A, Fernández-García M (2015) Role of the Interface in Base Metal Ceria-Based Catalysts for Hydrogen Purification and Production Processes. Chem Cat Chem. Doi: 10.1002/cctc.201500593.

General conclusion

General conclusion

In this work, our contribution focused on the synthesis, physicochemical characterizations of different La (Ni/Fe) O_2/NiO nanocomposite materials.

In the first part, the work aims to preparing $LaNiO_3$ perovskite oxides by different synthesis methods (sol-gel and sol gel combustion) with two solvents (ethanol and water), and different complexing agents. The samples were characterized by several techniques (XRD, TGA, FTIR, and PSD).

➤ The study by X-ray diffraction, has allows us to identify the phase of $LaNiO_3$ system at the selected temperature of calcination. And showed us that the oxides have a perovskite with rhombohedral symmetry and space group R3m.

➤ Chemical analysis by laser particle size, has allowed us to follow the evolution of the partical size of the oxide $LaNiO_3$ and confirm with to those of the literature; to obtain the composition of the structure of the samples initially prepared from the different precursor salts used, and to optimize their catalytic performance.

➤ Thermogravimetric analysis (TGA) allowed us to identify different transformations that take place during a heating cycle and the corresponding calcination temperature at the passage of the hydroxide form of the various metals in the oxide form which starts from 500 ° C to determine the stability range of the pure perovskite phase in the temperature range studied.

➤ Infrared spectra (IR) of the oxide $LaNiO_3$ show that the bands related to the hydroxide group and water and (C=O) have disappeared completely. The intense band observed at 420 cm^{-1} corresponds to the stretching vibration indicating the formation of the Ni-O band in all samples of oxide $LaNiO_3$ developed in both solvents (ethanol-water) and by different methods and agents of complexation to form the perovskite structure.

In the second part: we prepared $LaNiO_3$ perovskite oxide by the same method and used as a reference sample, different formulations in which nominal amounts of Ni + Fe employed are in excess with respect to that of La have been prepared with the aim of achieving nickel substitution by iron in the perovskite simultaneous to segregated NiO.

TGA-TDA and XRD analysis of the decomposition of the precursors show that minimum temperature to achieve full crystallization of the components is 750°C. The textural properties of corresponding materials calcined at 750°C have been explored by S_{BET} measurements and PSD analysis, demonstrating that the agglomeration degree of primary particles increases with

Increasing the amount of iron. Characterization by XRD and XPS have demonstrated the formation of mentioned nanocomposite structures for which optimum catalytic properties for the CO oxidation reaction are apparently achieved for a weak substitution level in the substituted perovskite interacting with small well-dispersed NiO entities.

Abstract

Nanocomposite structures involving LaNiO$_3$ perovskite partially substituted with iron and segregated NiO are synthesized by sol–gel and sol gel combustion methods using citric acid, ascorbic acid, sucrose, as chelating agents and methanol, ethanol, water as solvents. X-ray diffraction (XRD) and thermogravimetric, differential thermal analysis techniques are used to explore precursor decomposition and to establish adequate calcination temperature for the preparation of the nanocomposites. The samples obtained after calcination at 750, 800°C were characterized by XRD, X-ray photoelectronic spectroscopy, Brunauer–Emmett–Teller surface area analysis, Fourier transform infrared spectroscopy and powder size distribution, and tested for the catalytic oxidation reaction of CO. Optimum catalytic properties are shown to be achieved for nanocomposites with relatively weak Fe/Ni substitution degree in the perovskite interacting with well-dispersed small NiO entities.

Résumé

Les nanocomposites LaNiO$_3$ de structure perovskite partiellement substitués par du Fer et la ségrégation du NiO sont synthétisés par des procédés sol-gel et sol-gel combustion en utilisant de l'acide citrique, l'acide ascorbique, le saccharose, à titre d'agents chélatants et le méthanol, l'éthanol, l'eau comme des solvants. La diffraction des rayons X (XRD), thermogravimétrie et thermogravimétrie différentielle, des techniques utilisées pour explorer la décomposition des précurseurs et d'établir la température de calcination appropriée pour la préparation des nanocomposites. Les échantillons obtenus après calcination à 750, à 800 ° C ont été caractérisés par : diffraction des rayons X, XPS (spectroscopie photoélectronique des rayons X), analyse de la surface Brunauer-Emmett-Teller, la spectroscopie infrarouge à transformée de Fourier et la distribution granulométrique des poudres et l'évaluation de l'activité catalytique assurée par oxydation catalytique de CO. Les nanocomposites avec un faible degré de substitution de Fe/Ni et une bonne dispersion de NiO présentent des propriétés catalytiques optimales.

<div dir="rtl">

الملخص

في هذا العمل تم اصطناع مركبات ذات بنى نانومتريه من أكسيد LaNiO$_3$ ذو البنية البلورية " بيرو فسكيت" بعدة طرق: صول جال وصول جال احتراق باستعمال حمض الليمون، حمض الاسكوربيك والسكروز كممخلبات والماء، الميثانول والايثانول كمحلات، واستبدال كميات صغيرة بالحديد. استعملت عدة تقنيات لدراسة الخواص الكيميائية والفيزيائية لهذه المركبات وهي: XRD، TGA-TDA، S$_{BET}$، PSD، FTIR،XPS لدراسة الخواص الحفزية للمركبات المعالجة حراريا في 750 و800 درجة مئوية. قمنا باختبار العينات بواسطة الاكسدة الحفزية لأحادي أكسيد الكربون CO اذ وجدنا ان أحسن النتائج وافقت النسبة الأقل من الحديد المستبدل في بنية LaNiO$_3$.

</div>